UCLouvain

École polytechnique de Louvain

Fabrication of nanotextured electrodes for electrochemical sensors towards medical applications

Author: **Véra Manuelle Fokou Kingué**
Supervisor: **Jean-Pierre Raskin**
Readers: **Jean-Pierre Raskin, Laurent Francis, Ramy Moumneh, Clémentine Gevers**
Academic year 2023–2024
Master [120] in Electro-mechanical Engineering

Acknowledgment

First, I would like to express my deepest appreciation to Ramy Moumneh. Thank you for the support, for taking the time to answer all of my questions, for your patience, and for the constructive comments regarding my thesis.

I would also like to thank Professor Jean-Pierre Raskin, my supervisor, for his helpful recommendations and encouragement regarding my work.

Many thanks to Clémentine Gevers and Loïc Lahaye for their guidance throughout the entire year and helpful advice.

I would like to extend my sincere thanks to Sami Yunus and Grégoire Le Brun for providing the necessary equipment for my experiments. Thank you for your enthusiasm for my work.

I am also grateful to Professor Laurent Francis for accepting to be part of my Jury.

A special thanks to my family for their support and encouragement during the writing of this work.

Abstract

Venous thromboembolism (VTE) is a medical condition that arises when a blood clot develops in a vein. It is a common cardiovascular disease ($\sim$ 700 per 100 000, death rates up to 40%) difficult to diagnose due to its non-specific symptoms [68]. A strategy to detect the risks of VTE is the measure of the D-dimer level in a blood sample. Currently, there is a lack of reliable and affordable point-of-care assays to diagnose the risks of VTE.

This master's thesis is part of a research project aimed at developing a reliable and affordable D-dimer point-of-care electrochemical biosensor. The sensor's sensitivity is a crucial aspect of the design, and it depends on the charge-transfer resistance of the biosensor electrode. This work contributes to this research project by investigating the impact of the deposition of gold nanoparticles on the charge-transfer resistance. In the scope of this thesis, the electrophoretic deposition and the drop casting of gold nanoparticles were used to modify graphite ink electrode surfaces. Additionally, a characterization method using scanning electron microscope images (SEM) was developed. Lastly, electrochemical impedance spectroscopy measurements (EIS) were used to evaluate the impact of the deposition process on the charge-transfer resistance.

It was demonstrated that the electrophoretic deposition of AuNPs works at high voltages (27V). However, the process damaged the graphite ink electrode. At lower voltages, the electrophoretic deposition process did not have a significant influence on the amount of deposited AuNPs. The drop casting method, however, could be performed on graphite ink electrodes but the method presents limits in terms of reproducibility. A decrease of the charge-transfer resistance of up to 80% was observed for electrodes modified with AuNPs. Finally, the EIS measurements presented several issues. Multiple solutions to those issues were suggested and would need to be tested in future work.

Contents

Chapter 1

Introduction

Venous thromboembolism (VTE) is a condition that occurs when a blood clot forms in a vein, as shown in figure 1.1 [64]. It is a common cardiovascular disease ($\sim$ 700 per 100 000, death rates up to 40%), and the symptoms are non-specific, making the diagnosis of this disease difficult. [68].

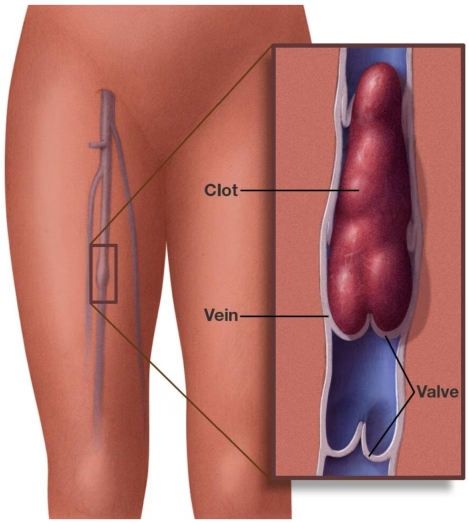

Figure 1.1: Blood clot due to venous thromboembolism [14]

A common strategy to detect the risks of VTE is the measure of the D-dimer level in a blood sample. After this measure, hospital confirmatory image testing is done if the patient presents risks of VTE. Nowadays, there is a lack of reliable and affordable point-of-care (POCT) testing assays for rapid quantification of the D-dimer level. There is a need for the development of biosensors for D-dimer testing. This would allow to perform testing at the patient's location and avoid unnecessary referrals to hospitals for imaging tests. [48, 61].

The research project linked to this master's thesis aims to develop a low-cost, rapid, and handy POCT electrochemical biosensor for testing D-dimer level in blood samples. One objective pursued by this project is the development of surface-modified electrodes to improve the sensitivity of the electrochemical devices.

This work is divided into six chapters. The second chapter presents a literature review that is divided into three sections:

- A state of the art of the research field related to biosensors
- An explanation of the electrochemical impedance spectroscopy method (EIS). It will serve as a basis for understanding the measurements in later chapters.
- A state of the art of the recent surface modification method for electrodes as well as their advantages and drawbacks.

The third chapter presents the design of the electrochemical device and the theory behind the sensor's sensitivity. The reasons for the use of gold nanoparticles are also described. In the third chapter, the main objective of this thesis is explained, as well as the research questions.

The fifth chapter details a characterization method involving the use of scanning electron microscope images (SEM) to estimate the amount of deposited AuNPs on electrodes. The sixth and seventh chapters present the deposition process of AuNPs via electrophoretic deposition and drop casting. The previously developed characterization method using SEM images is used to compare the deposition processes. Lastly, the eighth chapter examines EIS measurements of electrodes modified with AuNPs. In the ninth chapter, a conclusion and guidelines for future works are given.

Chapter 2

Literature Review

2.1 Biosensors

Nowadays, biosensors are used in a wide range of different fields, such as healthcare, the food industry, and environmental monitoring [39]. Biosensors are analytical devices that can convert a biological response into an electrical signal [21]. They combine two elements: a bio-element that can recognize a target analyte and a sensor element that detects biorecognition processes and transforms this information into an electrical signal [41, 44]. Standard biosensors comprise an analyte, a bioreceptor, a transducer, electronics, and a display. A schematic of a general biosensor is presented in figure 2.1.

- Analyte: It is the substance to be detected by the biosensor.
- Bioreceptor: It is the bio-element in charge of detecting the target analyte. There are various bioreceptors depending on the analyte. It could be an enzyme, an antibody, etc...
- Transducer: This part converts the biological information into an electrical signal. This signal can take the form of current, voltage, or impedance.
- Electronics: The electronics amplify the signal and process it for further analysis through a display.

For the construction of the biosensor, adherence of the bioreceptor onto the transducer is important. This step of the construction process is called *functionalization*. Four techniques for bioreceptor immobilization on electrodes are cited in the literature: adsorption, covalent bonding, crosslinking, and encapsulation[7].

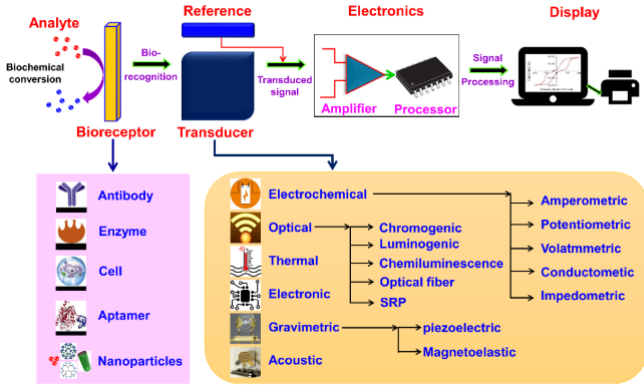

Figure 2.1: Schematic representation of a typical biosensor [44]

2.1.1 Characteristics of biosensors

The efficiency of biosensors can be measured through various criteria: selectivity, sensitivity, reproducibility, and stability [9]. They give requirements that must be validated to ensure the creation of a highly effective biosensor [44].

- Selectivity: Selectivity is an important characteristic for the choice of a bioreceptor. A selective biosensor can detect a target analyte even in the presence of unwanted contaminants in samples. Making a selective biosensor is a challenge in clinical applications because the analyzed samples are complex and contain various analytes different from the target analyte [9].

- Sensitivity: The sensitivity measures the ratio between the transduced signal intensity and the variation of the concentration of the target analyte. Upper and lower detection limits define the range of measurable signals. The desired lower limits of detection range from nano molar (ng/mL) to pico (fg/mL) molar for typical biosensors [9, 44].

- Reproducibility: Reproducibility can be defined by accuracy and precision. Accuracy corresponds to the ability of the sensor to give measurement that corresponds to the true concentration of the target analyte in the sample. Precision is the ability of the sensor to provide the same measurements multiple times when the same sample is being analyzed.

- Stability: The stability of the biosensor is primordial when continuous monitoring is required. This criterion depends on the affinity of the bioreceptor and the degradation over time of the biosensor [44, 9].

2.1.2 Classification of Biosensors

Biosensors can be classified according to various criteria. This literature review presents only classifications based on the bioreceptor and the transducer in figure 2.2. A more complete classification of biosensors is given in [44].

Based on the biorecognition principle, biosensors are classified as catalytic biosensors or non-catalytic biosensors. Analyte–bioreceptor interactions in a catalytic biosensor lead to the synthesis of novel biochemical reaction products [45]. The bioreceptors for this type of biosensor are enzymes, microorganisms, tissues, and whole cells. In non-catalytic (or affinity) biosensors, the interactions between the analyte and the bioreceptor result in the irreversible bonding of the analyte to the receptor, and no new biochemical reaction product is produced. The bioreceptors of this type of biosensor comprise antibodies, cell receptors, and nucleic acids [44]. Biosensors can be classified according to their transducer. Biosensors are categorized as electrochemical, optical, thermal, and piezoelectric biosensors [7].

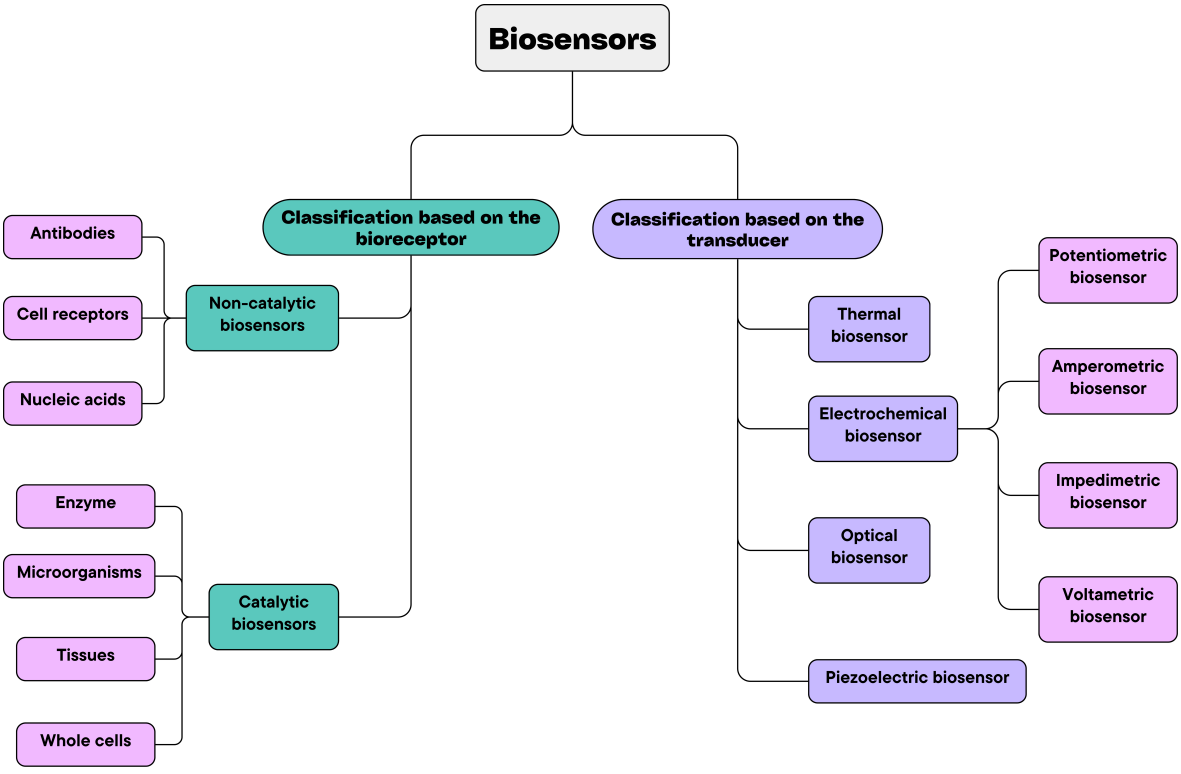

Figure 2.2: Classification of the biosensors according to the bioreceptors and the transduction method

2.1.3 Immunosensors

Immunosensors are affinity biosensors in which the target analytes are antigen and the bioreceptors are antibodies [42]. Antibodies are also called immunoglobins and can be recognized through their characteristic "Y" shape shown in figure 2.3 [9]. Antibodies are formed from light and heavy polypeptidic chains. Antibodies bind with their antigen to form a stable immunocomplex that is detected by the sensor[24, 39, 42]. Based on the detection method, immunosensors can be further divided into two categories: labeled and label-free immunosensors [44].

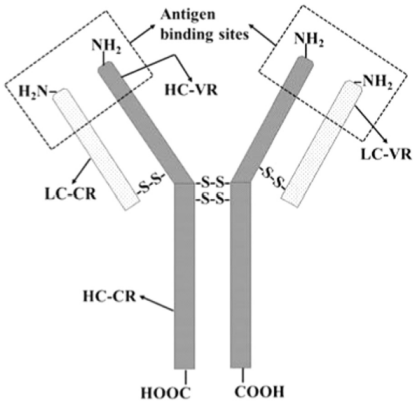

Figure 2.3: Schematic representation of heavy and light chains combined to form the most common antibody (IgG). LC = Light chains, HC = Heavy chains, CR = Constant region, VR = Variable region, SS = disulfide bridges [19]

Labeled immunosensors A label is a foreign molecule that is chemically or temporarily attached to the target analyte [60]. The label generates a signal that is detected by the immunosensor. The number of labels detected corresponds to the number of target analytes [42]. The label can, for instance, be fluorescent or chemiluminescent molecules or nanomaterials like gold nanoparticles [9].

Label-free immunosensors Label-free (or direct) immunosensors monitor physical or chemical changes due to the formation of antigen-antibody complexes. Target analyte can be detected without prior chemical modification due to labeling [55, 19]. However, one major difficulty for the construction of label-free immunosensors is the specificity. Real clinical samples are complex and contain various antigens and other proteins that can bind with the antibodies or the surface of the immunosensor. This leads to an increase of the background signal and a decrease of the immunosensor's

sensitivity [55, 42]. A schematic representation of label and label-free detection is represented in figure 2.4:

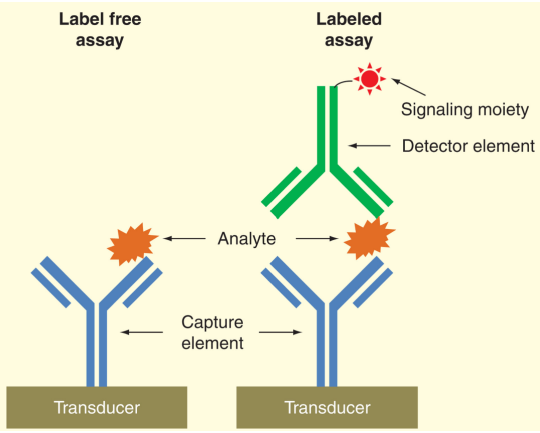

Figure 2.4: Label and label-free detection [55]

Like biosensors, immunosensors can be divided into multiple categories depending on the transduction process: optical immunosensor, piezoelectric immunosensor, and electrochemical immunosensors [36]. In this literature review, only electrochemical biosensors/immunosensors are presented. More information on the other types of transduction methods for biosensors can be found in [37, 12, 44].

2.1.4 Electrochemical biosensors

Electrochemical biosensors rely on the fact that due to the interactions between the target analyte and the bioreceptor, many chemical reactions occur, leading to the production or consumption of ions. This leads to a change in the electrical properties at the surface of the transducer that can be sensed and measured by electrochemical biosensors [41, 7]. Electrochemical electrodes act as transducers for electrochemical sensors. Most electrochemical sensors use a two or three-electrode electrochemical cell. Three-electrode chemical cells are composed of a counter electrode (CE), a working electrode (WE), a reference electrode, and an electrolyte solution. Section 2.2.3 gives a more detailed explanation of electrochemical cells. Electrochemical reactions occur between the working electrode and the electrolyte, producing detectable electrochemical signals in the form of current, voltage, impedance, and capacitance. This signal is proportional to the concentration of target analytes on the surface of the WE. Recently, great interest has been shown in electrochemical biosensors due to their affordable cost and the fact that they require low power to work properly. This makes those sensors suitable candidates for portable devices and Point of Care testing [65, 27]. Depending on the nature of the electrical

signal measured, electrochemical biosensors can be categorized as potentiometric, amperometric biosensor, voltammetric, or impedimetric [18].

Potentiometric biosensors

Potentiometric sensors measure the accumulated charges or potential at the working electrode due to the interaction between the analyte and the bioreceptor. The potential is measured relative to the reference electrode [44]. Ion activity can be characterized with the Ernst equation. This equation describes the relationship between free ion concentration and the potential applied [37, 31]:

$$E_{cell} = E^0_{cell} - \frac{RT}{nF} lnQ$$

where E_{cell} is the cell potential, E^0_{cell} is the standard cell potential, R is the universal gas constant, T is the temperature, n is the charge number of electrode reaction, F is the Faraday constant and Q is the ratio of ion concentrations between the anode and the cathode.

Amperometric / voltametric biosensors

In amperometry, a constant potential is applied to the working electrode with respect to the reference electrode. This causes electrochemical oxidation or reduction of electroactive species in the electrolyte, and a current proportional to the concentration of the analyte present in the solution can be measured at the working electrode [29]. In voltammetry, a potential is also applied at the working electrode but varies over time. The measure of the current is proportional to the concentration of the analyte in the solution [44].

Impedimetric immunosensors

Impedimetric biosensors use a method called Electrochemical Impedance Spectroscopy (EIS). This method applies a small sinusoidal excitation signal at the working electrode to measure the impedance at the interface between the electrode/electrolyte. The sensor measures the change in impedance that can be correlated to the concentration of the target analyte immobilized on the electrode [49, 3]. A deeper explanation of this electrochemical method is given in the section 2.2. Impedimetric biosensors use label-free detection. To ensure good selectivity, the bioreceptor must have the ability to specifically bind with the analyte. Therefore, bioreceptors like DNA, antibodies, etc. are used [31].

2.2 Electrochemical impedance spectroscopy

Electrochemical impedance spectroscopy (EIS) is done by applying a small AC voltage signal to a system and measuring the electrical current response [69]. This method uses a small excitation signal (typically 5-10 mV) in order to ensure that the signal response is linear[19]. EIS gives insight into the electrochemical changes at the surface of the electrode due to the analyte binding with the bioreceptor [3]. The AC signal is often superposed with a DC signal, but in the following subsections, for simplicity, the DC component isn't represented.

2.2.1 Impedance definition

The excitation voltage applied can be presented as a function of time and has the form:

$$E_t = E_0 sin(\omega t)$$

Where E_t corresponds to the potential applied at time t, E_0 is the amplitude of the signal, and ω is the frequency of the signal in rad/sec. In a linear system, the current response to this small sinusoidal excitation is a sinusoidal with a phase shift.

$$I_t = I_0 sin(\omega t + \phi)$$

Where I_t is the current response at time t and ϕ is the phase shift of the current with respect to the applied voltage. E_t and I_t are both represented in figure 2.5.

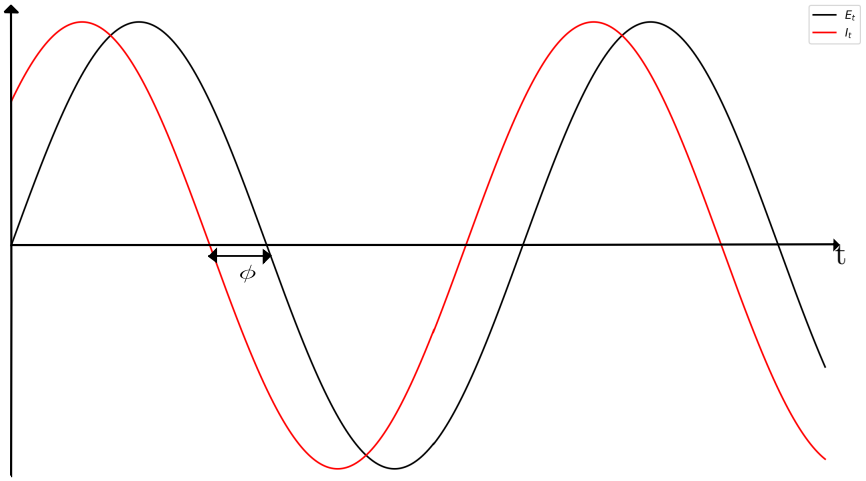

Figure 2.5: Applied voltage E_t (in black) and the current response I_t (in red)

The impedance of a complex system Z is given by the following equation:

$$Z = \frac{E_t}{I_t} = Z_0 exp(j\phi) = Z_0(cos\phi + jsin\phi) = Z_R + jZ_{Im}$$

The impedance is a complex value and can be represented via: Nyquist plot and bode plot as shonw in figure 2.6. Z_0 and ϕ are often represented in bode plots while the real Z_R and imaginary Z_{Im} parts of Z are used for Nyquist plot.

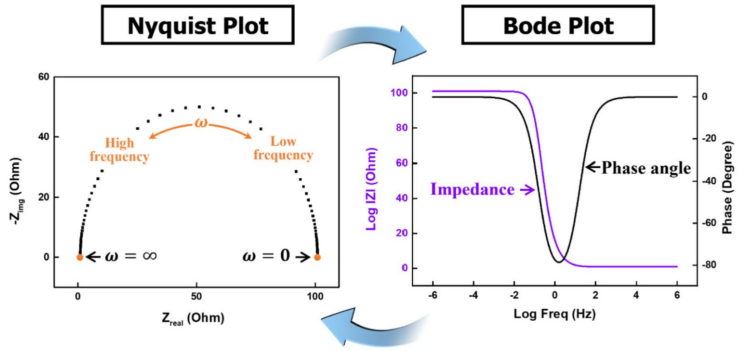

Figure 2.6: Nyquist diagram and its corresponding bode plot [13]

2.2.2 Impedance representation

EIS data are usually analyzed by fitting an equivalent electrical circuit to the data using basic elements like resistors, capacitors, and inductors [30]. The currents and voltages in those basic elements are represented in figure 2.7. Their corresponding Nyquist diagram and bode plots are shown in figure 2.8.

- In a resistor, the current and voltage are in phase, and the impedance is independent of the frequency. $Z_R = R$

$$i(t) = v(t)/R$$

- In a capacitor, when an AC voltage is applied, the current at time t is given by:

$$i(t) = C\frac{dv}{dt}$$

  This equation yields that in a capacitor the current is shifted from the voltage by a -90° phase shift and $Z_C = \frac{1}{j\omega C}$.

- In an inductor, there is a +90° phase shift between the voltage and the current, $Z_L = j\omega L$.

$$i(t) = L\int i(t)$$

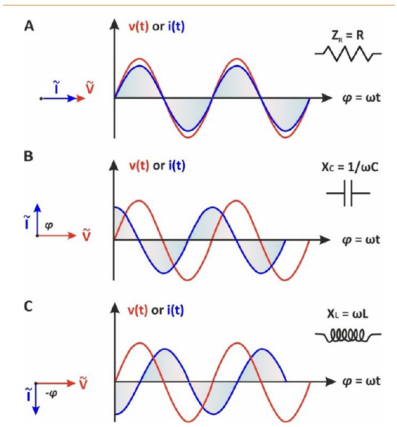

Figure 2.7: Current and voltage in basic circuit elements [30]

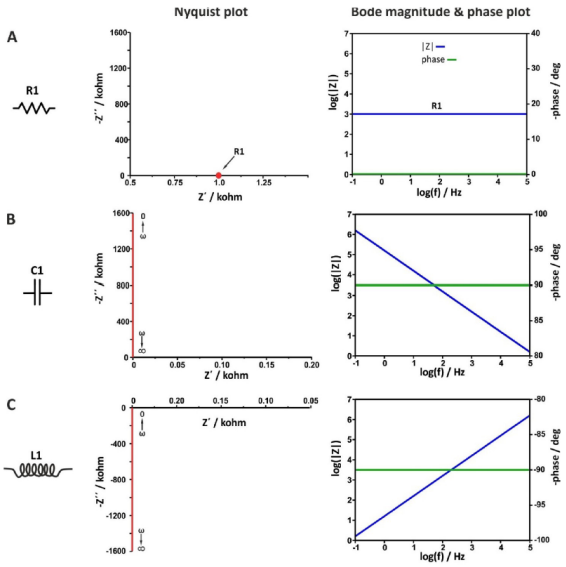

Figure 2.8: Nyquist diagrams and bode plots of resistors, capacitors, and inductors [30]

2.2.3 Three-electrode electrochemical cells

The most common setup used for EIS measurements is a three-electrode electrochemical cell. A schematic representation of a three-electrode electrochemical cell is given in figure 2.9. In this configuration, the cell consists of a working electrode (WE), a counter electrode (CE), a reference electrode (RE), and an electrolyte. An electrolyte is a solution made of water or other solvents in which ions are dissolved [17]. The cell is connected to a potentiostat. This device applies a potential at

the WE with respect to the RE and measures the current that flows between the WE and the CE. At the surface of the working electrode, electrochemical (redox) reactions take place due to the applied voltage [38]. Reference electrodes serve as a reference point for the applied voltage to the working electrode. Therefore, they must hold constant potential on an absolute scale during the measurement. This is achieved by having little to no current flowing through them. Reference electrodes have standard potential. This potential was measured against a standard hydrogen electrode whose potential is defined as 0V. References made of silver/silver chloride (Ag/AgCl) are commonly used and have a standard potential $E^\circ = 0.223$ under standard conditions [63, 56, 15]. To ensure all the current goes to the counter electrode and any change in terms of signal is only due to the working electrode, its surface is usually larger than the surface of the working electrode [63]. Then, because redox reactions also occur at the CE, they are usually made of inert-redox materials such as platinum or carbon [17].

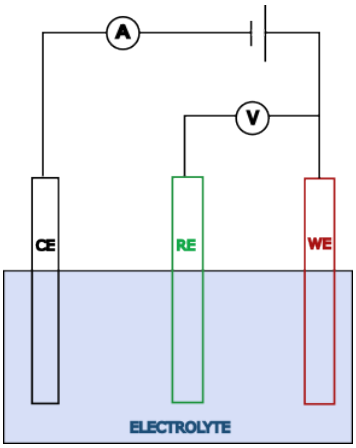

Figure 2.9: Schematic representation of a three-electrode electrochemical cell

2.2.4 EIS analysis of electrochemical cells

When the EIS measurements are done in the presence of a redox couple in the electrolyte, the impedance to the current flow between the CE and RE in an electrochemical cell can be represented via an equivalent Randles circuit shown in figure 2.10. This type of EIS measurement is called Faradaic EIS. The equivalent Nyquist diagram is given in figure 2.11. In this case, a DC potential matching the standard potential E° of the redox couple is superposed to the small AC excitation signal [30].

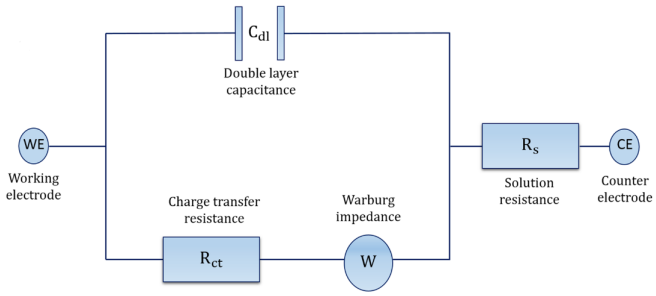

Figure 2.10: Randles equivalent circuit[31]

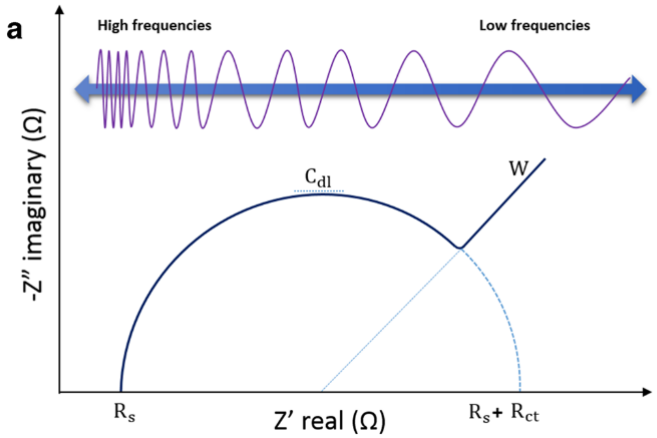

Figure 2.11: Nyquist diagram of a Randles circuit [31]

A typical Randles circuit is made of: R_s, R_{ct}, C_{dl} and W. R_s corresponds to the ohmic resistance of the electrolyte between the working and the reference electrode. For a given electrolyte, R_s depends on the concentration of free ions in the solution and the geometry of the area in which current is carried.C_{dl} is the double layer capacitance, it is represented in figure 2.12. When a potential is applied to an electrode, ions are adsorbed in the electrode's surface separating it from the charged ions in the electrolyte 2.12. This forms an electrical double layer that can be modelized by a capacitor. Most of the time, the perfect capacitor does not exist, and an element called a constant phase element (CPE) is used to model the non-ideal behavior of the double layer capacitance. It is defined as $Z_{CPE} = \frac{1}{Y_0(j\omega)^N}$ where Y_0 is the capacitance in $Ohm \cdot s^N$ and N is an exponent that is equal to 1 when CPE is an ideal capacitor and to 0 for a resistor [4, 30]. N accounts for the non-ideal behavior of the double-layer capacitance. The origin of this non-ideal behavior has been attributed to surface roughness, fractal dimensions

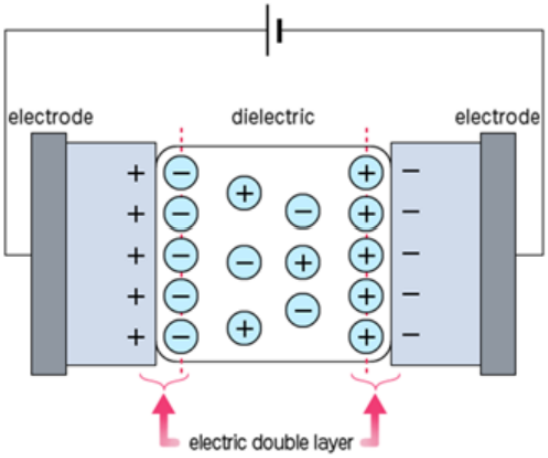

Figure 2.12: Double-layer capacitance

of the surface, non-uniform current distribution, etc. For rough electrodes, it has often been observed that N ranges between approximately 0.7 and 0.9 [4, 30, 1, 47]. More detailed information regarding the different theories explaining the causes of CPE can be found in [1, 47, 28, 50]. A representation of CPE with resistors in a Nyquist diagram is given in figure 2.13. $\theta = 90°(1 - N)$

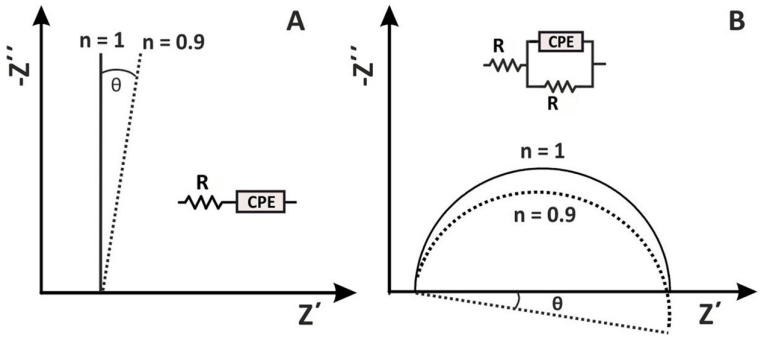

Figure 2.13: (left) Nyquist diagram of CPE in series with a resistor; (right) Nyquist diagram of a resistor in series with CPE in parallel to R [30]

Due to the redox reaction, a faradaic current flows through the electrochemical cell. This is represented via R_{ct} in series with Z_W. The charging and discharging of C_{dl} occur simultaneously to the faradaic process. Those two processes are represented in the Randles circuit with C_{dl} in parallel with $R_{ct} + Z_W$. R_{ct} is the charge-transfer resistance, and it is related to the kinetics of the heterogeneous

electrochemical process as per the equation:

$$R_{ct} = \frac{RT}{k^0 n^2 F^2 AC} \tag{2.1}$$

where k^0 is the heterogeneous electron transfer rate in cm/s, n is the number of electrons transferred in the electrochemical reaction, F is Faraday's constant (96485 C/mol), R is the gas constant (8.314J/molK), T is the temperature in kelvin, A is the electroactive surface area of the working electrode in cm^2 and C is the concentration of the redox species assuming that this concentration is the same as the one in the bulk solution and that $C_{ox} = C_{red} = C$ [30]. Z_W is the Warburg impedance. Diffusion of the reactants to the electrode surface creates an impedance Z_W called the Warburg impedance.

$$Z_W = \sigma\omega^{1/2}(1 - j)$$

where

$$\sigma = \frac{2RT}{n^2 F^2 \sqrt{2}\sqrt{D}C}$$

where D is the diffusion coefficient in $[cm^2/s]$. At high frequencies, Z_W is small since diffusing reactants don't have to move far. At lower frequencies, the redox molecules have to diffuse far hence an increase of Z_W can be observed. The Warburg electrode can also be expressed as $Z_W = \frac{1}{Y_0(j\omega)^{(1/2)}}$, it is represented by a straight line with a 45° angle from the reel axis in a Nyquist plot.

An intuitive comprehension of the nyquist diagram can be given using the frequency. At lower frequencies, $Z_{c_{dl}} >> R_{ct} + Z_W$ hence current will mainly pass through R_{ct}, Z_W and R_s. At high frequencies, the impedance of a capacitor is very low as it is proportional to the inverse of the frequency, $Z_{c_{dl}} << R_{ct} + Z_W$. The current will flow mainly through the capacitance layer C_{dl} and R_s.

2.2.5 EIS for impedimetric biosensor

The objective of impedimetric biosensor is to measure the change in transfer charge due to the binding of the analyte with the bioreceptor. In general, R_{ct} increases with the complexity of the electrode surface. This change can be translated into a detected concentration of analyte as shown in figure 2.14.

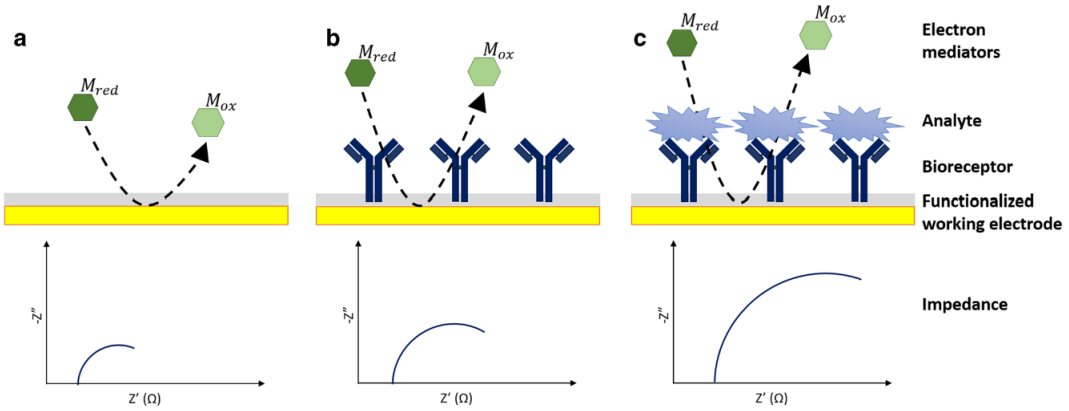

Figure 2.14: EIS spectra for impedimetric biosensor[31]

2.3 Electrode surface modification techniques

One major challenge associated with developing electrochemical biosensors is attaining high sensitivity [52]. Signal-based amplification methods modify the transducer (electrodes) to lower the LOD and increase sensitivity. This part of the literature review gives an overview of the recent techniques used to modify electrode surfaces. The underlying objective behind those techniques is the increase of the sensor's sensitivity [72].

2.3.1 Microtextured gold electrode

The formation of microporous/macroporous films provides a large active surface that leads to the decrease of the charge transfer resistance R_{ct}. The reduction of the charge transfer resistance is a key factor for increasing the sensitivity of electrochemical biosensors [10]. Methods for the formation of these films are presented in the following sections.

3D ordered microtexture via silica spheres

Silica (SiO_2) spheres have the advantage of producing highly ordered and repetitive 3D films. In [10], a vertical technique was used to assemble the spheres on a substrate and form a crystal. Then, a sintering step was performed, and gold was electrodeposited in the interstices of the silica sphere crystal. Finally, the mask of silica spheres was removed in order to obtain a microtextured electrode. The process is shown in figure 2.15. In [22], the use of Silica spheres to create highly ordered microelectrode array is reported. The formation of 3D ordered

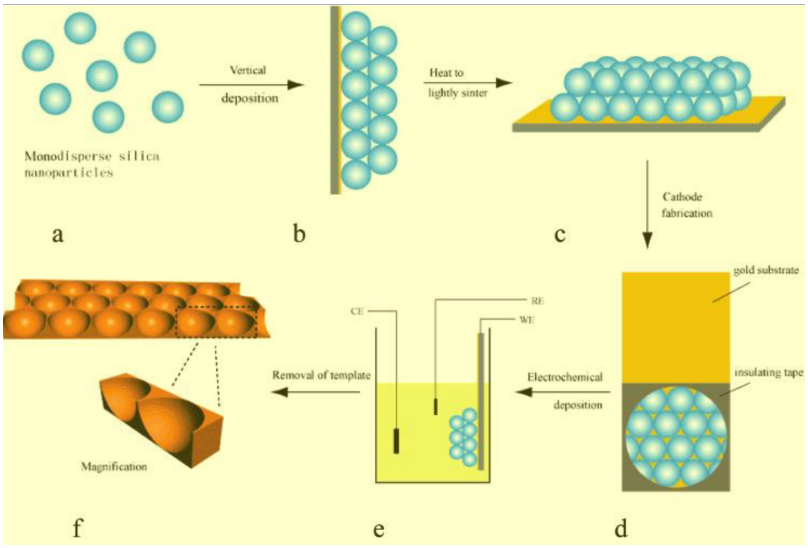

Figure 2.15: Preparation of 3D ordered macroporous gold film modified electrode [10]

macroporous film on electrodes provides a large active surface area, which can increase the density of immobilized bioreceptors and facilitate electron transfer [10].

Dynamic hydrogen bubble template

The preparation of macroporous/microporous films can be realized using the hydrogen bubble dynamic template method. When a high current is applied to the substrate electrode in order to electrodeposite a metal on the electrode, the reduction of H+ produces hydrogen bubbles that act as a template for the electrodeposited material [25]. A schematic representation of the dynamic hydrogen bubble template method is given in figure 2.16. In [71] and [32], microporous and macroporous gold electrodes were developed for the determination of mercury and for detection of glucose, respectively, using the hydrogen bubble dynamic template method. The formation of a three-dimensional porous material film would allow faster mass transport and increased active surface area of the electrode

2.3.2 Nanotextured gold electrode via gold nanoparticules

Gold nanoparticles have recently attracted a lot of attention as a good material for electrode surface modification. They have good biocompatibility, allowing the immobilization of bioreceptors on the electrode when the electrode material isn't biocompatible (for instance, carbon electrode) [54, 34]. Other advantages of

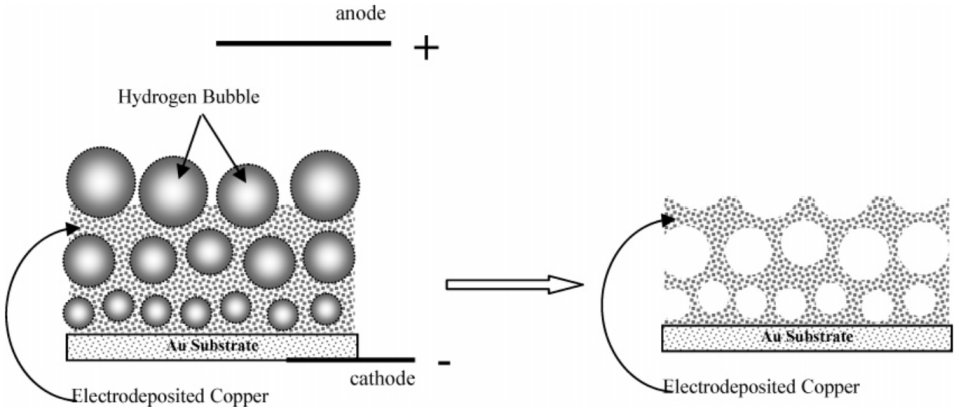

Figure 2.16: Schematic representation of the dynamic hydrogen bubble template method [33]

nanoparticles are their high conductivity, large surface-to-volume ratio enabling an increase of the active surface of the electrode, and the ability to increase electron transfer between redox species [58]. Gold nanoparticles are synthesized in an aqueous solution by reduction of chloroauric acid ($HAuCL_4$). $HAuCl_4$ is dissolved in boiling deionized water (100°C) using a reducing agent such as trisodium citrate ($Na_3C_6H_50_7$). This results in Au^{3+} ions to be reduced to neutral gold atoms. Gold atoms accumulate to form stable gold nanoparticles. Stable gold colloidal nanoparticle solutions can be prepared with this approach[70, 54]. There are several methods that have been developed in order to ensure binding of the AuNPs to surfaces. In the following sections, five methods for electrode surface modification using AuNPs are presented: Langmuir-Blodgett method, self-assembled monolayer (SAM), electrodeposition, electrophoretic deposition, and drop casting.

Langmuir-blodgett (LB) method

In this strategy, colloidal gold nanoparticles are spread onto the water surface in a tank, and the substrate is slowly lowered into the water. The process is shown in figure 2.17. While the substrate is lowered in the tank, the transfer of the AuNPs onto the substrate is controlled by surface pressure of the monolayer of nanoparticles at the water surface and the speed at which the electrode is lowered in the tank. This strategy is used to form a monolayer of gold nanoparticles over a substrate. Repeating the process allows for the formation of multiple layers. One advantage of the LB method is that it gives precise control over the film structure. However, one major drawback of this method is that a step to modify the surface of AuNPs and make them hydrophobic is necessary [54, 59].

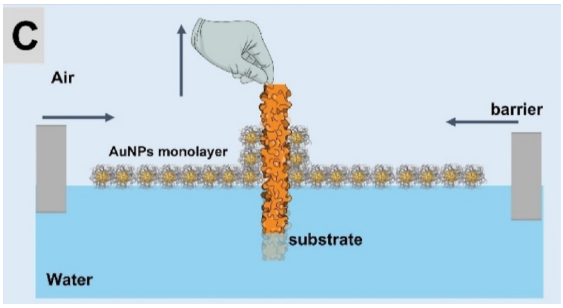

Figure 2.17: Schematic representation of the Langmuir-Blodgett method [54]

Self-assembled monolayer (SAM)

Functional groups of thiol can be immobilized on an electrode surface in order to act as a template for the attachment of AuNPs. Control over the spacing and the distribution of the thiol molecules allows control over the film of AuNPs [54]. In figure 2.18, a film of AuNPs using self-assembled monolayers is represented. SAMs are created via the adsorption of thiol molecules to the electrode surface. An advantage of the SAM method is the good stability of the layer and the ability to create highly order gold nanoparticule films. [62].

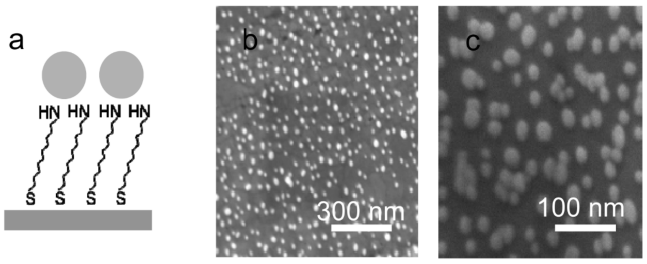

Figure 2.18: (a) Schematic representation of SAM with attached gold nanoparticules, (b) and (d) SEM images of the electrode modified with SAM and AuNPs [53]

Electrodeposition

In this method, a substrate is put into a solution containing $HAuCl_4$, and a potential is applied between the WE and the RE. The applied potential causes the reduction of Au^{3+} ions present in the solution onto the substrate (WE) surface. A film of AuNPs is formed on the substrate surface. Size, density, and distribution of the AuNPs can be controlled via the applied potential, the concentration of $HAuCl_4$ in the solution, and the duration of the process [54]. In [11], a highly sensitive electrochemical biosensor was realized using an indium thin oxide (ITO)

electrode modified with electrodeposited AuNPs. Good coverage of the electrode with AuNPs was obtained. Results are shown in figure 2.19.

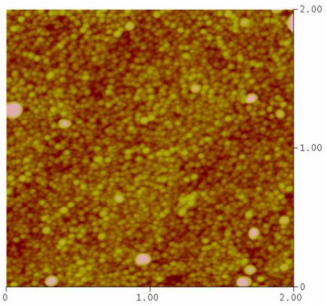

Figure 2.19: atomic force microscope image of the ITO electrode after the AuNPs electrodeposition process [11]

Electrophoretic deposition (EPD)

During the electrophoretic deposition process, the substrate is in a solution of charged particles. A potential opposite to the charge of the particles to be deposited is applied on the substrate with respect to an anode, creating a constant electric field between the substrate and the anode[5]. A force is applied to the charged particles due to the electrical field according to the equation:

$$F = qE$$

where F is the applied force, q is the charge of the particle and E is the electrical field [8].

The Hamaker equation is used to express the weight of the film of particles

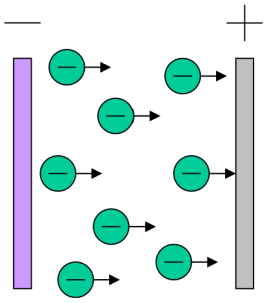

Figure 2.20: [5]

deposited onto a substrate:

$$w = \frac{2}{3} C \cdot \epsilon_0 \cdot \epsilon_r \cdot \zeta \cdot (\frac{1}{\eta})(\frac{V}{d}) \cdot t \tag{2.2}$$

Where w is the weight of deposited nanoparticles, C is the concentration of particles, ϵ_0 is the permittivity of vacuum, ϵ_r is the relative permittivity of the solvent, ζ is the potential of the nanoparticles, η is the viscosity of the solvent, V is the applied voltage, d is the distance between the electrodes, t is the time of the deposition process. Except for V, t, d, and C, all the other parameters are constant because they depend on the solution used for the deposition process [16]. Electrophoretic deposition offers the possibility to control the thickness and density of the deposited nanoparticle films by varying the potential and deposition times. Moreover, the electrophoretic deposition process can be done on various substrate shapes [5, 8]. In [73], AuNPs were deposited via EPD onto the ITO glass substrate. The AuNPs presented good mechanical adhesion strength to the substrate. This method presents the advantages of being a fast process that can result in the formation of an ordered film of AuNPs.

Drop casting

For this method, a drop of gold colloidal nanoparticles is deposited on the electrode, and the drop is allowed to dry [58]. The thickness of the deposited film can be controlled via the concentration of the colloidal solution of nanoparticles and the volume of solution deposited [54]. One drawback of drop casting is the coffee-ring effect as shown in figure 2.21. The origin of this effect is the nonuniform evaporation flux that takes place at the interface air-liquid of the droplet. More liquid evaporates at the edges of the drop compared to the center. This loss is compensated by a flow of the solution and the nanoparticles from the center to the edges leading to a ring-like shape of nanoparticles once the solution completely dries [40, 26].

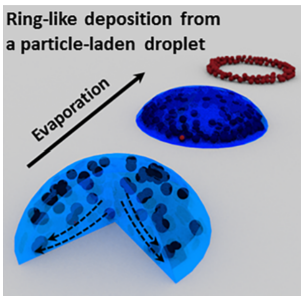

Figure 2.21: Coffee-ring effect

Chapter 3

Presentation of the detection device

This work is part of a research project aiming at developing an electrochemical biosensor to diagnose risks of venous thromboembolism by detecting the D-dimer level in blood samples. The sensor is depicted in figure 3.1. It features a paper chip for sample handling and an external device for electrochemical sensing. A crucial step in the sensor's design involves the development of an impedimetric immunosensor for the external electrochemical device.

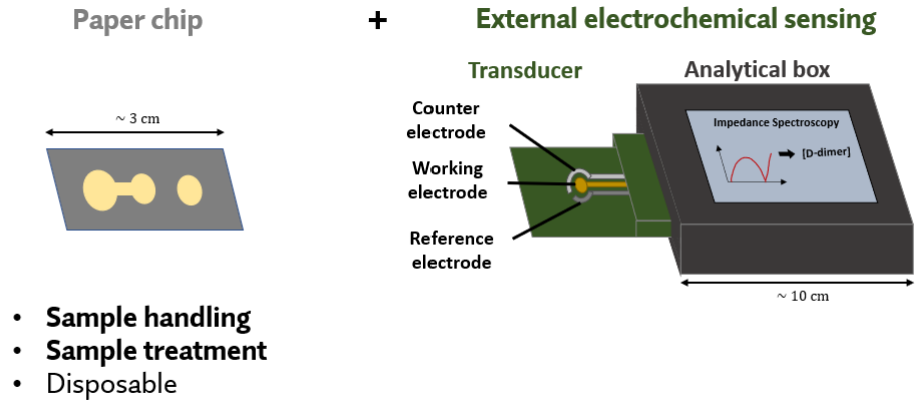

Figure 3.1: Design of the electrochemical biosensor of the research project. *The illustration was realized by Ramy Moumneh*

In the section 2.2 related to electrochemical impedance spectroscopy in the literature review, it was demonstrated that an electrochemical cell, when in the presence of a redox couple, can be modeled by a Randles equivalent circuit as illustrated in figures 3.2 and 3.3.

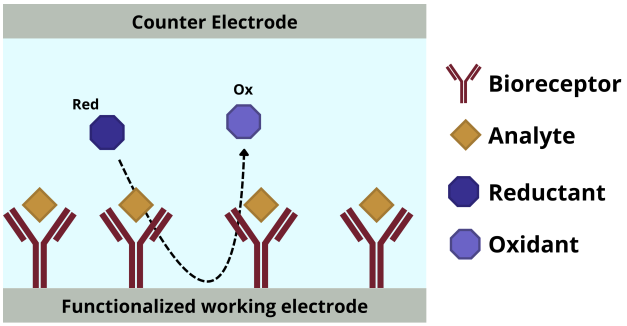

Figure 3.2: Electrochemical cell

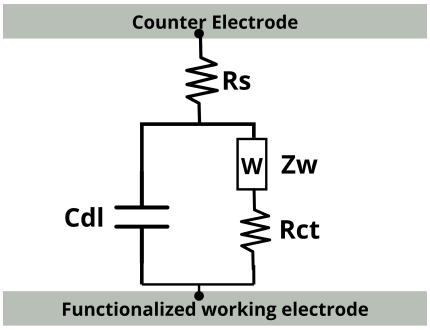

Figure 3.3: Randles equivalent circuit of an electrochemical cell in the presence of a redox couple

The sensitivity of the impedimetric immunosensor is defined in equation as:

$$S = \frac{R_{ct,final}}{R_{ct,initial}}$$

where $R_{ct,initial}$ represents the charge transfer resistance of the electrode with antibody attached to its surface, and $R_{ct,final}$ represents the charge transfer resistance of the electrode with the (bioreceptor) antibodies and the (analyte) D-dimer immobilized on its surface. They are represented in figure 3.4.

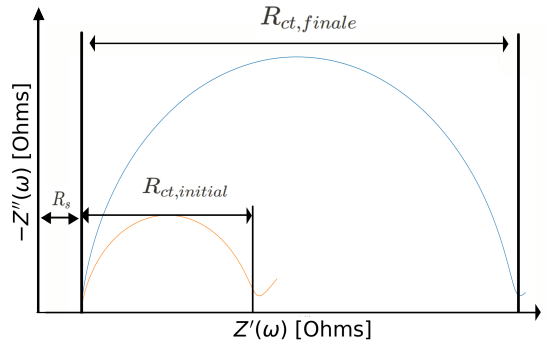

Figure 3.4: $R_{ct,initial}$ is the charge transfer resistance of electrode with the antibodies, $R_{ct,final}$ is the charge transfer resistance of the electrode with the antibodies and the D-dimer

R_{ct} is given by the formula:

$$R_{ct} = \frac{RT}{k^0 n^2 F^2 A_{active} C} \tag{3.1}$$

where k^0 is the heterogeneous electron transfer rate in cm/s, n is the number of electrons transferred during the electrochemical reaction, F is the Faraday's constant (96485 C/mol), R is the gas constant (8.314J/mol.K), T is the temperature in kelvin, A_{active} is the electroactive surface area of the working electrode in cm^2, and C is the concentration of the redox species assuming that this concentration is the same as in the bulk solution and that $C_{ox} = C_{red} = C$ [30].

Several electrode surface modification methods have been cited in the previous literature review. A common objective shared by these methods is increasing the electrode's active surface A_{active}. This gives a double advantage in terms of sensitivity. First, since R_{ct} is proportional to the inverse of A_{active} as shown in equation 3.1, if A_{active} increases, $R_{ct,initial}$ of the surface-modified electrode should decrease. Second, since A_{active} increases, more antibodies can be immobilized on the surface-modified electrode, leading to more target analytes being immobilized on the electrode surface for the same volume. In summary, if A_{active} increases, $R_{ct,final}$ increases while $R_{ct,initial}$ decreases. Finally, it is expected that:

$$S_{\text{modified electrode}} > S_{\text{non-modified electrode}}$$

Surface modification methods involving the deposition of gold nanoparticles (AuNPs) on the electrode have been reviewed. Gold nanoparticles have unique properties such as their high conductivity, large surface-to-volume ratio, and ability to increase electron transfer between redox species [58]. For the sensor, graphite electrodes are used. They present several advantages: they are low cost, they can easily be made using graphite ink, and graphite electrodes have already been used in the healthcare sector for electrochemical detections. However, graphite electrodes are not biocompatible, meaning that they can not be functionalized; in other words, antibodies can not be immobilized on graphite electrodes. The deposition of AuNPs to modify the surface of graphite electrodes would offer three advantages: a decrease in the charge-transfer resistance, the biocompatibility of the electrode surface, and the modification of the electrode surface without the need for cleanroom facilities. For these reasons, in this thesis, the deposition of AuNPs on graphite electrodes was realized.

Chapter 4

Master's Thesis Objective

The main objective of this master's thesis is ***the modification of electrodes with deposited gold nanoparticles to increase the sensitivity of an impedimetric immunosensor***.

This objective was divided into three research questions:

- ***Is it possible to deposit gold nanoparticles on a graphite electrode via electrophoretic deposition or via drop casting?***
- ***How can we evaluate the amount of deposited gold nanoparticles on the electrode surface via a characterization method?***
- ***Is there an effect on the charge-transfer resistance when the electrode is modified with gold nanoparticles***

To answer these research questions, the development of a characterization method using SEM images to estimate the amount of deposited AuNPs on a graphite electrode is explained *Chapter 4*. *Chapters 5* and *6* present the electrophoretic deposition and drop casting of AuNPs on graphite electrodes, respectively. Finally, electrochemical impedance spectroscopy measurements were performed to evaluate the effect of the deposition of AuNPs on graphite electrodes in *Chapter 7*.

This thesis focuses on the reduction of the charge-transfer resistance (R_{ct}) through the deposition of AuNPs on graphite electrodes. modification techniques. The exact origins behind the decrease of R_{ct} via AuNPs and the influence of electrode functionalization on R_{ct} are beyond the scope of this study.

Chapter 5

Electrode Characterization method via SEM images

5.1 Introduction

Before delving into the explanation of the electrode fabrication processes, the electrode surface is analyzed, and a characterization method using SEM images is presented. This method was developed to estimate the amount of deposited AuNPs after the electrode surface modification in later chapters.

5.2 Analysis of the electrode surface

A scanning electron microscope (SEM) and an atomic force microscope (AFM), Multimode-Bruker in tapping mode, were used to get an overview of the graphite electrode surface structure.

SEM

It can be observed in figure 5.1 that the electrodes have an irregular shape, are not planar, and can sometimes have small holes.

AFM

The AFM measurement in figures 5.2 and 5.3 show an existing microstructure of the graphite electrode, and when looking at the roughness, it can be observed that there is also a nanostructure. This first analysis suggests that the initial microstructure of graphite electrodes might already enhance the performance of the biosensor since R_{ct} is inversely proportional to the electrode's active surface.

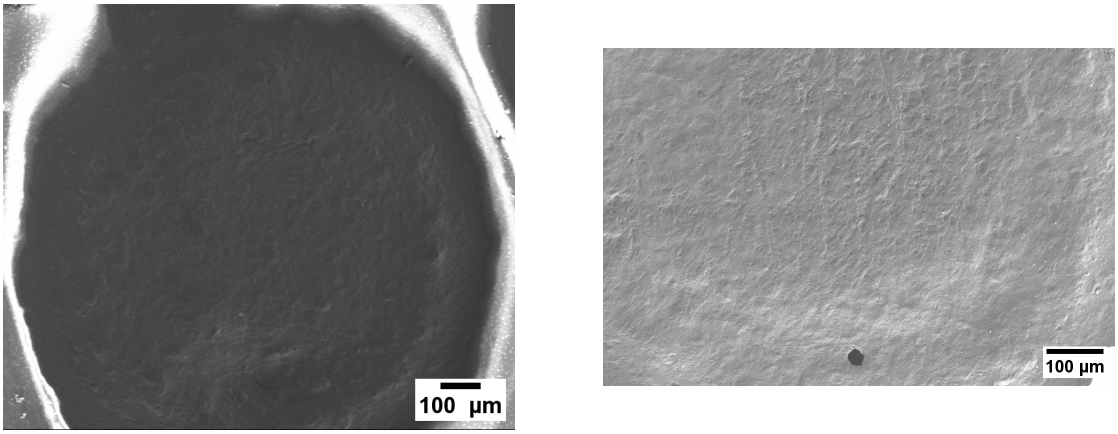

Figure 5.1: (left) SEM image of a graphite electrode; 68x magnification; (right) SEM image of a graphite electrode; 127x magnification

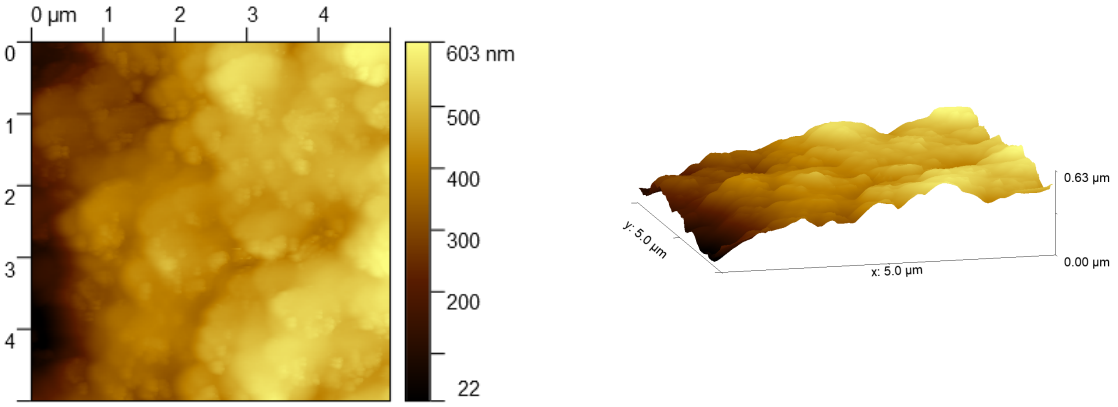

Figure 5.2: (left) 2D image taken with AFM, scan length is 5µm; (right) 3D image of the AFM measure, the average roughness of an horizontal profile is $R_a = 2.747nm$

5.3 Characterization method via SEM images

To count the nanoparticles in each image, an Image-based Tool for Counting Nuclei (ITCN) was used. ITCN was developed by Thomas Kuo and Jiyun Byun, who were members of the Center for Bio-image Informatics of the University of California, Santa Barbara [2]. ITCN is a plugin for the ImageJ software. Before the counting process, the SEM images were inverted using ImageJ. Inversion of the image creates a reversed image, similar to a photographic negative, of the entire image. To use the tool, the user must specify the average size of the particles and the average distance between them. For SEM images with a 30kx magnification, the best parameters were found to be 8px for the average size of the nanoparticles and 4px

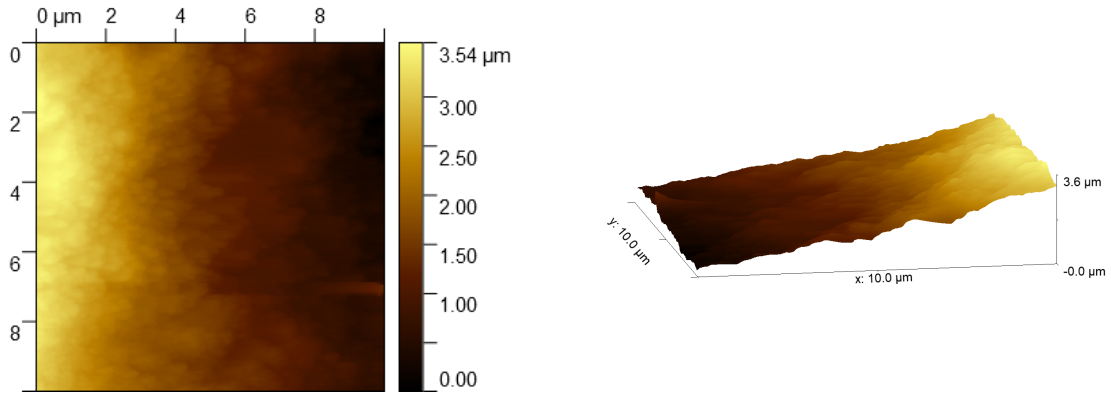

Figure 5.3: (left) 2D image taken with AFM, scan length is 10µm; (right) 3D image of the AFM measure, (c) Roughness of a horizontal profile of the SEM measure, the average roughness is 7.73nm

for the average distance. The performances of these parameters were assessed by counting the number of nanoparticles for the SEM image shown in figure 5.4.

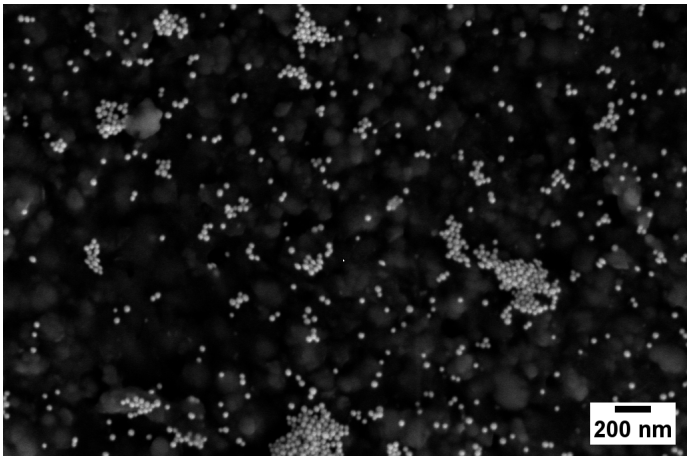

Figure 5.4: SEM image of a graphite electrode with deposited AuNPs; 30kx magnification, 818 particles were counted by the plugin and 811 were particles counted manually (by human)

Then, when the plugin counts the particles, it marks them with red dots, as shown in figure 5.5, so a visual check was also performed for several SEM images. The magnification was chosen to be 30kx because when smaller magnifications were used, the program could not differentiate the AuNPS from each other. The

graphite electrode has a diameter of 1mm, and if it were planar, its surface area would be 0.785mm2. Although with a 30k magnification, the size of the image is small, 1.089e-5mm2, compared to the surface of the electrode, 0.785mm2, it was not possible to images with smaller magnifications due to the constraint mentioned before.

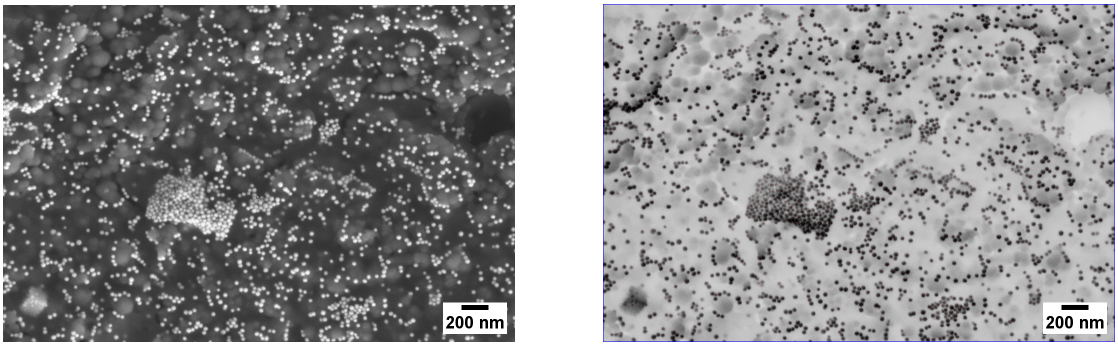

Figure 5.5: (left) SEM image of a graphite electrode with deposited AuNPs; 30kx magnification (right) SEM image of a graphite electrode with deposited AuNPs, the image was inverted, and the the red dots correspond to nanoparticles; 30kx magnification

The workflow to compute the number of AuNPs per electrode is shown in figure 5.6.

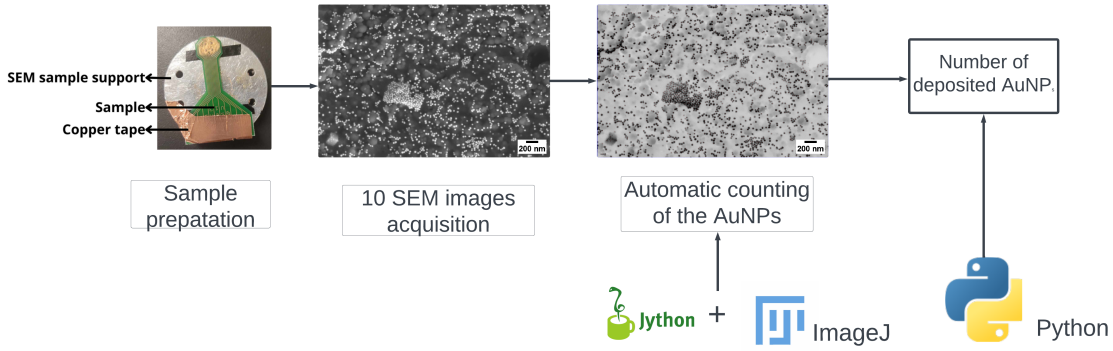

Figure 5.6: Workflow used to compute the amount of deposited AuNPs

- The sample needs to be grounded to take SEM images. Copper tape was used to connect the sample's contact to the SEM's support. Without this contact, the acquisition of SEM images is not possible because the SEM electron beam charges the sample, and those charges are not evacuated.

- 10 SEM images are taken per electrode to account for the non-uniform distribution of the deposited AuNPs.
- A Jython script was coupled with the ITCN plugin in order to automatize the counting over folders of images.
- Using Python, the average amount of nanoparticles for those 10 images was then used to estimate the number of nanoparticles deposited on the electrode. This estimation supposes that the graphite electrode is a planar disk of surface $S_{\text{planar electrode}} = \pi * (\frac{1}{2}) = 0.785mm2$.

  The SEM images for every sample are available in the appendices.

Finally, to assess the validity of the estimated number of deposited AuNPs, the maximum number of AuNPs that can be deposited on a planar electrode with the same diameter (1mm) as the graphite electrodes used in our setup was calculated. The 2D surface area of a nanoparticle with a diameter of 40nm is $\pi * (\frac{40.10^{-6}}{2}) = 1.256.10^{-9}mm^2$ and the surface of one electrode (if it was planar) $S_{\text{planar electrode}}$ is approximately $\pi * (\frac{1}{2}) = 0.785mm2$. Approximately $6.25e8$ nanoparticles can be deposited on a planar electrode with the same diameter as the graphite electrode to form a layer of nanoparticles. This maximum number was used as a boundary on the estimated number of AuNPs. Knowing that $S_{\text{graphite electrode}} > S_{\text{planar electrode}}$ due to its structure as shown in section 5.2, it is expected that the maximum number of AuNPs required to form a layer in a graphite electrode is higher than $6.25e8$. However, this provides an upper boundary to assess whether the estimated number of deposited AuNPs is acceptable.

Conclusion

A method to compute an estimation of the amount of AuNPs on a surface when the distribution is not homogeneous was presented in this section. A challenging aspect of the method was the time required to record the images for each sample while keeping an acceptable resolution of the image for the ITCN plugin to work.

For future work, it would be advantageous to manage to connect the Python code to compute the amount of deposited AuNPs to the Jython script for the ITCN plugin. Then, the ITCN plugin performance depends on the parameters that are specified by the user. Due to this, there is difficulty to find the most optimized parameters. The plugin FindFoci is an open-source plugin of ImageJ that allows to find the optimized parameters to count particles for a dataset using machine learning and could offer an alternative to the ITCN plugin to get better performances [23].

Chapter 6

Electrophoretic deposition

6.1 Introduction

This chapter presents an attempt to reproduce the electrophoretic deposition (EPD) process from the article *"Gold colloidal nanoparticle electrodeposition on a silicon surface in a uniform electric field"* by Buttard et al. [8]. The difference between the experiment setup of the article and the setup used in this thesis constitutes a challenge. First, the reference article is presented. Then, the materials and methods used for the EPD process are described. Finally, the results are presented and discussed. The deposition process will be characterized using pictures, the characterization method via SEM images described in *Chapter 4*, and electrochemical impedance spectroscopy measurements.

6.2 Presentation of the reference article

In [8], Buttard et al. reported the successful electrophoretic deposition of AuNPs on a planar silicon wafer. The deposition process was characterized according to three figures of merit:

- High density of deposited nanoparticles
- Stability of the deposited film
- Irreversibility of the deposition process

6.2.1 Experimental setup and deposition process

A schematic representation of the deposition process is given in figure 6.1. Voltage is applied to the silicon wafer (anode) with respect to the platinum counter-electrode

(cathode). A uniform electric field **E** across the electrochemical cell creates a force that is applied to the nanoparticles. Because the colloidal gold nanoparticles are negatively charged due to the shell of negative citrate ions (the colloids in figure 6.1), **E** drives the nanoparticles towards the anode by subjecting them to a force $F = qE$. The electrophoretic deposition of AuNPs is explained in more detail in section 2.3.2 in *chapter 1*.

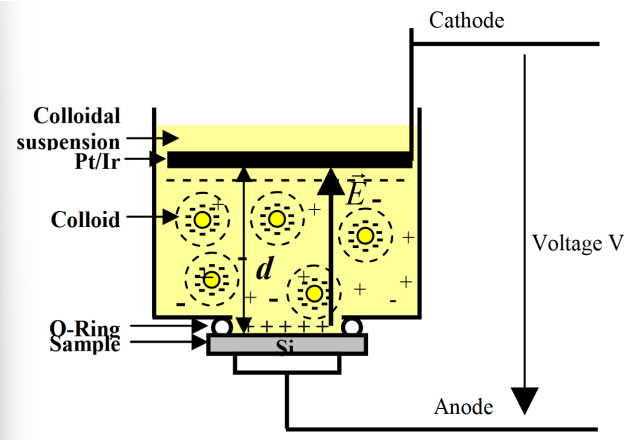

Figure 6.1: Experimental setup of the reference article

The EPD process can be described via the Hamaker equation:

$$w = \frac{2}{3} C \cdot \epsilon_0 \cdot \epsilon_r \cdot \zeta \cdot (\frac{1}{\eta})(\frac{V}{d}) \cdot t \tag{6.1}$$

where w is the weight of deposited nanoparticles, C is the concentration of particles in the solution, ϵ_0 is the permittivity of vacuum, ϵ_r is the relative permittivity of the solvent, ζ is the potential of the nanoparticles, η is the viscosity of the solvent, V is the applied voltage, d is the distance between the electrodes, and t is the time of the deposition process [16]. In the reference article, except for V, t, d, and C, all the other parameters are constant

- the applied voltage: V
- the distance between the anode and cathode: d
- the duration of the deposition process t
- the concentration of AuNPs in the solution: C

6.2.2 Results

High density of deposited AuNPs The silicon wafer was deoxidized before the deposition process. They conducted an experiment where the applied voltage was constant at 40V. The distance between the anode and the cathode was also maintained constant, but the exact value is not specified in the paper. The results of the EPD of AuNPs are shown in figure 6.2. After 10 mins of deposition, the AuNPs were uniformly deposited over the substrate surface with no aggregation. r_0 represents the average distance between the centers of two particles. After 10 minutes of deposition, r_0 saturated at 46.9nm. SEM images were recorded for longer deposition time and were similar to the SEM images after 10 minutes of deposition. Knowing the diameter of the AuNPs was 20 nm, it was concluded that after long deposition time, the EPD process reached saturation, indicating that the highest possible density of AuNPs was deposited.

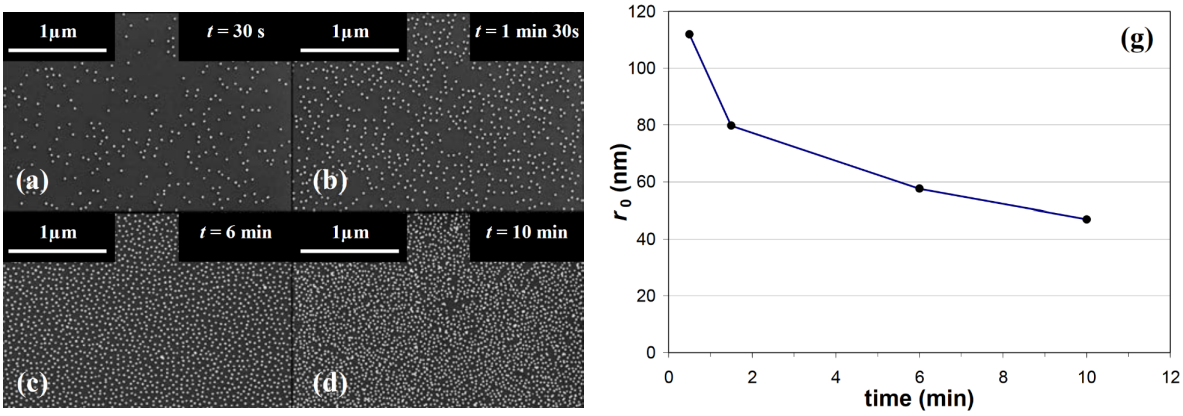

Figure 6.2: (left) SEM images of the EPD of AuNPs after different **t**; (right) average distance between nanoparticles r_0 over time

Stability and irreversibility The stability of the deposited film was tested by dipping the silicon substrate into acidic and basic baths; the composition of these baths was not mentioned in the paper. The irreversibility of the EPD process was tested by applying a reverse electric field to the cell, with the positive voltage applied at the cathode instead of the anode. After each test, no significant modification of the deposited film was observed.

Finally, they tried to change the material of the substrate for a platinum-coated silicon wafer and an oxidized silicon wafer. The results showed no signs of AuNPs deposition on either substrate. They also realized EPD at low electric fields and observed that before a threshold electric field $E_{trans} \approx 80V/m$, the amount of deposited AuNPs was low compared to higher electric fields. With these last

results, they suggested that a dependency on the substrate material exists, and a minimum electrical field is required for the EPD process.

6.3 Materials

Electrodes

The electrodes of the electrochemical cell are all on a PCB as shown in figure 6.3. Per PCB there are eight working electrodes (WE), one counter electrode (CE), and four reference electrodes (RE). The reference electrodes are made of Ag/AgCl ink and the CE and WE are made of graphite ink. The reference electrodes are short-circuited together. The working electrodes are all independent, a different voltage can be applied to each WE.

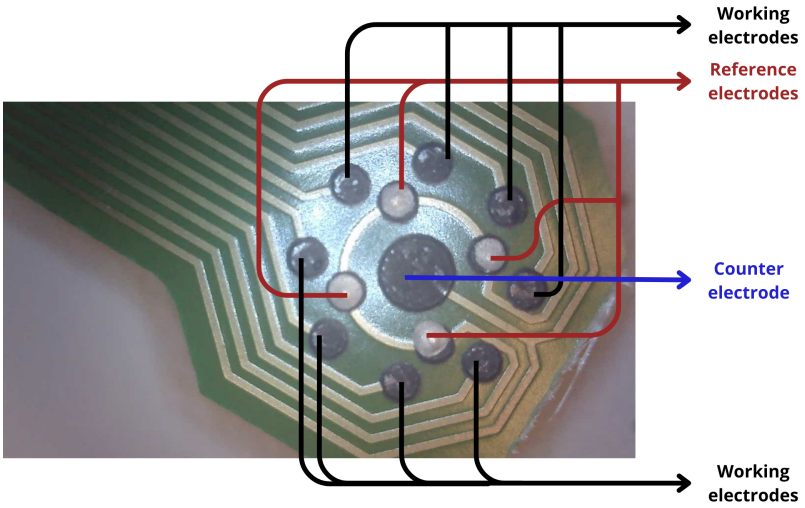

Figure 6.3: Picture of the PCB and its different electrodes

Gold colloidal nanoparticles solution

The gold colloidal nanoparticles solutions used came from Unisensor Nano Flow. The surfactants in the solution are citrate ions. Surfactants prevent the aggregation of the nanoparticles when they are suspended in a solution. Since negative charges repel each other, the particles in the solution stay unaggregated [43]. The diameter of the AuNPs is 40nm, and the concentration of the solution is $8.1e11$ particules/mL.

Ferricyanide/ferrocyanide ($[Fe(CN)_6]^{3/4-}$) solution

The redox couple used for the EIS measurements is the $[Fe(CN)_6]^{3/4-}$ couple. A 5mM $[Fe(CN)_6]^{3/4-}$ solution was used for the EIS measurements. The solution was prepared by dissolving 2.5 mmol of potassium ferricyanide (potassium hexacyanoferrate(III)), $K_3[Fe(CN)_6]$, and 2.5 mmol of potassium ferrocyanide (potassium hexacyanoferrate(II) trihydrate), $K_4[Fe(CN)_6]$, in 500 ml of distilled water.

Equipment

The EPD process and the EIS measurements were done using the potentiostat Autolab PGSTAT302N shown in figure 6.4 and the software Nova [46]. The PCB was connected to the potentiostat via the housing shown in figure 6.5. The switches in the housing allow the application of a voltage to each WE of the PCB. The electrodes and the housing were made by Sami Yunus, a researcher at UCLouvain, ICTEAM.

Figure 6.4: Potentiostat Autolab PGSTAT302N

Figure 6.5: Housing used in the experiments to connect the cables of the potentiostat to the contacts of the electrode

6.4 Method

Cleansing method of the electrodes

The electrodes are cleansed before the deposition process. The cleansing method involves scrubbing the electrodes with an eraser, rubbing them with Kimtech paper, and finally blowing nitrogen onto them.

Complete experimental setup

The complete experimental setup for the EPD and the EIS measurements is shown in figure 6.6.

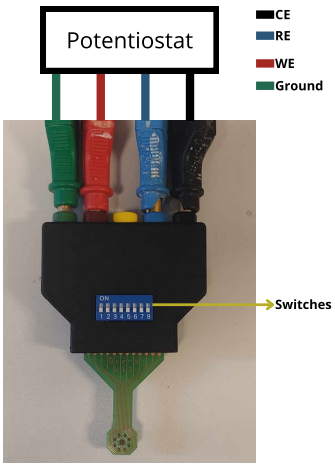

Figure 6.6: Complete experimental setup

Electrophoretic deposition

For the EPD process, a 120µL drop of Colloidal AuNPs is deposited over all the electrodes of the PCB as represented in figure 6.7 and a voltage is applied at the WE with respect to the RE.

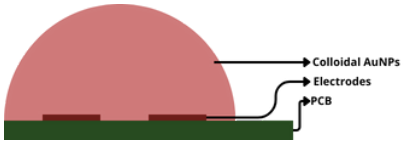

Figure 6.7: Side view of the PCB during the EPD process.

All the parameters for the EPD process are listed in table 6.1. Some parameters were fixed for all experiments, while others were variable. The electrical field lines in the setup of the reference article in figure 6.1 are parallel, and the electric field is uniform. In our experimental setup shown in figure 6.6, it is assumed that the electrical field lines form arcs between the RE and the WE. The drying method used is the removal of the droplet of gold colloidal nanoparticle solution with a micropipette and air-drying of the electrode.

Parameters	Fixed or variable	Value
Applied voltage	variable	/
Duration of the deposition process	variable	/
Distance between WE and RE	fixed	1.5mm
Volume of colloidal AuNPs solution	fixed	120µL
AuNPs Diameter	fixed	40nm
Concentration of the AuNPs solution	fixed	8e11 AuNPs/mL
Concentration of surfactant in the solution	fixed	/ (not mentioned in the datasheet of AuNPs)
Charge of the surfactant	fixed	negative

Table 6.1: Parameters of the EPD

EIS measurements

EIS measurements were carried out in the presence of 5mM a $[Fe(CN)_6]^{3/4-}$ solution. The frequency range for the measurements was [0.01Hz;100kHz], and a DC potential of +0.2V was superposed to the small AC signal. The *Frequency Analyser (FRA) measurement* tool of the Nova software [46] was used to perform the EIS measurements. The DC potential, 0.2V, corresponds to what is usually used in the literature when the $[Fe(CN)_6]^{3/4-}$ redox couple is used with an Ag/AgCl reference [30]. A 120 µL drop of $[Fe(CN)_6]^{3/4-}$ solution was deposited on the PCB to do the measurement as represented in figure 8.1.

Figure 6.8: Experimental setup for the EIS measurements

The measurements were fitted to an equivalent Randles circuit using the tool *Fit and simulation* of the Nova software. The equivalent randles circuit is shown in figure 8.2. A constant phase element (CPE) was used instead of an ideal capacitor for the equivalent circuit. The roughness of the initial graphite electrode causes non-ideal behavior of the double-layer capacitance as explained in the section 2.2 related to electrochemical impedance spectroscopy in *Chapter 1*.

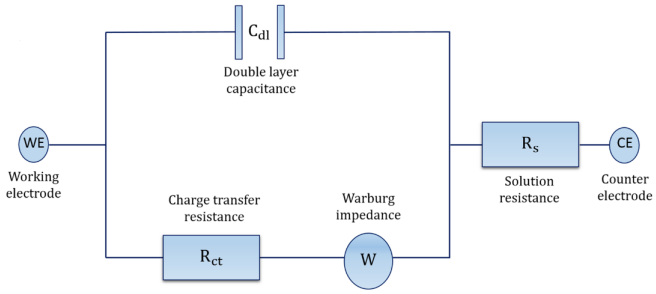

Figure 6.9: Equivalent Randles Circuit

Convention used for the measurements and depositions

Lastly, for every deposition in *Chapter 6*, *7*, and *8*, the working electrode 1 represented in figure 6.10 was used for the estimation of the amount of deposited AuNPs using the characterization method via SEM and EIS measurements.

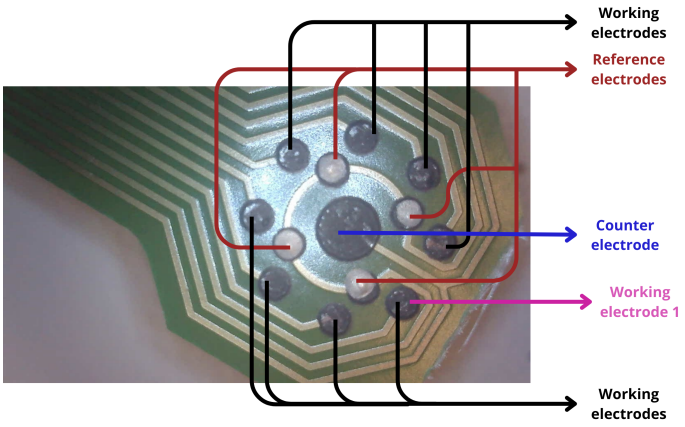

Figure 6.10: Working electrode used for EIS measurements and SEM characterizations

6.5 Results and discussion

6.5.1 Preliminary EPD deposition

The results of the first preliminary electrophoretic deposition (EPD) are examined in this section. The parameters for these depositions are referenced in table 6.2. When those EPD were realized, a different potentiostat from the Autolab was used, and it was limited to 5V. A voltage source limited to 27V was used to apply higher voltages instead of the potentiostat. The positive voltage was applied to the WE and the CE and RE were short-circuited to the ground.

	Duration of the deposition
EPD at 27V	10 min
EPD at 5V	10 min

Table 6.2: Parameters of the first electrophoretic depositions

Comparison between figures 6.11 and 6.12 shows that nanoparticles were effectively deposited on the graphite electrode after the EPD at 27V. Comparison between the figures 6.13 and 6.14 suggests that less AuNPs were deposited after the EPD at 5V compared to the EPD at 27V. SEM images of the EPD at 5V, shown in figure 6.15 and 6.16, show that AuNPs were effectively deposited. This difference could be explained via the Hamaker formula 6.1. For these depositions, only V and t are free parameters. C and d are kept constant. From this equation, we can understand that since $5V < 27V$ but since the same deposition time is used for both depositions, less AuNPs are expected to be deposited on the graphite electrode of the 5V deposition.

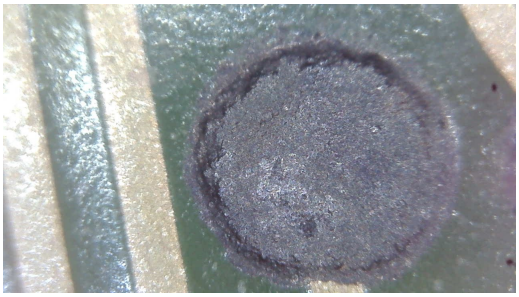

Figure 6.11: Picture of the WE before the EPD process at 27V

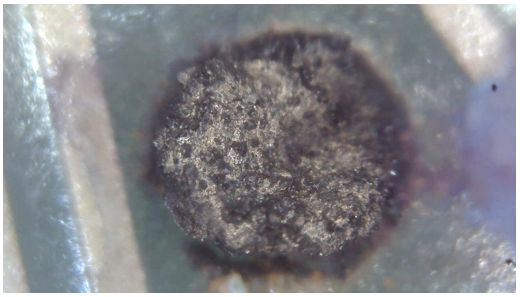

Figure 6.12: Picture of the WE after the EPD process at 27V

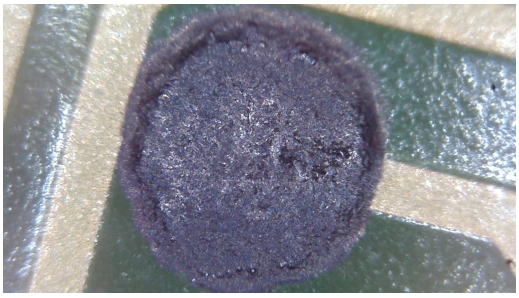

Figure 6.13: Picture of the WE before the EPD process at 5V

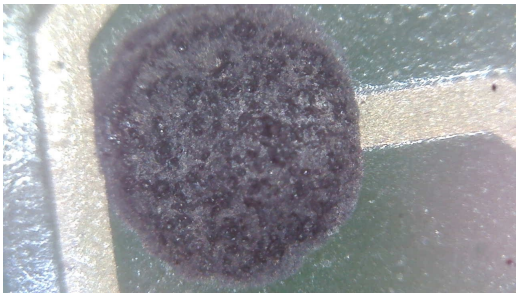

Figure 6.14: Picture of the WE after the EPD process at 5V

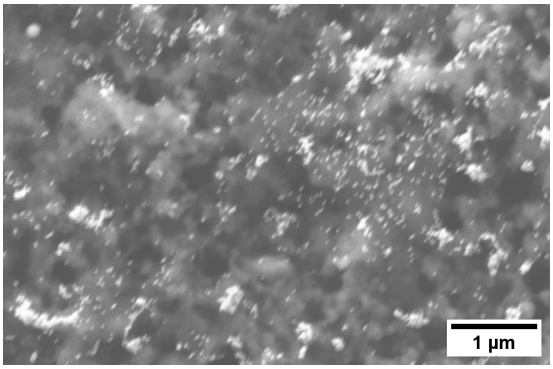

Figure 6.15: SEM image of the WE after the EPD process at 5V; 17.81kx magnification

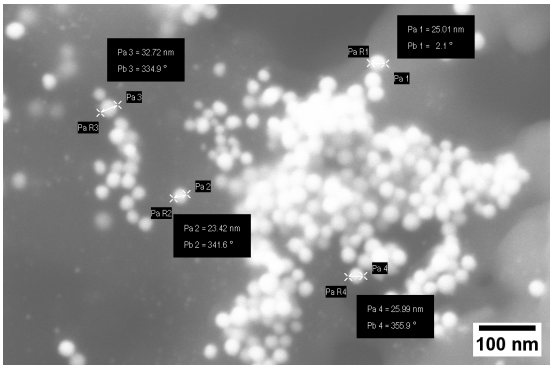

Figure 6.16: SEM image of the WE after the EPD process at 5V; 120.61kx magnification

Two problems arise with the deposition process: **degradation of the electrochemical cell and degradation of the working electrodes**. In figures 6.17 and 6.18, the CE and RE were damaged due to the deposition process. Since the same electrochemical cell should be used for later measurements with the sensor,

this is a problem. Furthermore, the working electrodes of both depositions were also damaged. The working electrode of the EPD at 27V was degraded to the point where the graphite was coming off from the PCB. Therefore, it could not be analyzed via SEM. However, the working electrode of the EPD at 5V could be analyzed via SEM. In figures 6.19 and 6.21, it can be seen that compared to the normal graphite electrode 6.20, pores into the electrode were created following the deposition process.

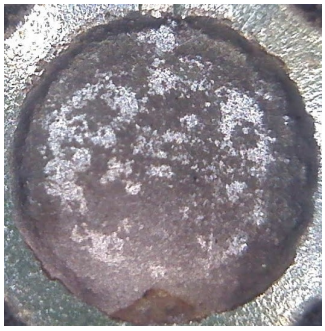

Figure 6.17: Picture of the CE after the EPD at 27V and 5V

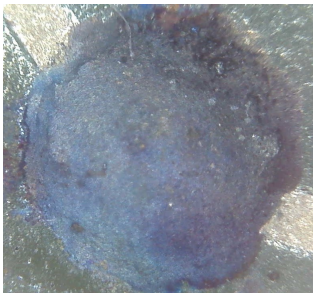

Figure 6.18: Picture of the RE after the EPD at 27V

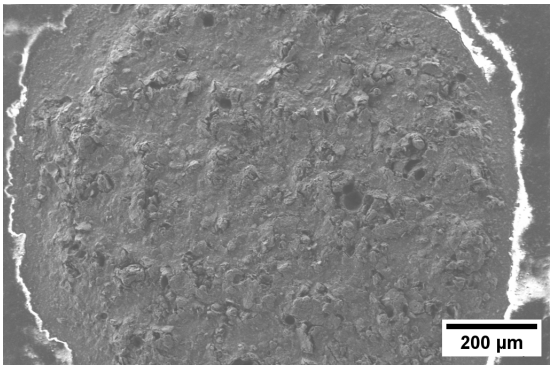

Figure 6.19: SEM image of the WE after the EPD at 5V; 94x magnification

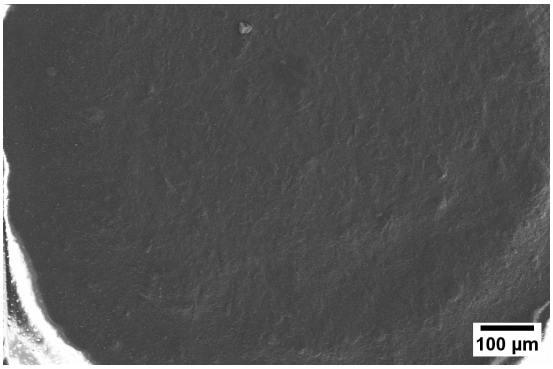

Figure 6.20: SEM image of a graphite electrode, no EPD was performed on this electrode

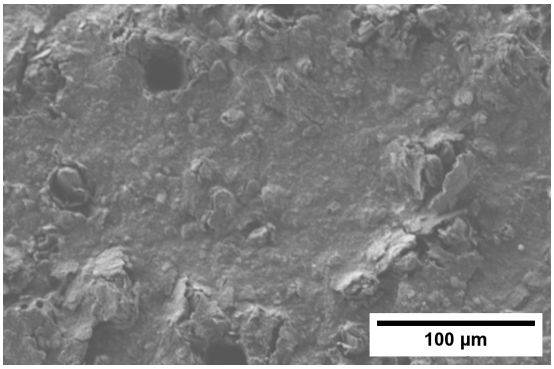

Figure 6.21: SEM image of the WE after the EPD at 5V; 329x magnification

These first experiments demonstrated that **electrophoretic deposition of AuNPs was possible, but adjustments must be made to avoid electrode degradation**. The next section presents the cause of the deterioration and attempts to solve the problem.

6.5.2 Origin of the electrode degradation

When an aqueous solution is used in an electrochemical cell, water electrolysis occurs and results in the formation of hydrogen and oxygen bubbles.

$$2H_2O_{(liq)} \rightarrow O_{2(g)} + 2H_{2(g)}$$

Typically, water electrolysis occurs when there is around a 1.23V difference between the RE and WE. The preliminary results gave the confirmation that the electrophoretic method works. However, due to the creation of hydrogen and oxygen bubbles that get trapped inside the graphite, the electrodes are damaged. This constrains the maximum voltage that can be applied.

6.5.3 Hypothesis and solutions for the deterioration of the electrodes

Two attempts were made to solve the problem of electrode deterioration.

- Attempt 1: The surface of the electrode in the reference article is bigger than the surface of the electrode in our setup. This might suggest that the applied potential should not be the same.
- Attempt 2: Identifying a threshold voltage low enough to prevent excessive hydrogen/oxygen bubble formation while still allowing the EPD process to occur.

Attempt 1: Long EPD process at low voltage

The surface of the silicon waffer in [8] was $S_{ref} = 0.385[cm^2]$. The electrode in our experimental setup has a diameter of 1mm, so $S_{exp} = 0.0078[cm^2]$. Applying the rule of three suggests that the voltage should be 0.81V. This leads to the electrical field E being smaller, and the force applied to AuNPs is smaller. According to Hamaker's equation 6.1, if the applied voltage is reduced, to have the same amount of deposited AuNPs on the electrode, the duration of the deposition process should be increased. Therefore, EPD was realized by applying a small voltage, 1V, for 24h. A control experiment was also realized. The parameters of the EPD process are given in table 6.3.

	Duration of the deposition
EPD at 1V	24h
Control experiment (0V applied)	24h

Table 6.3: Parameters of the 24h EPD at low voltage

The setup for the EPD at 1V for 24 hours, shown in figure 6.22, is different from the one presented in figure 6.6 in the *Method* section 6.4. Since a drop of gold colloidal solution would evaporate before the end of the deposition process, the PCB was dipped in a pot filled with gold colloidal solution. Comparison between the SEM images of the 24h EPD process shown in figures 6.23 and 6.26 and of the SEM images of the control experiment in figures 6.25 and 6.26 suggested that the deposition was successful. The WE of the 24h EPD showed a better coverage of AuNPs compared to the control experiment.

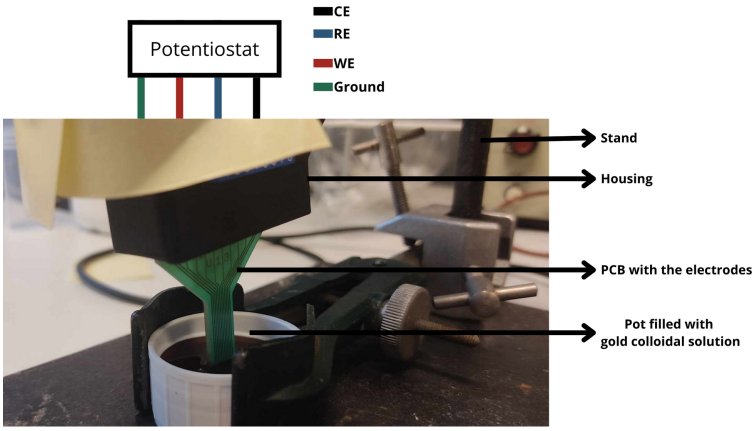

Figure 6.22: Experimental set-up for the 24h EPD

Figure 6.23: SEM image of the WE after the 24h EPD; 5.35kx magnification

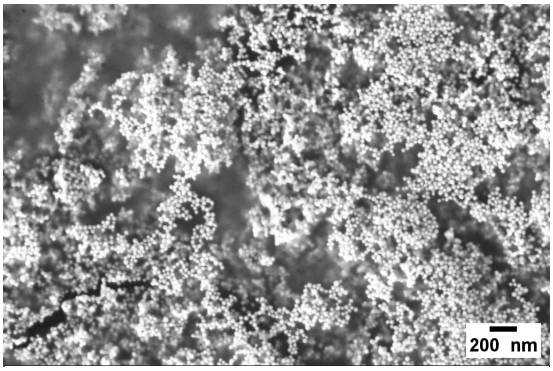

Figure 6.24: SEM image of the WE after the 24h EPD; 28.23kx magnification

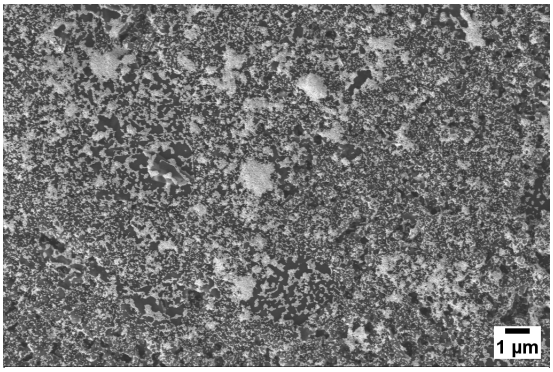

Figure 6.25: SEM image of the WE after the 24h control experiment; 5.13kx magnification

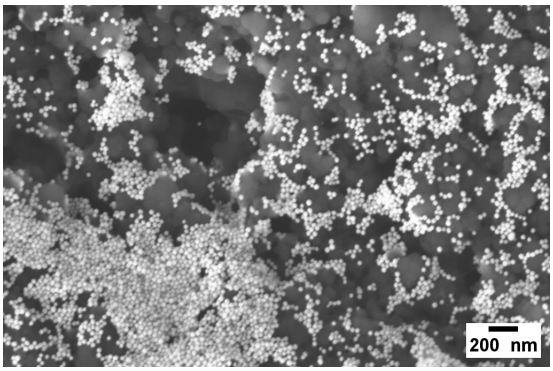

Figure 6.26: SEM image of the WE after the 24h control experiment; 30.68kx magnification

However, to realize the experiment, the amount of gold colloidal solution used was too important compared to the amount of solution we possessed. 9mL of solution was used, and the solution came in vials of 1.5mL. Moreover, the solution in the pot could not be reused for other experiments because the AuNPs contained in the solution because the AuNPs aggregated and sedimented at the bottom of the pot because the solution was exposed to air for a long time. Hence, another setup was made and is shown in figure 6.27. In this setup only a 120 µL droplet of gold colloidal solution was necessary. The PCB was enclosed in a petri plate covered with parafilm in this setup. There is a damp paper towel to ensure that the space is saturated in humidity to avoid the evaporation of the drop of gold colloidal nanoparticles solution.

One last long EPD process was realized, and the parameters are shown in table

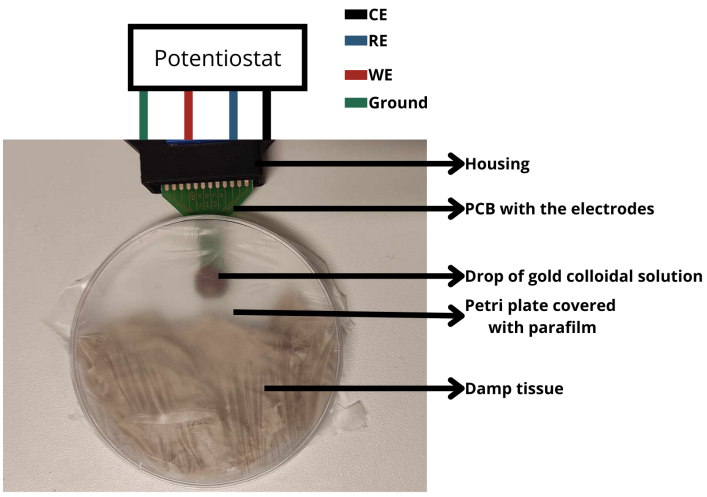

Figure 6.27: Second experimental setup for long EPD process

6.4. The duration of the deposition was different from the previous deposition (24h), but it was expected that after 12h, if the deposition process is effective, a significant difference should be observable between the WE of the 12h EPD and its control experiment. Comparison between the results of the EPD at 1V for 12h in figure 6.28 and its control experiment in figure 6.30 shows no significant difference in terms of the amount of deposited AuNPs. Furthermore, less nanoparticles were deposited with the 12h EPD at 1V, as shown in figures 6.28 and 6.29 compared to the results of the 24h EPD at 1V as shown in figures 6.26 and 6.23. From these results, it was unclear whether, when the EPD process is long and at low voltage, the AuNPs are effectively deposited in the WE mostly due to the applied voltage.

	Duration of the deposition
EPD at 1V	12h
control experiment (0V)	12h

Table 6.4: Parameters of the second long EPD process. The duration of the deposition process was 12h

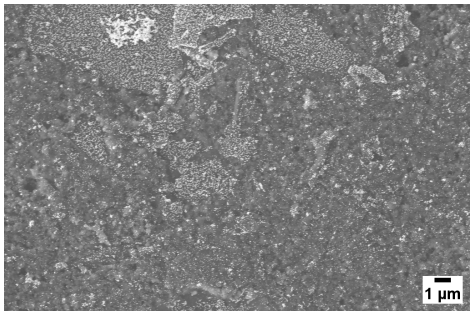

Figure 6.28: SEM image of the WE after the EPD at 1V for 12h; 4.17kx magnification

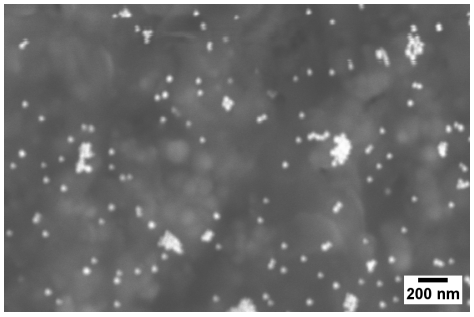

Figure 6.29: SEM image of the WE after the EPD at 1V for 12; 34.11kx magnification

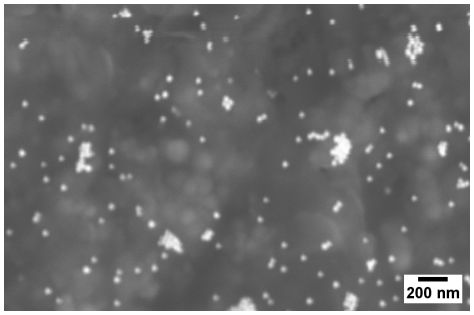

Figure 6.30: SEM image of the 12h control experiment; 34.11kx magnification

Attempt 2: Identification of a threshold voltage for the EPD process

From the preliminary results 6.12, we observed that the electrophoretic deposition process worked at high voltages (27V), but the graphite electrode was damaged in the process. In the reference article, [8], they observed that there exists a threshold electric field. If the electric field was not high enough, the deposition process was still occuring, but the density of deposited nanoparticles was low compared to when the electric field exceeded the threshold. Since the electric field $E = \frac{V}{d}$ and d is fixed for the deposition process in our experimental setup, only V can change the applied electric field. Due to the constraint of water electrolysis, EPD was performed at 1V, 1.3V, and 1.5V. Additionally, to avoid other effects that could influence the deposition of AuNPs, t was set to 30 minutes. This is long compared to the reference article, where the longest deposition time was 10 minutes. However, since lower voltages are used, it is expected, according to Hamaker's formula 6.1, that t should be increased. The amount of deposited nanoparticles was computed using SEM images and the method presented in *Chapter 4*. All of the SEM images are available in the appendices. There is not a significant difference

in terms of the number of AuNPs deposited. The experience at 1.5V might show a better coverage of the electrode, but it is not clear if it is exactly due to the electrophoretic deposition process since there is not a significant difference with the estimated number of deposited nanoparticles. All the SEM images used for the characterization method can be found in the appendices in chapter B.

	Duration of the deposition	Number of deposited AuNPs
Control experiment (0V)	30 min	1.56e8
EPD at 1V	30 min	1.69e8
EPD at 1.3V	30 min	1.58e8
EPD at 1.5V	30 min	1.79e8

Table 6.5: Parameters of the EPD processes and the amount of deposited AuNPs

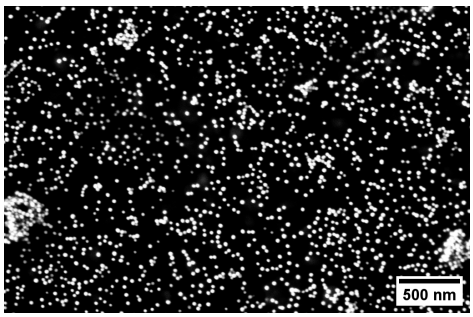

Figure 6.31: SEM image of the WE after the control experiment

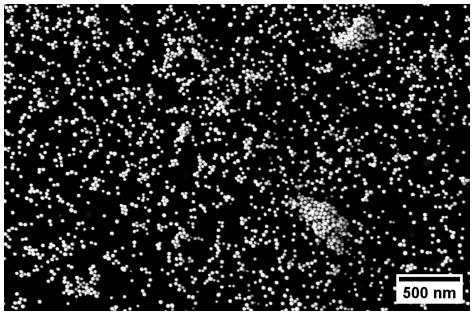

Figure 6.32: SEM image of the WE after the 1V EPD process during 30 min; 30kx magnification

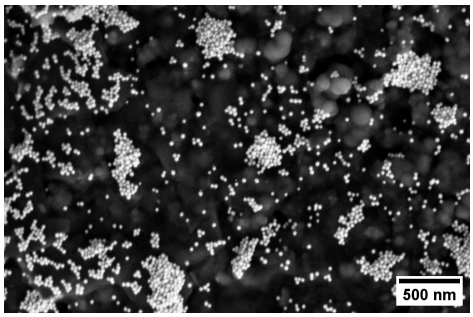

Figure 6.33: SEM image of the WE after the 1.3V EPD process during 30 min; 30kx magnification

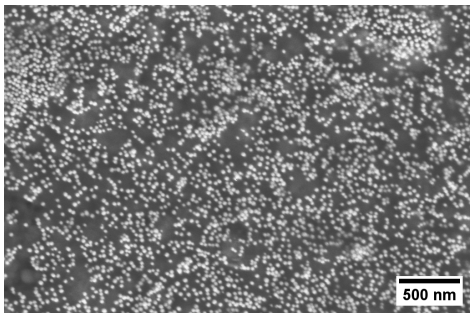

Figure 6.34: SEM image of the WE after the 1.5V EPD process during 30 min; 30kx magnification

6.5.4 First EIS measurements of electrode modified with deposited AuNPs

The EIS measurements for the EPD at 1V during 30 minutes and the control experiment are plotted in Nyquist diagrams in figures 6.35 and 6.36 respectively. An equivalent circuit was fitted to the data for both depositions, and the values of the equivalent circuit elements are shown in tables 6.6 and 6.7. These first EIS measurements indicated that there is indeed a reduction of R_{ct} when AuNPs are deposited on the electrode. A constant phase element (CPE) was used instead of an ideal capacitor for the equivalent circuit. The roughness of the initial graphite electrode causes non-ideal behavior of the double-layer capacitance. The control experiment and the 1V experiments both lead to a decrease of R_{ct}.

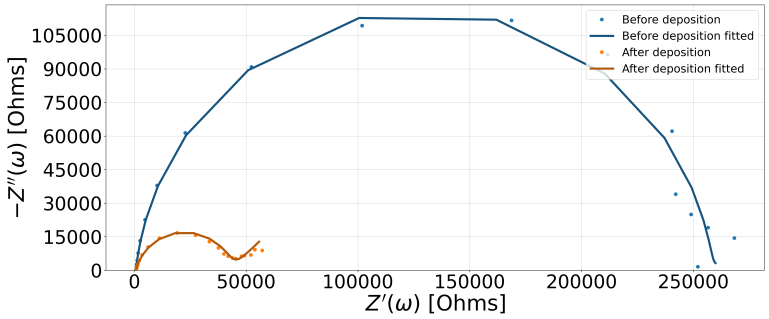

Figure 6.35: Nyquist plot of the EIS measurement of the WE before and after the EPD at 1V during 30 min

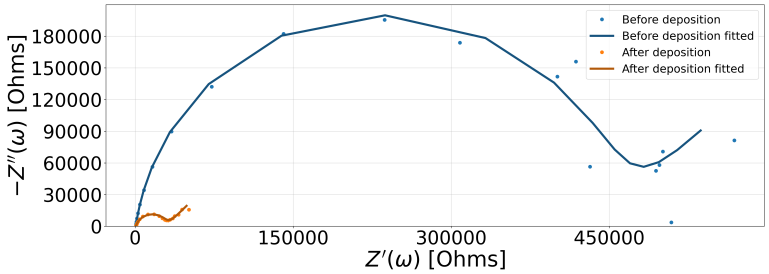

Figure 6.36: Nyquist plot of the EIS measurements of the WE before and after the control experiment

	Rs [Ohm]	**Rct** [Ohm]	**W** (Y_0) [µOhm·s$^{(1/2)}$]	**CPE** (Y_0) [nOhm·s^N]	**N**
EPD at 1V	640	453k	10.4	28.3	0.911
Control experiment	713	258k	536	35.8	0.933

Table 6.6: EIS measurement of the WE of the 1V EPD experiment and the control experiment before the deposition process

	Rs [Ohm]	**Rct** [Ohm]	**W** (Y_0) [µOhm·s$^{(1/2)}$]	**CPE** (Y_0) [nOhm·s^N]	**N**
EPD at 1V	705	42.7k	70.9	123	0.848
Control experiment	702	29.3k	46.7	236	0.819

Table 6.7: EIS measurement of the WE of the EPD at 1V and the control experiment after the deposition process

6.6 Conclusion of the electrophoretic deposition process

With the preliminary results, proof was given that the electrophoretic deposition process works, but the electrodes were damaged due to water electrolysis.

The objective of the thesis is to increase the sensitivity of an impedimetric immunosensor by reducing the charge-transfer resistance of the electrode before functionalization. The first EIS measurements before and after AuNPs deposition showed a reduction of R_{ct} when AuNPs are deposited on an electrode.

In future work, a solution to the formation of hydrogen/oxygen bubbles during the EPD process could be the bubble-free aqueous electrophoretic deposition process demonstrated in [6]. This method is based on the application of a square-wave pulse potential instead of a DC potential. Less hydrogen/oxygen bubbles are created during the deposition process when the width of the pulse is decreased. This method was used to deposit aluminum particles (diameter=0.20µm) on a substrate. Results are shown in figure 6.37. To our knowledge, the method has yet to be tested with gold nanoparticles, but it could offer a solution.

Another solution would be to change the electrode material. In [67], electrophoretic deposition of AuNPs on graphite carbon plate electrodes was achieved with applied voltages of 5V and 10V. This paper showed that electrophoretic deposition of AuNPs on graphite substrate is possible. In our experimental setup, the electrodes were made of graphite ink. In our experimental setup, the electrodes

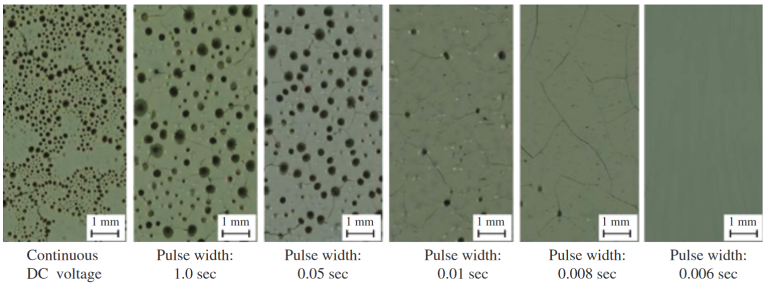

Figure 6.37: Bubble-free electrophoretic deposition of aluminum particles for different voltage pulse width [6]

were made of graphite ink. It is supposed that due to the graphite ink not being as solid as graphite carbon plate, air bubbles could get trapped inside the graphite ink electrode and damage them when they exploded. Using a solid substrate could solve the problem.

Finally, since the control experiment showed good results in terms of the number of AuNPs deposited and for the decrease of R_{ct}, the technique used to make the control experiment, drop casting, is more investigated in the next chapter.

Chapter 7

Drop Casting

7.1 Introduction

In the previous chapter, the EPD process was used to deposit AuNPs on graphite electrodes. Through the first EIS measurements presented in subsection 6.5.4, it was already concluded that the charge-transfer resistance can be reduced via the deposition of AuNPs on graphite electrodes. However, there was an issue, the electrode was damaged in the process. But, it was noticed that the control experiment, which was made via a modified version of the drop casting method, presented good results in terms of the number of AuNPs deposited and a decrease of the charge-transfer resistance. That deposition method is investigated in this chapter.

7.2 Method

Cleansing of the electrodes

The electrodes are cleansed according to the method presented in subsection 6.4.

Drop casting on single electrode

Drop casting is done by depositing a drop of gold colloidal solution onto the electrode and letting it dry, as presented in figure 7.1.

Drop casting on multiple electrodes

A 120 µL drop of gold colloidal solution was deposited over all the electrodes, compared to the original drop casting method shown previously, where the drop is deposited only on a single electrode as shown in figure 7.1.

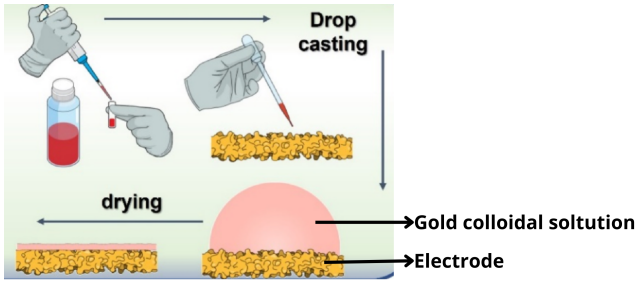

Figure 7.1: Drop casting method [54]

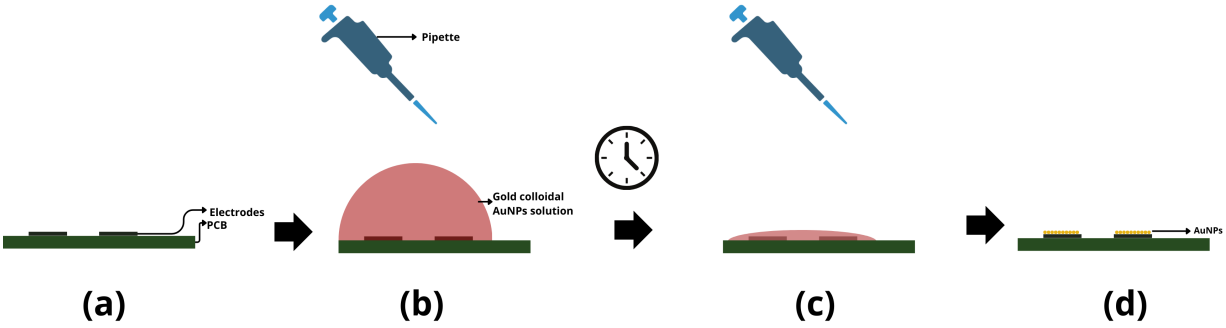

Figure 7.2: Modified drop casting procedure; (b) a drop of gold colloidal solution is deposited over all the electrodes of the PCB, (c) after a time t, the solution is removed partially, (d) the solution is left to dry and a film of AuNPs is formed

7.3 Results and discussion

7.3.1 Drop casting on single electrode

The original drop casting method presented in figure 7.1 was first tested since less gold colloidal solution (5µL) is required for the deposition process. It could be observed that more nanoparticles are deposited on the edges of the electrode compared to the center in figure 7.3. This is the coffee-ring effect.

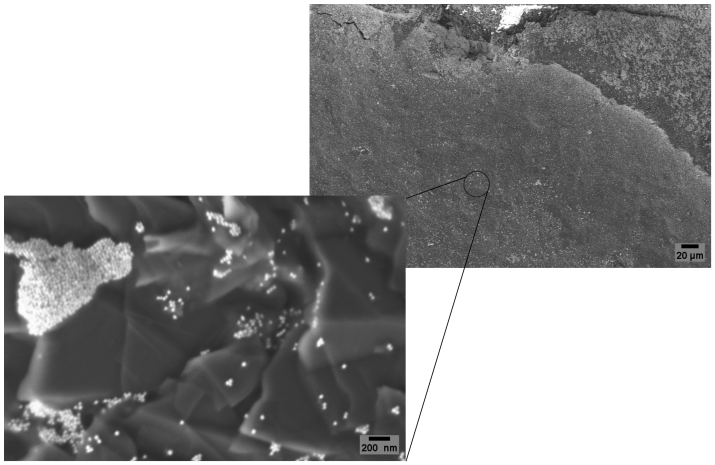

Figure 7.3: Coffee-ring problem

In the previous chapter, control experiments for the EPD process were realized with the modified drop casting method shown in figure 7.2. Coffee-ring could be observed on the PCB, but not on the WE. It is supposed that since the WE on the PCB are on the edges of the drop, this works in favor of the coffee-ring effect. Therefore, this modified version of the drop casting will be used in the next sections.

7.3.2 Investigation of the influence of the parameters on the modified drop casting method

The first step in designing the deposition process was to decide what parameters can influence the technique presented in figure 7.2. First, the parameters and their minimum and maximum values were decided and are written in table 7.1.

Parameter	Minimum value	Maximum value
Temperature	25°C	30°C
Concentration	8e11 AuNPs/mL	16e11 AuNPs/mL
Environment saturated in humidity	No	Yes
Time	30min	2h

Table 7.1: Parameters of the modified drop casting deposition process

Four parameters are used: the temperature, the humidity of the environment, the concentration of the gold colloidal solution, and the duration of the deposition process. The coffee-ring effect is linked to the non-uniform evaporation of the drop, as explained in section 2.3.2. The humidity and temperature criteria impact the

evaporation of the droplet, which is why those parameters were chosen. The setup in figure 6.27 was used to saturate the environment with humidity. But this time, no potentiostat was involved in the deposition process. Due to time constraints, an optimized experimental design was generated to evaluate the effects of parameters by conducting the least amount of experiments. The experimental matrix shown in table 7.2 was designed for optimizing the D-optimal criterion, which focuses on the parameter estimations. The matrix was generated by the statistical JMP software [57]. The number of deposited AuNPs after each deposition process is also given. The SEM images used for the characterization method are all in Chapter C.

	Time	Temperature	Concentration [#AuNPs/mL]	Humidity	Number of deposited AuNPs
Electrode 1	30min	25°C	8e11	No	1.67e8
Electrode 2	2h	25°C	16e11	No	2.86e8
Electrode 3	2h	30°C	8e11	Yes	2.24e8
Electrode 4	30min	30°C	16e11	No	4.01e8
Electrode 5	2h	25°C	16e11	Yes	3.88e8
Electrode 6	2h	30°C	8e11	Yes	1.5e8
Electrode 7	2h	30°C	16e11	No	1.74e8
Electrode 8	30min	30°C	16e11	Yes	2.42e8
Electrode 9	30min	25°C	16e11	Yes	3.37e8
Electrode 10	30min	25°C	8e11	Yes	2.10e8
Electrode 11	2h	25°C	8e11	No	2.034e8
Electrode 12	30min	30°C	8e11	No	1.77e8

Table 7.2: Experiments to determine the influence of the parameters

The number of deposited AuNPs for each electrode was used to construct a linear model to explain the deposition process according to the chosen parameters as shown in figure 7.5. The estimations of the parameters are given in figure 7.6. In this case, the intercept was found to have no statistical significance. The p-value for each parameter was evaluated and is shown in table 7.3. Only the concentration has a statistically significant effect on the deposition process since the p-value is smaller than 0.05. Therefore, a last experiment was done in the next section in order to assess the effect of the concentration on the deposition process.

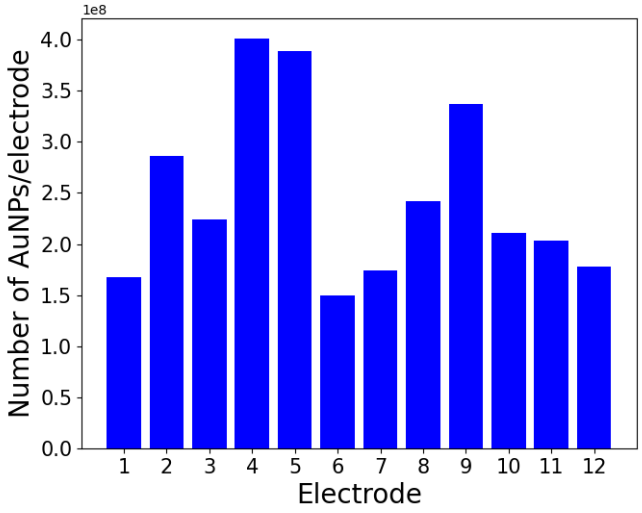

Figure 7.4: Number of deposited AuNPs per electrode

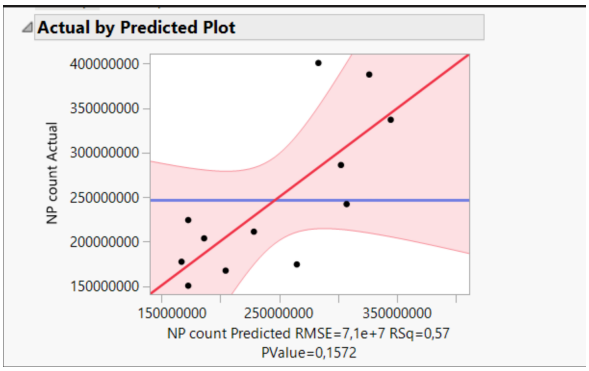

Figure 7.5: Prediction model of the number of deposited AuNPs with the chosen parameters, the red zone corresponds to the confidence interval

Parameter Estimates

Term		Estimate
Intercept	Biased	293583333
Time		-202777,8
Temperature		-7476667
Concentration		0,0001449
Humidity Saturation[no]		-11958333

Figure 7.6: Estimated parameters of the linear model

Parameter	pvalue
Concentration	0.026
Temperature	0.39
Humidity	0.58
Time	0.67

Table 7.3: pvalue of each parameter.

7.3.3 Variation of the number of deposited AuNPs with respect to the concentration of gold colloidal solution

An experiment was conducted where the concentration of the gold colloidal solution (C) in [#AuNPs/mL] was varying. Depositions with C=8e11, C=16e11, C=24e11, and C=32e11 [#AuNPs/mL] were realized. Since in the previous section, the deposition of AuNPS on electrodes 2 and 11 was realized with C=8e11 and C=16e11 for 2h; they were reused for the comparison in this experiment. The number of deposited AuNPs for each electrode is plotted in figure 7.8. In terms of the number of deposited AuNPs, we can observe that there is a significant difference between the depositions with C = 8e11 and C = 16e11 compared to the depositions using C = 24e11 and C = 32e11. The coverage of the electrode surface with AuNPs is also more important for depositions with C = 24e11 and C = 32e11 as shown in figures 7.11 and 7.12 compared to depositions with C = 8e11 and C = 16e11 as shown in figures 7.9 and 7.10.

In the case where C = 32e11, cracks in the film could be observed. There is one hypothesis for this film structure. When changing the concentration of the initial solution from 8e11 to 32e11, the solution was centrifuged and resulted in a solution with the AuNPs at the bottom of the vial and the solvent separated, as shown in figure 7.7. Due to the solvent removal, the AuNPs tended to aggregate more than in the solution with the initial concentration (8e11). This might have impacted the film formation in figure 7.12. The SEM images used for the characterization method are all in Chapter D in the appendices.

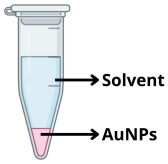

Figure 7.7: Centrifuged gold colloidal solution

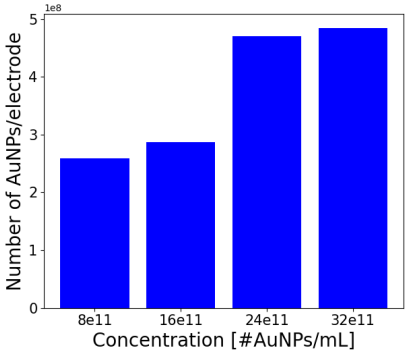

Figure 7.8: Variation of the number of nanoparticles with respect to the concentration

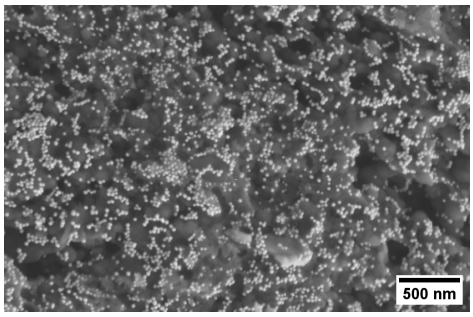

Figure 7.9: SEM image of the WE after the deposition with a solution of gold colloidal with C=8e11; 2kx magnification

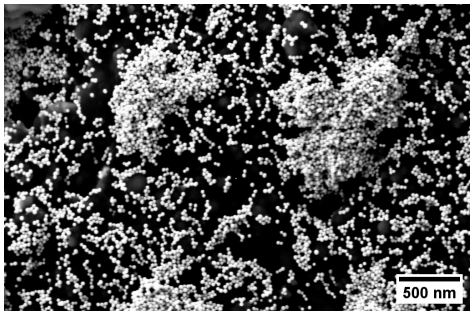

Figure 7.10: SEM image of the WE after the deposition with a solution of gold colloidal with C=16e11; 2kx magnification

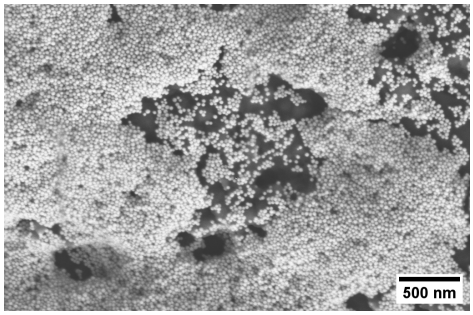

Figure 7.11: SEM image of the WE after the deposition with a solution of gold colloidal with C=24e11; 30kx magnification

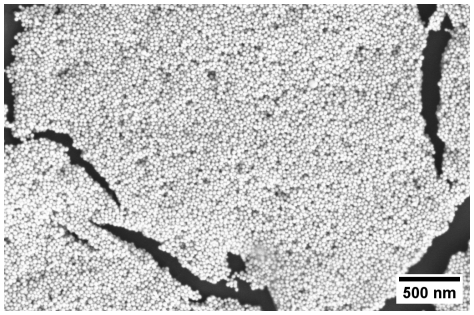

Figure 7.12: SEM image of the WE after the deposition with a solution of gold colloidal with C=32e11; 30kx magnification

7.3.4 Reproducibility

The reproducibility of the deposition process for the electrodes of the same PCB is studied in this section. The analysis was only qualitative, using SEM images. Figures 7.13 - 7.20 show the eight working electrodes of the PCB for the deposition with C = 32e11 [#AuNPs/mL] during 2h in subsection 7.3.3. These images show that even between the electrodes of the same PCB, the density of AuNPs varies between the electrodes. In figure 7.20, compared to the other electrode, significantly less nanoparticles were deposited.

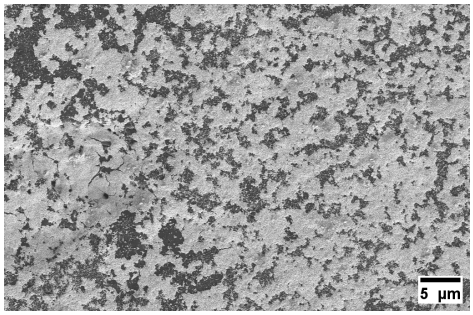

Figure 7.13: SEM image of the WE 1 after the deposition with a solution of gold colloidal with C=32e11; 2kx magnification

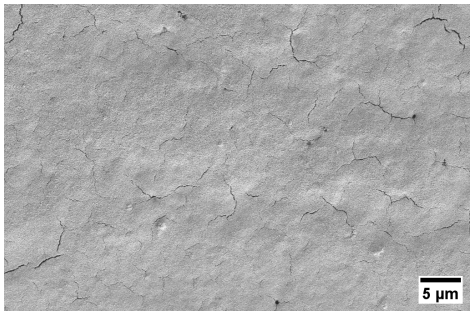

Figure 7.14: SEM image of the WE 2 after the deposition with a solution of gold colloidal with C=32e11; 2kx magnification

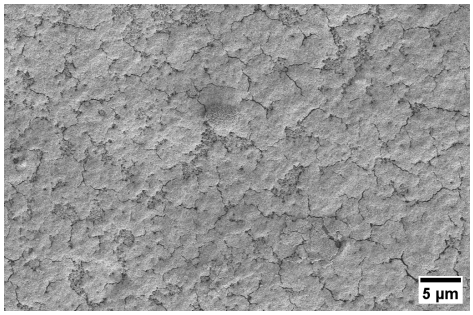

Figure 7.15: SEM image of the WE 3 after the deposition with a solution of gold colloidal with C=32e11; 2kx magnification

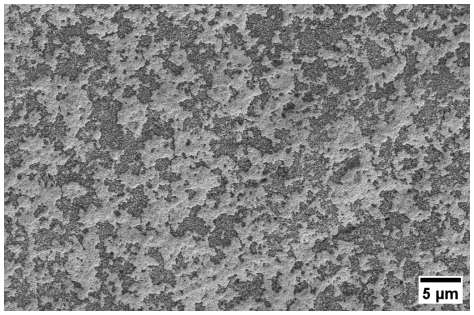

Figure 7.16: SEM image of the WE 4 after the deposition with a solution of gold colloidal with C=32e11; 2kx magnification

7.3.5 Stability

The stability of the deposited film of AuNPs is studied in this section. In the reference article used for the electrophoretic deposition chapter 6.2, they analyzed the stability of the deposited film by subjecting the sample to acidic and basic baths. The exact composition of these baths was not provided. However, given the intended use of the final biosensor in the healthcare sector, it did not seem relevant to use acidic and basic baths to test the stability of the deposited film of AuNPs in this thesis. The stability of the deposited film was evaluated by running a thin stream of distilled water and a thin stream of physiological serum over the sample. Due to time constraints, stability was only observed qualitatively via SEM images. After water rinsing, fewer nanoparticles may be present, but a substantial amount remains on the electrode surface, as shown in figure 7.22. Figure 7.23 shows that

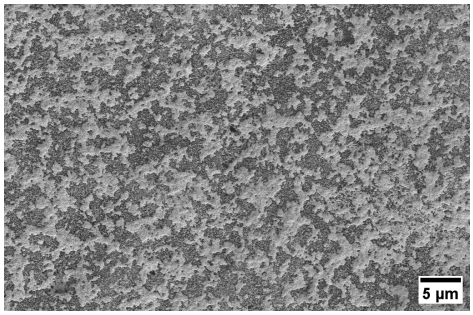

Figure 7.17: SEM image of the WE 5 after the deposition with a solution of gold colloidal with C=32e11; 2kx magnification

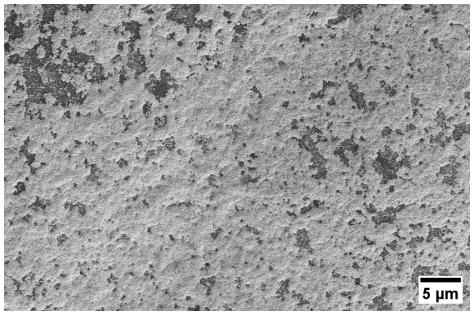

Figure 7.18: SEM image of the WE 6 after the deposition with a solution of gold colloidal with C=32e11; 2kx magnification

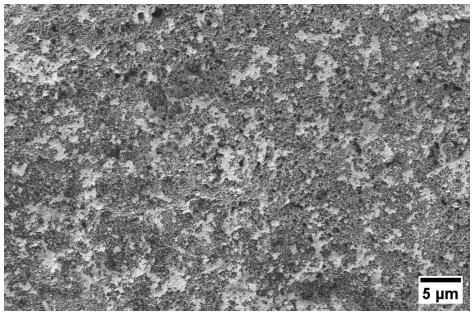

Figure 7.19: SEM image of the WE 7 after the deposition with a solution of gold colloidal with C=32e11; 2kx magnification

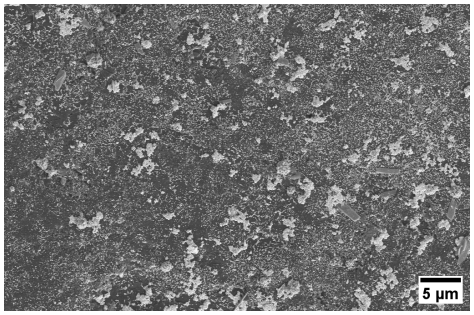

Figure 7.20: SEM image of the WE 8 after the deposition with a solution of gold colloidal with C=32e11; 2kx magnification

rinsing with physiological serum does not affect the attachment of the AuNPs to the surface. It was used because the presence of salt could impact the atmosphere around the AuNPs and lead to film instability. Finally, abrasive friction was also tested, as shown in figure 7.24. The film does not resist abrasive friction.

7.3.6 Economical aspect of the deposition process

For the deposition using gold colloidal nanoparticles solution with a concentration of 32e11 particles/mL, a drop of 120µL was used. The drop contains 3.84e11 nanoparticles, but only 4.84e8 nanoparticles were deposited onto one electrode. If we assume the same amount was deposited on all electrodes (which was not the case as seen in the section about reproducibility 7.3.4), 3.87e10 nanoparticles should be deposited, which represents about 1% of the amount of AuNPs present

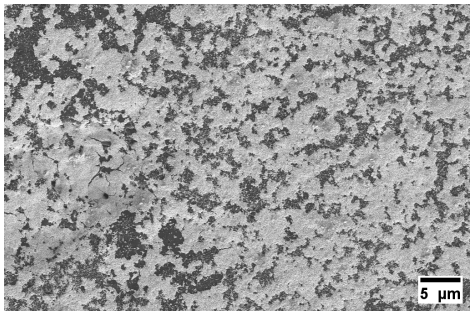

Figure 7.21: SEM image of the WE after the deposition with a solution of gold colloidal with C=32e11; 2kx magnification

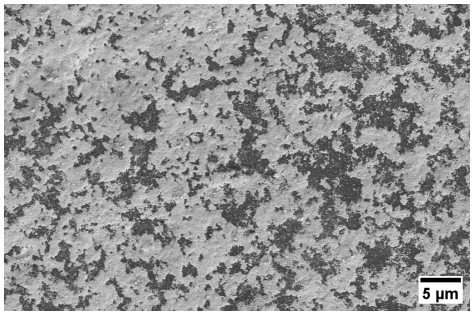

Figure 7.22: SEM image of the WE after the deposition with a solution of gold colloidal with C=32e11 and water rinsing; 2kx magnification

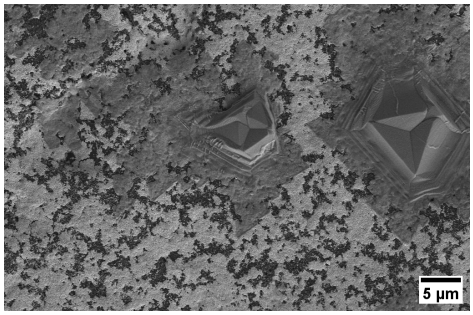

Figure 7.23: SEM image of the WE after the deposition with a solution of gold colloidal with C=32e11 and water rinsing and rinsing with physiological serum; 2kx magnification

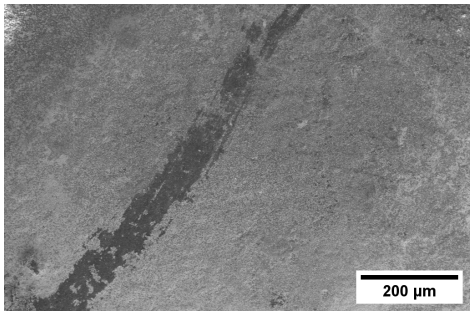

Figure 7.24: SEM image of the WE after the deposition with a solution of gold colloidal with C=32e11 and water rinsing and rinsing with physiological serum and abrasive friction; 121x magnification

in the drop. Thinking far ahead, it would appear that the return of this method compared to the resources used is low.

7.3.7 AFM measurement of an electrode with a deposited film of AuNPs

AFM measurements were also realized for electrodes with deposited nanoparticles. Gold nanoparticles can be observed in figure 7.27. AFM measurement for a longer scan shown in figure 7.30 reveals that the AuNPs deposited follow the initial micro-nanotexture of the graphite electrode. Due to the initial texture of the electrode, performing AFM measurements was challenging. Using a profilometer

to characterize the electrode surface might be a better alternative for future work, as the texture should be less problematic.

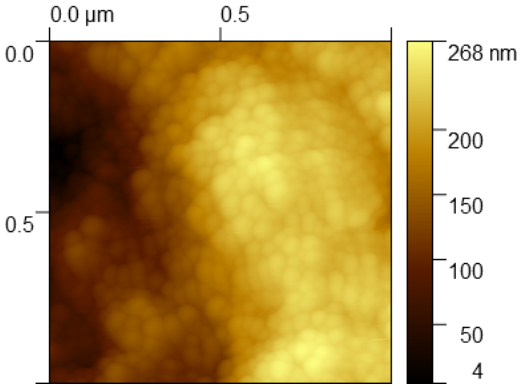

Figure 7.25: (a)

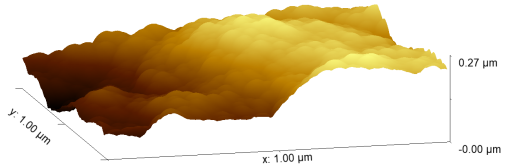

Figure 7.26: (b)

Figure 7.27: (a) 2D image taken with AFM, scan length is 1µm (b) 3D image of the AFM measure, the average roughness of a horizontal profile is $R_a = 1.565nm$

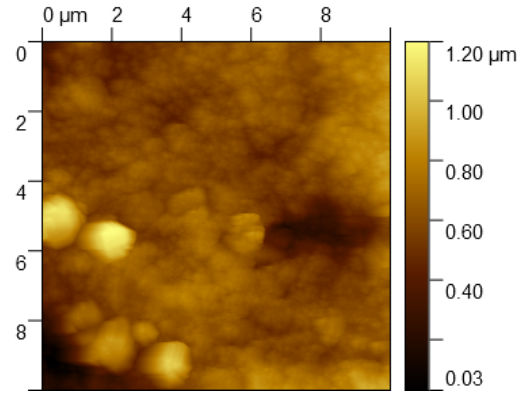

Figure 7.28: (a)

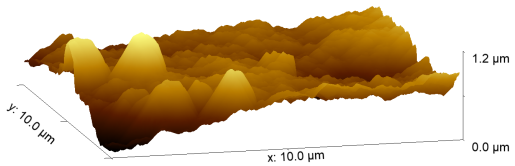

Figure 7.29: (b)

Figure 7.30: (a) 2D image taken with AFM, scan length is 10µm (b) 3D image of the AFM measure, the average roughness of a horizontal profile is $R_a = 8.695nm$

7.4 Conclusion of the deposition processes

The objective of this section was to study the deposition of AuNPs using a modified drop casting method. The deposition was successful, and it was possible to obtain good coverage of AuNPs on the graphite electrode with the deposition method when the concentration of the gold colloidal solution was increased. Ensuring good coverage of the graphite electrode is important for the sensor because it indicates that for future usage, antibodies can be immobilized onto a majority of the surface of the graphite electrode. However, the study of the reproducibility of the depositions shows a lack of control regarding the deposition process. Furthermore, a significant amount of AuNPs is wasted during the deposition process.

A key aspect not fully understood for both the electrophoretic deposition and drop casting methods is how the nanoparticles adhere to the electrode surface. The drying method is probably linked to the attachment of the AuNPs to the surface. In addition to the drying method, a dependency regarding the substrate material for the deposition of AuNPs exists, as mentioned in [8]. For future studies, it would be interesting to investigate the exact origin behind the attachment of the AuNPs on the electrode surface for both processes.

Finally, other electrode surface modification methods applicable to graphite ink electrode could be used in future work. The electrodeposition of AuNPs was explained in section 2.3.2. Compared to electrophoretic deposition, that method has already been used for the fabrication of several electrochemical biosensors [35, 11, 66]. Moreover, this method was also tested on electrodes made of graphite in [20].

Finally, in the next chapter, EIS measurements of electrodes with deposited AuNPs using the modified drop casting method are investigated.

Chapter 8

EIS measurements

8.1 Introduction

In this chapter, EIS measurements of the electrode modified with AuNPs via the modified drop casting method are presented. The objective is to get a better understanding of the impact of the AuNPs on the charge transfer resistance R_{ct} and the other elements of the equivalent randles circuit.

8.2 Material

The redox couple used for the EIS measurements is the $[Fe(CN)_6]^{3/4-}$ couple. A 5mM $[Fe(CN)_6]^{3/4-}$ solution was used for the EIS measurements. The solution was prepared by dissolving 2.5 mmol of potassium ferricyanide (potassium hexacyanoferrate(III)), $K_3[Fe(CN)_6]$, and 2.5 mmol of potassium ferrocyanide (potassium hexacyanoferrate(II) trihydrate), $K_4[Fe(CN)_6]$, in 500 ml of distilled water.

8.3 Method

EIS measurements were carried out in the presence of 5mM $[Fe(CN)_6]^{3/4-}$ in a frequency range from 0.01Hz to 100kHz at a DC potential of +0.2V. The Frequency Analyser (FRA) measurement tool of the Nova 2.0 software [46] was used to perform the EIS measurement. The DC potential, 0.2V, corresponds to what is usually used in the literature when the $[Fe(CN)_6]^{3/4-}$ redox couple is used with an Ag/AgCl reference [30]. A 120 µL drop of $[Fe(CN)_6]^{3/4-}$ solution was deposited on the PCB to do the measurement as represented in figure 8.1.

Figure 8.1: Experimental setup for the EIS measurements

The measurements were fitted to an equivalent Randles circuit using the tool *Fit and simulation* of the Nova software. The equivalent randles circuit is shown in figure 8.2. CPE was used instead of an ideal capacitor for the equivalent circuit. The roughness of the initial graphite electrode causes non-ideal behavior of the double-layer capacitance as explained in the section 2.2 related to electrochemical impedance spectroscopy in *Chapter 1*.

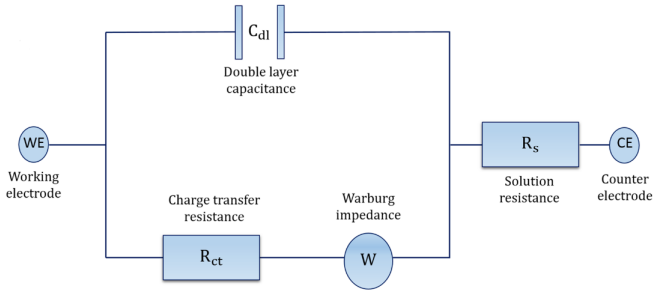

Figure 8.2: Equivalent Randles Circuit

8.4 Results and discussion

8.4.1 Determination of the equivalent circuit elements for various AuNPs-modified electrodes

EIS measurements were carried out for every electrode with deposited AuNPs via the modified drop casting method presented in subsection 7.3.2 except for electrode 6. The Nyquist diagram for electrode 1 is shown in figure 8.3. Since the Nyquist diagram before and after the deposition process are similar for all electrodes, the Nyquist plots of the other electrodes are not shown in this section but are in the appendices in Chapter A. The first observation that can be made when looking at the tables 8.1 and 8.2 is that there is a systematic diminution of R_{ct} when AuNPs are deposited. The table 8.3 shows the R_{ct} of the different electrodes before $R_{ct,before}$ and after $R_{ct,after}$ the deposition process. The table also includes the diminution percentage of R_{ct}, ΔR_{ct}, and the number of deposited AuNPs and

is sorted in ascending order of ΔR_{ct}. Since $R_{ct,before}$ of the different electrodes varies greatly, the diminution percentage $\Delta R_{ct} = 100 * \frac{R_{ct,before} - R_{ct,after}}{R_{ct,before}}$ was used to compare the electrodes. According to 8.3, ΔR_{ct} does not necessarily increase with the amount of nanoparticles deposited.

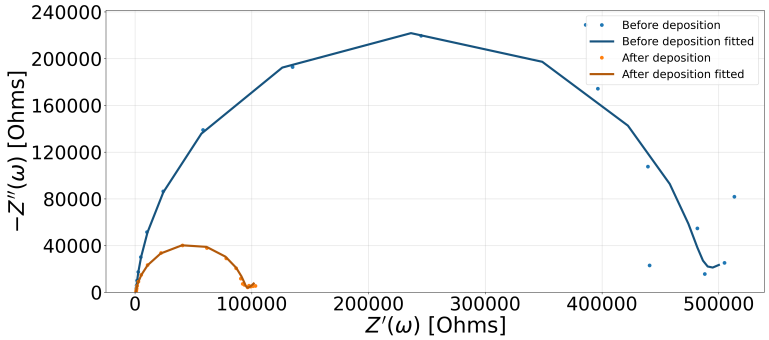

Figure 8.3: EIS measurements of the electrode 1 and the fitted curves of the data

Electrode	**Rs** [Ohm]	**Rct** [Ohm]	**W** (Y_0) [µOhm·s$^{(1/2)}$]	**CPE** (Y_0) [nOhm·s^N]	**N**
Electrode 1	774	480k	45.6	24.3	0.947
Electrode 2	677	219k	78.9	40.7	0.926
Electrode 3	748	193k	156	50.8	0.916
Electrode 4	691	152k	194	55.8	0.920
Electrode 5	667	61.8k	110	165	0.838
Electrode 7	712	330k	81.2	57.1	0.919
Electrode 8	716	146k	140	103	0.880
Electrode 9	743	77k	122	97	0.902
Electrode 10	677	103k	119	87.5	0.905
Electrode 11	679	90.8k	149	89.6	0.910
Electrode 12	756	185k	60.8	68.6	0.897

Table 8.1: EIS measurements before the deposition of AuNPs

The value of R_s for the different electrodes is on average 701 [Ohm]. Since R_s represents the resistance of the $[Fe(CN)_6]^{3/4-}$ solution, it was expected that this value should not change significantly between the different electrodes.

With the software used to fit the data, for each element of the circuit, an error percentage for the fitted value is given. This percentage indicates the impact of the element on the circuit model. The bigger the error percentage, the smaller the significance of the element for the circuit model. Removing an element from

Electrode	**Rs** [Ohm]	**Rct** [Ohm]	**W** (Y_0) [µOhm·s$^{(1/2)}$]	**CPE** (Y_0) [nOhm·s^N]	**N**
Electrode 1	734	93.6k	122	35.9	0.912
Electrode 2	678	53.2k	88.4	168	0.852
Electrode 3	791	40.8k	25.6	329	0.829
Electrode 4	729	60.5k	103	88.5	0.889
Electrode 5	672	23.9k	8.14	1.37	0.859
Electrode 7	528	147k	506	83.3	0.910
Electrode 8	686	56.2k	230	119	0.874
Electrode 9	745	52.2k	113	98.5	0.899
Electrode 10	696	85k	144	123	0.895
Electrode 11	655	70.7k	174	109	0.901
Electrode 12	669	107k	95	103	0.880

Table 8.2: EIS measurements after the deposition process

Electrode	$R_{ct,before}$ [Ohm]	$R_{ct,before}$ [Ohm]	ΔR_{ct} [%]	Number of deposited AuNPs deposited AuNPs
Electrode 10	103k	85k	17.4	2.10e8
Electrode 11	90.8k	70.7k	22.1	2.03e8
Electrode 9	77k	52.2k	32.2	3.37e8
Electrode 12	185k	107k	42.1	1.77e8
Electrode 7	330k	147k	55.4	1.74e8
Electrode 4	152k	60.5k	60.1	4.01e8
Electrode 5	61.8k	23.9k	61.3	3.88e8
Electrode 8	146k	56.2k	61.5	2.42e8
Electrode 2	219k	53.2k	75.7	2.86e8
Electrode 3	193k	40.8k	78.8	2.24e8
Electrode 1	480k	93.6k	80.5	1.67e8

Table 8.3: Variation of R_{ct} before and after EIS measurements

the circuit with a high error percentage does not significantly impact the values of the other elements. It was observed that before the deposition process, **W** often presented a high error percentage. For instance, for electrode 1, the error percentage before the deposition process was 92.65%. This suggests that a Warburg impedance was not necessary for the model of electrode 1. However, for other electrodes like electrode 9, a line can be observed at low frequencies in the Nyquist diagram in figure 8.4 suggesting that a Warburg impedance would be necessary for the fit although the error is 30.3%. After the deposition process, the error on **W** was 19%, but on the Nyquist diagram of electrode 1 in figure 8.3, a line at low

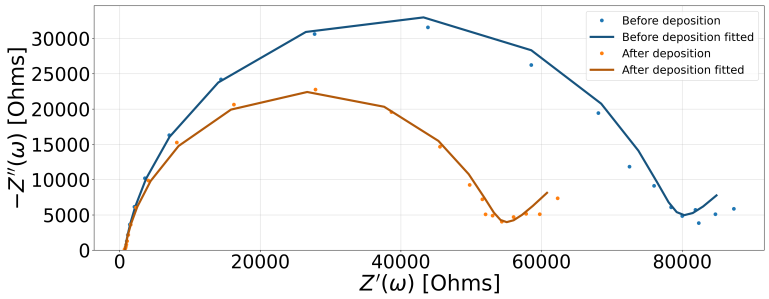

Figure 8.4: EIS measurements of the electrode 9 and the fitted curves of the data

frequencies is present, indicating that a Warburg impedance is necessary for the model. The large error for the Warburg impedance could be partly explained by insufficient measurement points being recorded during the EIS. Using more points per decade could help alleviate the errors on the fit.

After the deposition, the constant phase element (CPE) Y_0 increases and N decreases. In section 2.2 in *chapter 1*, it was mentioned that the use of CPE instead of a capacitor can be explained due to a non-ideal behavior of the double-capacitance layer. In the case of the graphite electrodes, they are initially rough, and adding nanoparticles impacts the roughness of the electrodes, and could lead to the modification of the double-layer capacitance

8.4.2 Variation of the number of AuNPs on the same electrode and impact on the equivalent circuit

In the previous section, various electrodes were compared together. To evaluate the impact of the increase of the number of deposited AuNPs on a single electrode, four successive depositions of AuNPs using the modified drop casting method were realized. Each deposition lasted 30 min. Due to time constraints, two experiments were conducted in parallel using the same method. One was used to analyze via SEM the amount of deposited AuNPs after the successive deposition, and one was used to do EIS measurements after the successive deposition.

SEM It is observed that the number of deposited AuNPs increases with the successive deposition process as shown in table 8.4 and in figures 8.5 - 8.8. The SEM images used for the characterization method are all in Chapter E in the appendices.

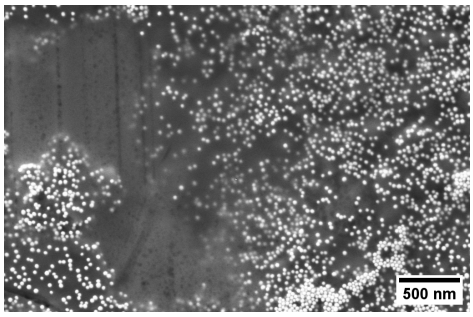

Figure 8.5: WE after the first 30 min deposition with C=8e11; 30kx magnification

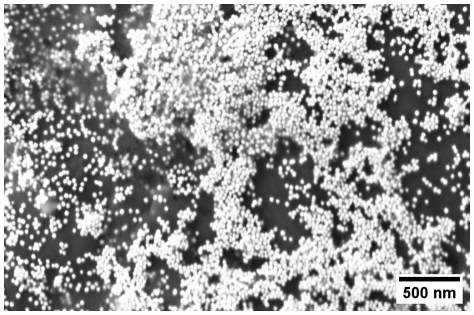

Figure 8.6: WE after the second 30 min deposition with C=8e11; 30kx magnification

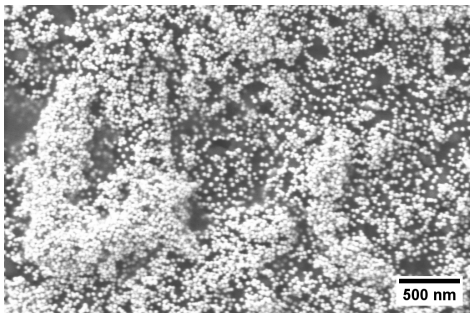

Figure 8.7: WE after after the third 30min deposition with C=8e11; 30kx magnification

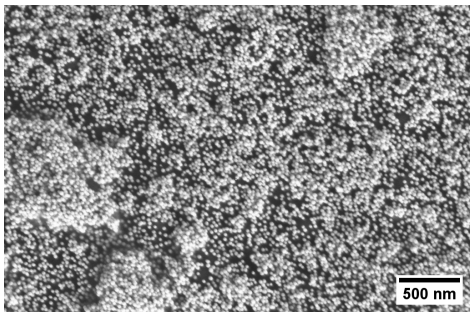

Figure 8.8: WE after the fourth 30 min deposition with C=8e11; 30kx magnification

	#AuNPs
before deposition	/
after the first deposition	2.021e8
after the second deposition	3.54e8
after the third deposition	4.50e8
After the fourth deposition	5.43e8

Table 8.4: Number of deposited nanoparticles after the successive deposition process

EIS The Nyquist diagram in figure 8.9 and table 8.5 show that, except after the second deposition, a decrease of the R_{ct} for the same electrode after the successive depositions. Since SEM images were not recorded for this experiment, nothing can be concluded for sure regarding the increase of R_{ct} after the second deposition process. After the successive deposition, the semicircle disappeared in the Nyquist plot, suggesting that R_{ct} is decreasing. After the fourth deposition, the Nyquist

plot presents no semi-circle, and R_{ct} is very low. The error percentage on R_{ct} was more than 100%. Therefore, R_{ct} is not necessary anymore for the model.

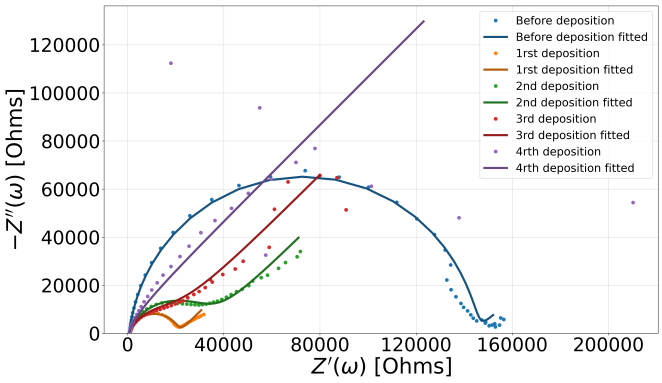

Figure 8.9: EIS measurements after each deposition process

	Rs [Ohm]	**Rct** [Ohm]	**W** (Y_0) [µOhm·s$^{(1/2)}$]	**CPE** (Y_0) [nOhm·s^N]	**N**
before deposition	750	144k	125	32.3	0.934
after the first deposition	769	20.4k	93.4	150	0.844
after the second deposition	771	33.2k	22.7	479	0.805
after the third deposition	725	20.2k	13.5	961	0.813
After the fourth deposition	721	28.3	6.89	353	1.04

Table 8.5: Values of the equivalents circuit elements

8.4.3 Problems of the EIS measurements

Several problems of the EIS measurements are presented in images 8.10 and 8.11.

- At low frequencies, the recorded measurement point starts to scatter as shown in figures 8.10. The Nyquist plot should represent the behavior of elements in the electrochemical cell via circuit elements that have a defined shape in Nyquist plots, and here, those points do not represent any elements and can impact negatively the fit.
- For some electrodes with a high density of AuNPs deposited, the impedance spectra do not ressemble the one of a Randles equivalent circuit as shown in figure 8.11.

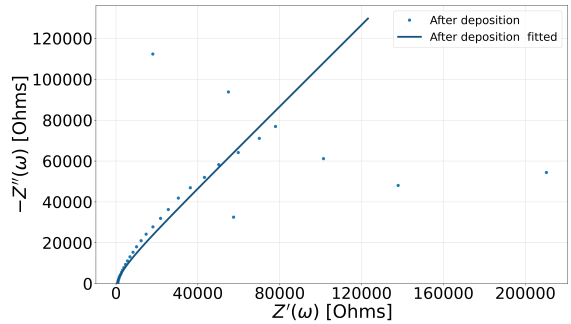

Figure 8.10: EIS measurements of the electrode in section 8.4.2 after the fourth deposition and fitted data curves. At low frequencies, the points start to scatter and do not represent real equivalent circuit elements anymore

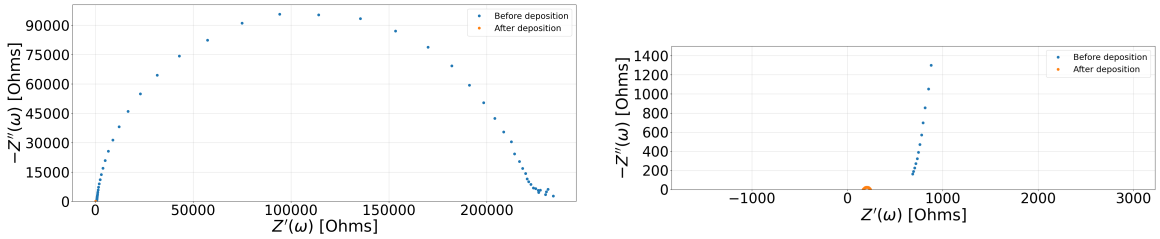

Figure 8.11: (left) EIS measurement for the deposition using a concentration of 32e11 nanoparticles during 2h; (right) zoom on the EIS measurements after the deposition process, the Nyquist diagram does not correspond to any equivalent circuit

Hypotheses were made regarding the origins of these problems:

- Hypothesis 1: There is a problem with the cables used to connect the potentiostat to the housing.
- Hypothesis 2: The housing itself is defectuous, or there is a problem with the contact of the housing with the PCB.
- Hypothesis 3: There is a problem with the $[Fe(CN)_6]^{3/4-}$ solution
- Hypothesis 4: There is a problem with the reference electrodes

Hypothesis 1: There is a problem with the cables used to connect the potentiostat to the housing

First, the potentiostat was used with a known circuit 8.13 using a Dummycell shown in figure 8.12.

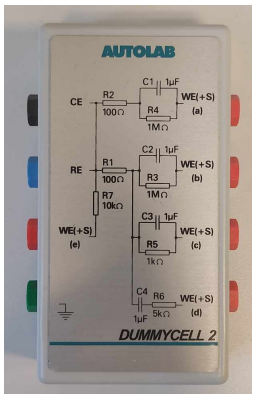

Figure 8.12: Dummycell

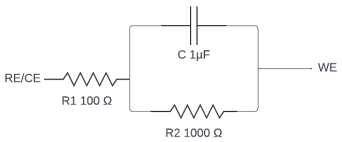

Figure 8.13: Circuit used

R1 [ohm]	R2 [ohm]	C [nF]
99.9	979	928

Table 8.6: Equivalent circuit of the Dummycell measured via EIS

The measurements in table 8.6 demonstrate that the problem does not lie with the connections from the potentiostat to the housing since there is almost no deviation of the measurements from the real values of the circuit.

Hypothesis 2: The housing itself is defective, or there is a problem with the contact of the housing

The measurements were conducted using the same circuit shown in figure 8.13. There are 8 WE per PCB, therefor the measurements were done for each contact to ensure that all the electronic contacts of the housing are working properly. Results in table 8.7 shows that the housing is not the problem since the measurements correspond to the known circuit for each contact (switch).

	R1 [ohm]	**R2 [ohm]**	**C [nF]**
switch1	99.9	997	982
switch2	99.9	997	971
switch3	99.9	997	965
switch4	100	998	976
switch5	100	998	961
switch6	99.9	998	960
switch7	99.9	997	968
switch8	99.9	997	963

Table 8.7: Values of the equivalent circuits

Hypothesis 3: The problem comes from the $[Fe(CN)_6]^{3/4-}$ solution

The concentration of the $[Fe(CN)_6]^{3/4-}$ might be too small. If the concentration is too small, too many ions could be consumed during the EIS measurement. Thus, the drop of $[Fe(CN)_6]^{3/4-}$ was changed between successive measurements. EIS measurements were realized four times for the same electrode, and the drop was changed between each measurement; the results are shown in figure 8.14. Four other measurements were done, but the drop was not changed during the repeated measurements. The results are shown in figure 8.15. The values of the equivalent circuit, when the drop is not changed between successive measurements, are similar to when the drop is changed. Therefore, the concentration of the $[Fe(CN)_6]^{3/4-}$ is not the problem.

Hypothesis 4: The problem comes from the reference electrodes

The references are made of Ag/AgCl ink. Those references are pseudo-references. The problem is the redox potential of a pseudo-reference might diverge from the standard redox potential of a true reference. In the section related to the electrochemical cell 2.2.3, in *Chapter 1*, it was mentioned that the standard potential of an Ag/AgCl reference was $E^\circ = +0.222V$. This potential is measured against

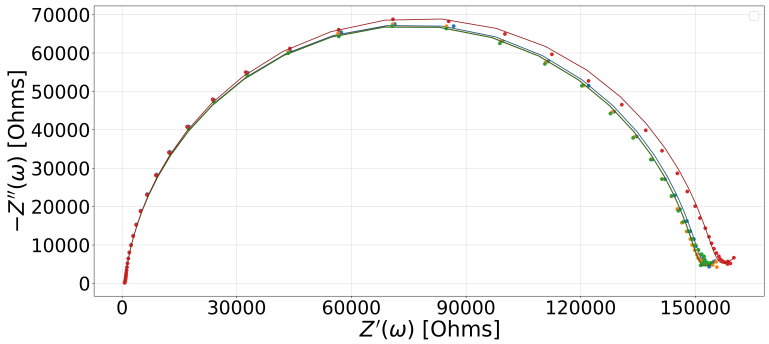

Figure 8.14: Nyquist plot of the EIS measurements when the drop of $[Fe(CN)_6]^{3/4-}$ solution is changed between the successive measure

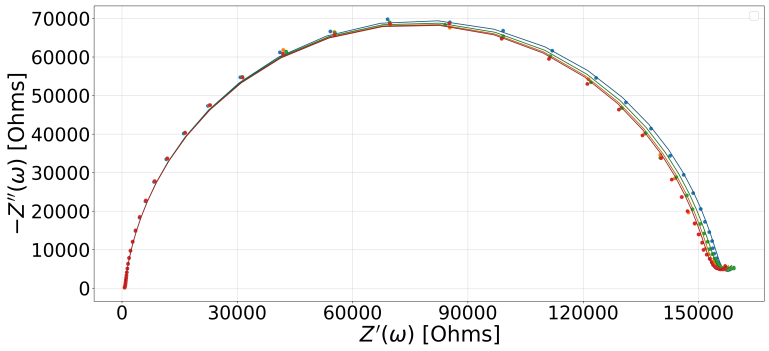

Figure 8.15: Nyquist plot of the EIS measurements when the drop of $[Fe(CN)_6]^{3/4-}$ solution is not changed between the successive EIS measurements

Rs [Ohm]	**Rct** [Ohm]	**W** (Y_0) [µOhm·s$^{(1/2)}$]	**CPE** (Y_0) [nOhm·s^N]	**N**
707	208	154k	43.7	0.933
708	173	152k	43.1	0.934
703	172	153k	43.2	0.933
699	178	152k	43.1	0.934

Table 8.8: Values of the equivalent circuit elements when the drop of $[Fe(CN)_6]^{3/4-}$ solution is not changed between the successive EIS measurements

a standard hydrogen electrode (SHE). By measuring the potential of the pseudo-reference made of Ag/AgCl ink against a true Ag/AgCl reference bought in the commerce and certified with $E^\circ = +0.222V$, we could find the redox potential of the Ag/AgCl pseudo reference. For the EIS measurements, a DC potential is superposed to an AC signal. In our experiments, the DC potential corresponds to

Rs [Ohm]	**Rct** [Ohm]	**W** (Y_0) [µOhm·s$^{(1/2)}$]	**CPE** (Y_0) [nOhm·s^N]	**N**
681	150k	181	42.7	0.931
684	149k	174	43.1	0.932
701	149k	189	43.3	0.931
705	154k	154	43.1	0.931

Table 8.9: Values of the equivalent circuit elements when the drop is changed in between successive measurements

the standard redox potential (E°) of the $[Fe(CN)_6]^{3/4-}$ couple. In the literature, the standard redox potential of the $[Fe(CN)_6]^{3/4-}$ couple is $E^\circ = +0.36$ [51]. If the potential of the pseudo-reference is known, we can more accurately find what potential should be applied at the working electrode with respect to the pseudo-reference made of Ag/AgCl ink to ensure that the DC potential corresponds to the redox potential of the $[Fe(CN)_6]^{3/4-}$ couple. In figure 8.16, the standard potential of the SHE, Ag/AgCl, and $[Fe(CN)_6]^{3/4-}$ couple are represented. It was not possible to test this solution in the scope of this thesis.

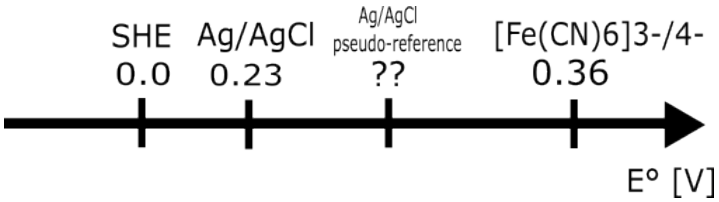

Figure 8.16: Representation of the standard potentials E° of the SHE, Ag/AgCl and $[Fe(CN)_6]^{3/4-}$

Variation of the charge-transfer resistance of the electrodes

The electrodes' R_{ct} on the same PCB varies greatly. In figure 8.17, the highest R_{ct} is 308kΩ and the lowest R_{ct} is 160kΩ. Two solutions are suggested for this problem:

- The variation of the shape of the graphite electrode. Since R_{ct} is prop to the active surface, if there is a defect in the electrode like a hole, this might explain a variation of R_{ct}
- The cleaning method used might not be effective enough. On top of the actual cleaning method used, electrochemical cleaning of the electrode using H_2SO_4 and cyclic voltammetry could be performed to reduce the variability of the R_{ct} of the graphite electrodes [20].

For futur studies, those two points should be investigated.

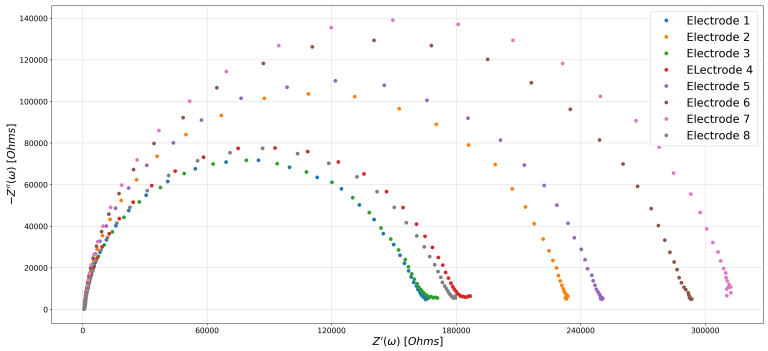

Figure 8.17: Variation of the R_{ct} for all the electrodes of the same PCB

8.5 Conclusion of the EIS measurements

From the measurements performed in this section, it was observed that after the deposition of AuNPs, there was a systematic diminution of the R_{ct}, and for some electrodes, ΔR_{ct} was high as 80%. For a deposition, there was no more characteristic semi-circle suggesting that R_{ct} is so low that the faradaic current in the electrochemical cell is due only to mass transfer.

The analysis of the other elements of the equivalent circuit showed that a Warburg impedance is not necessarily required before the deposition of AuNPs, but after the deposition, the Warburg impedance starts to appear. It was also observed that the value of the constant phase element Y_0 was increasing and N was decreasing after the deposition processes. It was supposed that this variation was related to the change in the surface structure of the electrode after the deposition.

Finally, some problems of the measurement were investigated. The most important problem was the scattering of the points at low frequency, which directly impacted the fitting and caused errors. It was first demonstrated that the problem did not come from the experimental setup. Actually, the setup used is robust even for measurements done at high frequencies (100kHz) and low frequencies (10mHz). The exact cause of the cited problems could not be found, but as suggested in the last section, finding the standard potential of the pseudo-reference might help get more stable EIS measurements. Furthermore, excluding defective electrodes and using electrochemical cleansing might help reducing the initial variability of the charge-tranfer resistance of the graphite electrodes.

Chapter 9

Conclusion

The main objective of this master's thesis was the modification of electrode with deposited gold nanoparticles to increase the sensitivity of an impedimetric immunosensor.

In the early stages of the thesis, various fabrication techniques were reviewed and are presented in the literature review. Using a surface modification method involving gold nanoparticles offers three advantages: a decrease in the charge-transfer resistance, the biocompatibility of the electrode surface, and AuNPs can be deposited on an electrode surface without the need for fabrication processes in cleanrooms. For these reasons, the electrophoretic deposition and drop casting of AuNPs were investigated.

First, in order to estimate the number of deposited AuNPs and compare the results of the deposition processes, a characterization method using SEM image analysis with the ImageJ software was developed.

Then, the electrophoretic deposition (EPD) of AuNPs on a graphite electrode was presented. From the preliminary results, it was concluded that the electrophoretic deposition process works when high voltages are used (27V), the deposition process was fast (10min), and a substantial amount of deposited AuNPs could be observed. However, due to water electrolysis, it was not possible to realize the electrophoretic deposition on graphite ink electrodes without damaging them. In order to find a threshold voltage that would allow the deposition process to occur while avoiding the degradation of the electrode, three depositions at 1V, 1.3V, 1.5V, and a control test were conducted for 30 min. The amount of deposited AuNPs for each electrode was 1.69e8, 1.58e8, 1.79e8, and 1.56e8 for the EPD at 1v, 1.3V, 1.5V, and the control experiment, respectively. From these results, it was observed that at low voltage, the EPD process has almost no influence on the deposition process since the amount of deposited AuNPs for the EPD deposition

was close to the amount of the control experiment. From these results, it was concluded that the EPD process is not adapted for graphite ink electrodes due to the water electrolysis that occurs at low voltages and constrains the voltage that can be applied.

Then, a modified version of the drop casting method was tested to deposit AuNPs. First, through an experimental procedure to assess what parameters influence the most the deposition process, it was observed that the concentration of the gold colloidal solution (C) has the biggest impact. Therefore, depositions using varying solution concentrations were performed. A good coverage of the electrode could be observed when the concentration was increased, especially for the experiment with C=32e8. However, cracks in the deposited film could be observed. Moreover, the methods presented some drawbacks: it was difficult to get reproducible results, which showed a lack of control over the deposition process. Furthermore, a substantial amount of AuNPs are wasted in the deposition process.

Finally, EIS measurements were performed, and it was observed that when AuNPs are deposited, there is a systematic decrease of the charge-transfer resistance. The biggest decrease in terms of charge-transfer resistance was %80 thanks to the deposited AuNPs. But, this decrease was not necessarly linked to the increasing number of AuNPs. For several measurements, at low frequencies, scattering of the data point could be observed on the Nyquist diagram. Solutions were investigated to find the origin of the problem, and it appears that the problem lies with the pseudo-reference electrodes.

9.1 Future work

The electrophoretic deposition process works and appears like an easy and relatively fast method to deposit nanoparticles on an electrode. Uniform deposition of AuNPs can be achieved as reported in [8]. For this reason, it would be interesting for future work to use this method with electrodes made of a different material, such as silicon wafer or carbon plate electrode, to avoid water electrolysis problems.

In this thesis, the sensor sensitivity was increased by reducing the charge transfer resistance of the electrode via the deposition of AuNPs. In the literature, among the properties of AuNPs, their large surface-to-volume ratio that leads to an increased active surface of the electrode is often cited as a reason for the decrease of the charge-transfer resistance [54]. However, quantitative measurement of the increase of the active surface is not always explicitly presented. It would be interesting for future work to study what is the exact impact of the active surface of the electrode

on the charge-transfer resistance. This would lead to a better comprehension of the influence of AuNPs on the electron transfer at the interface electrode/electrolyte.

Finally, other surface modification methods exist, like the electrodeposition of AuNPs. It appears to be a good alternative to the electrophoretic deposition process for graphite ink electrodes since the voltage used can be under the voltage at which water electrolysis occurs.

Appendix A

Nyquist plot of the experiment regarding the influence of the parameters of the modified drop casting method

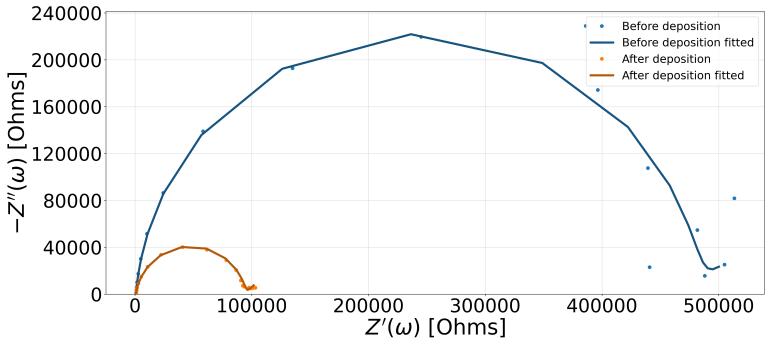

Figure A.1: EIS measurements of the electrode 21 and the fitted curves of the data

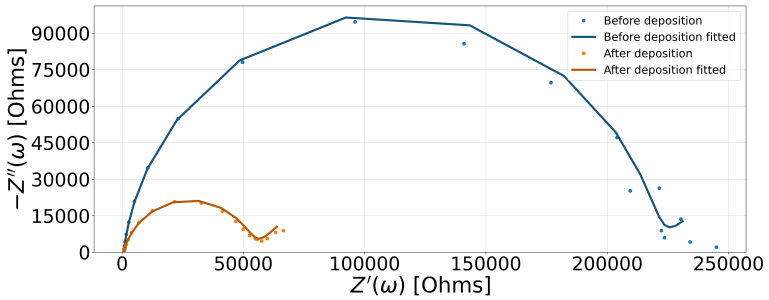

Figure A.2: EIS measurements of the electrode 2 and the fitted curves of the data

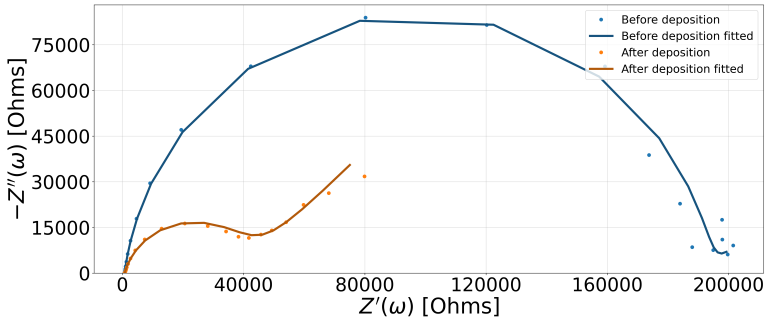

Figure A.3: EIS measurements of the electrode 3 and the fitted curves of the data

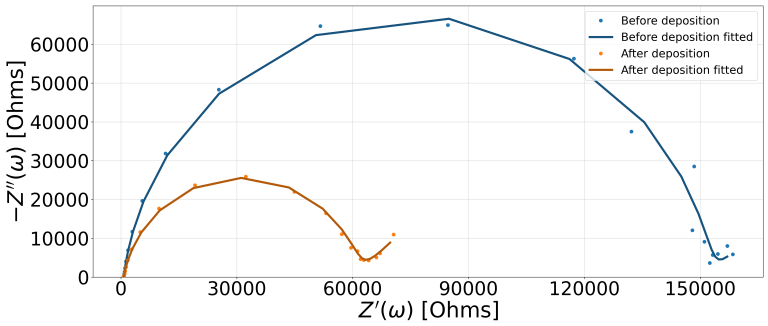

Figure A.4: EIS measurements of the electrode 4 and the fitted curves of the data

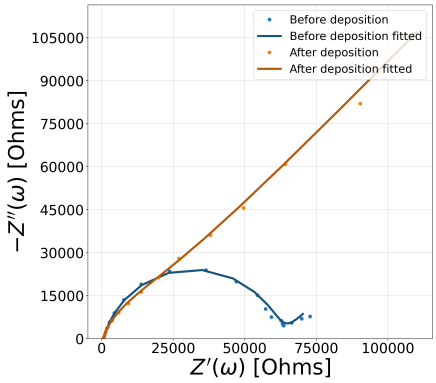

Figure A.5: EIS measurements of the electrode 5 and the fitted curves of the data

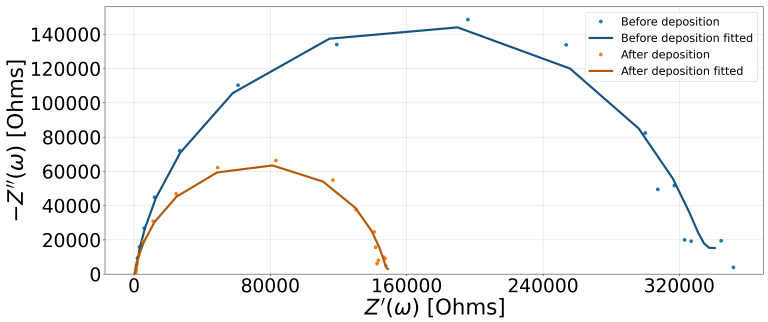

Figure A.6: EIS measurements of the electrode 7 and the fitted curves of the data

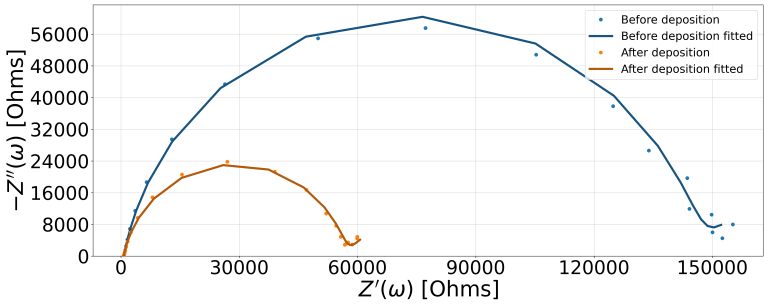

Figure A.7: EIS measurements of the electrode 8 and the fitted curves of the data

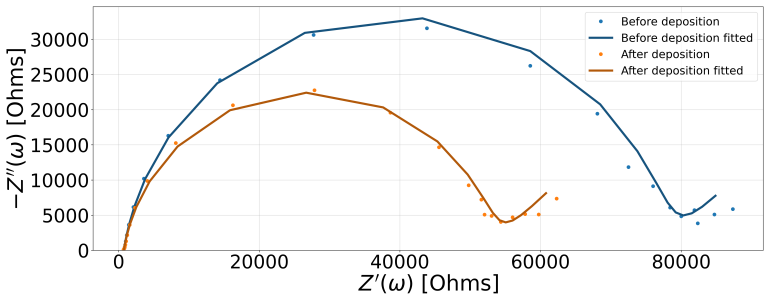

Figure A.8: EIS measurements of the electrode 9 and the fitted curves of the data

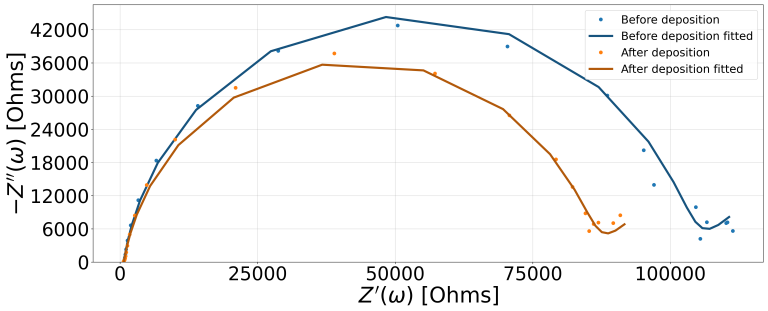

Figure A.9: EIS measurements of the electrode 10 and the fitted curves of the data

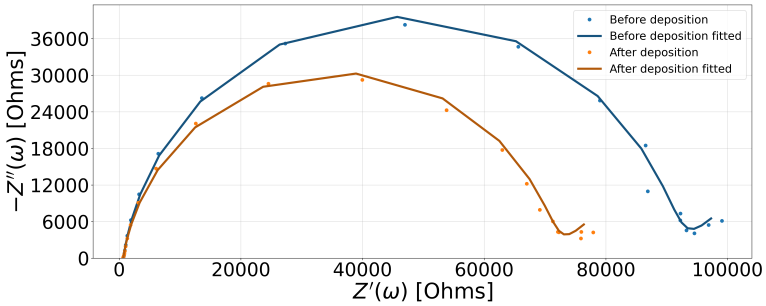

Figure A.10: EIS measurements of the electrode 11 and the fitted curves of the data

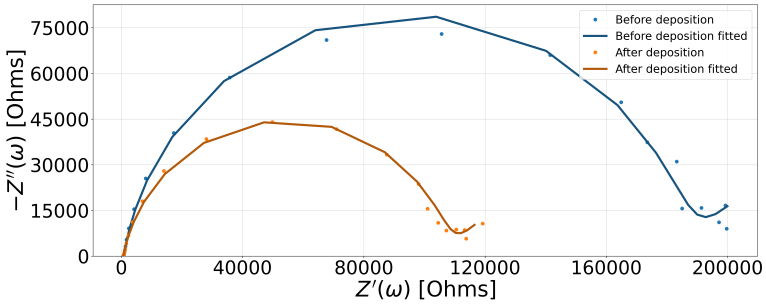

Figure A.11: EIS measurements of the electrode 12 and the fitted curves of the data

Appendix B

SEM images of the treshold voltage experiment

10 SEM Images of control experiment

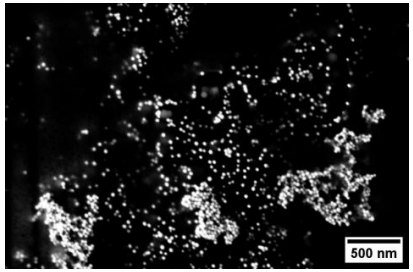

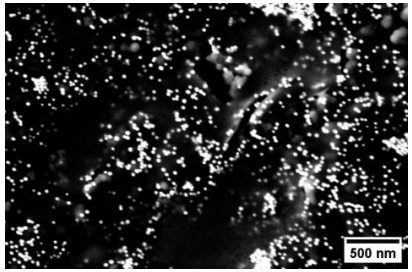

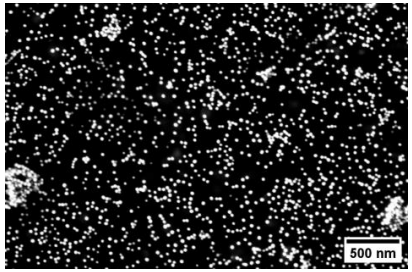

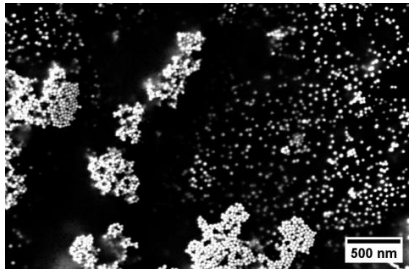

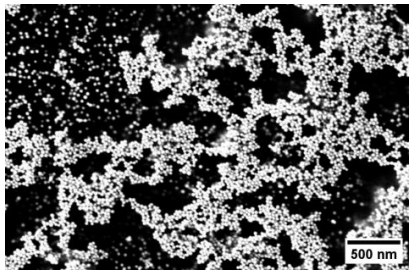

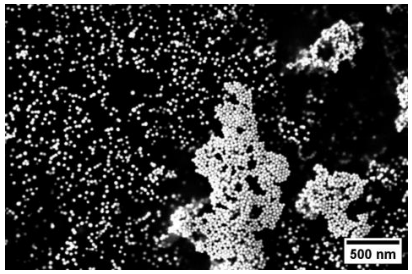

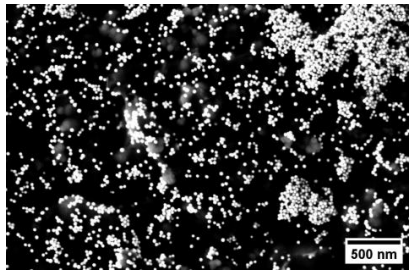

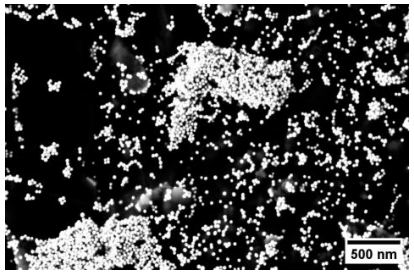

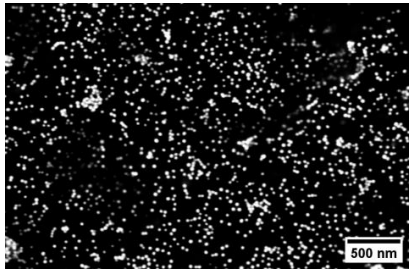

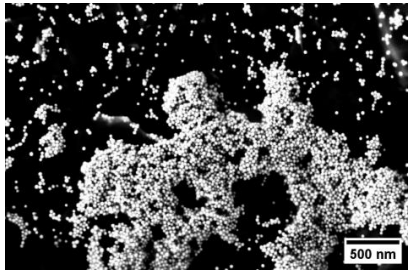

10 SEM Images of 1V EPD

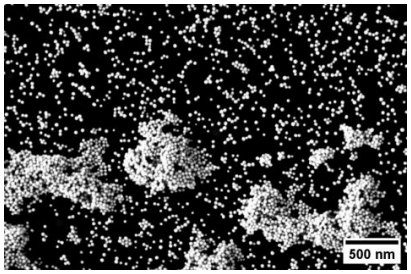

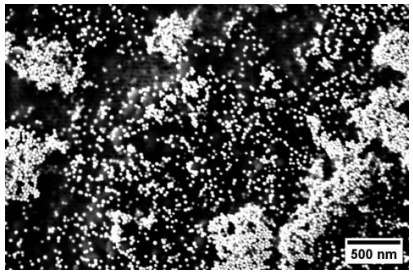

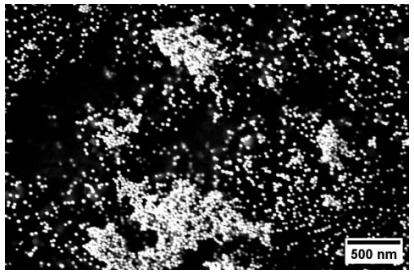

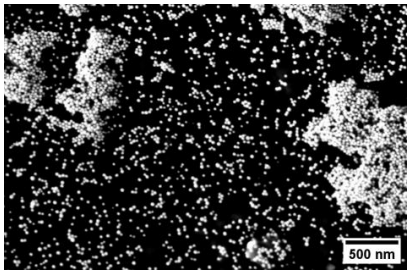

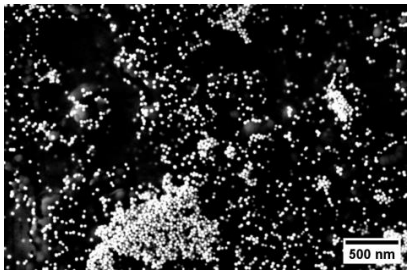

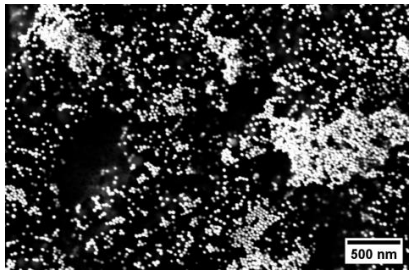

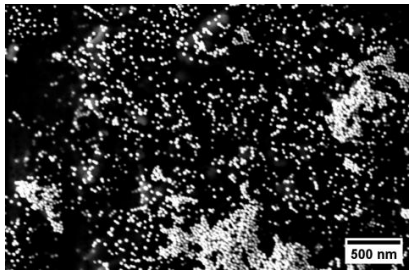

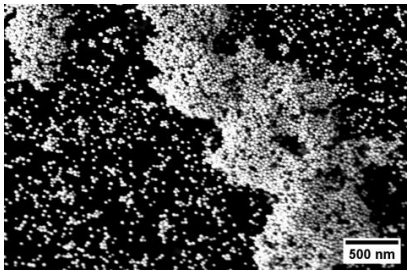

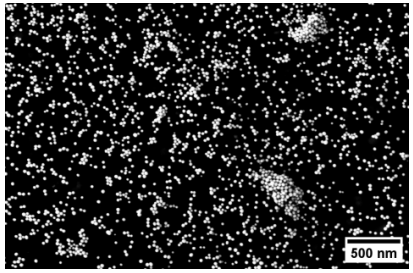

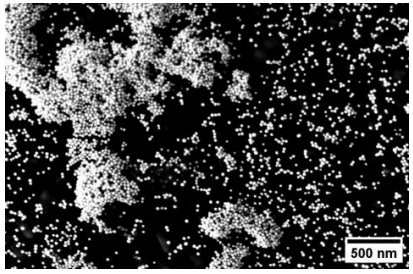

10 SEM Images of control 1.3V EPD

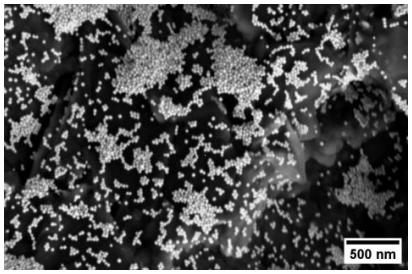

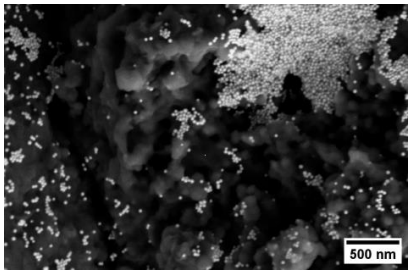

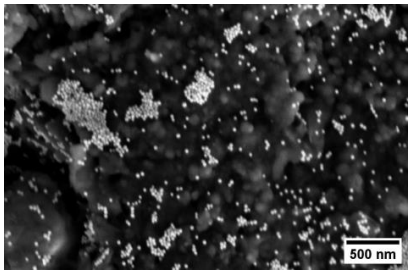

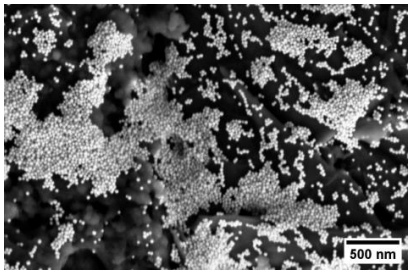

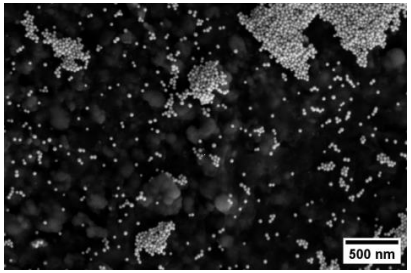

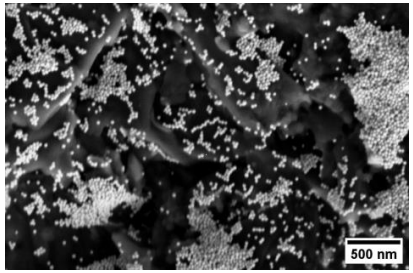

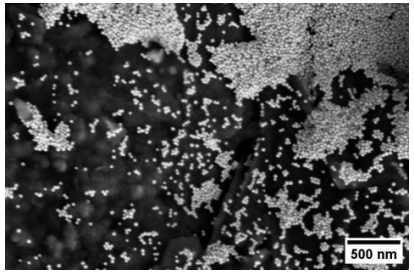

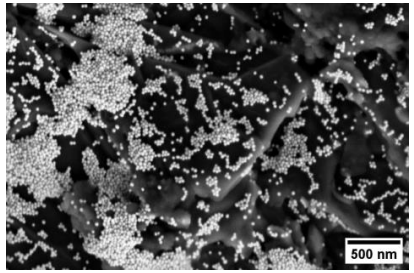

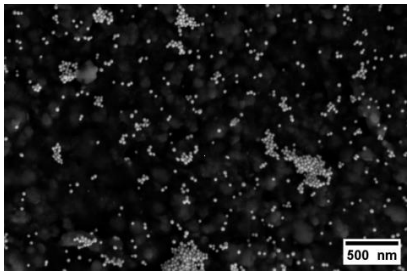

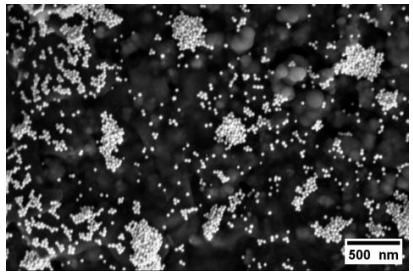

10 SEM Images of 1.5V EPD

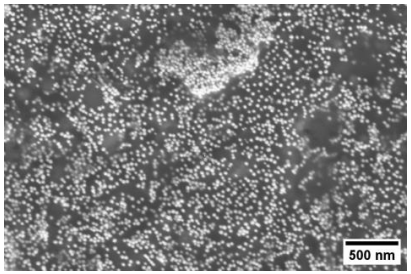

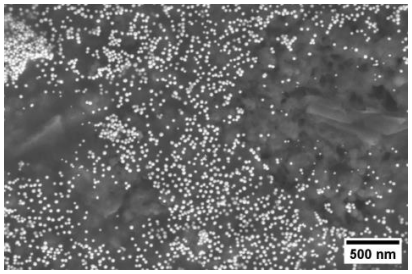

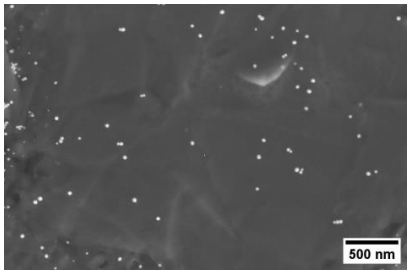

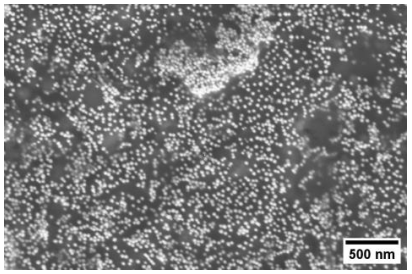

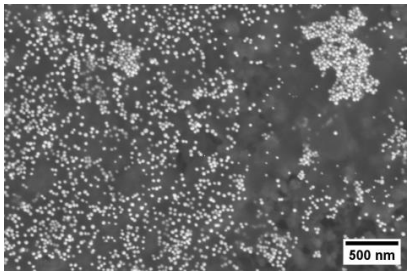

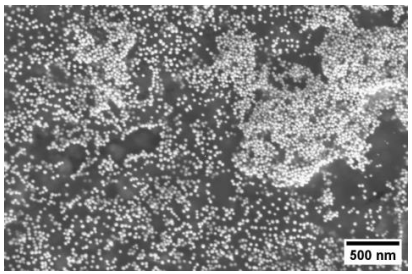

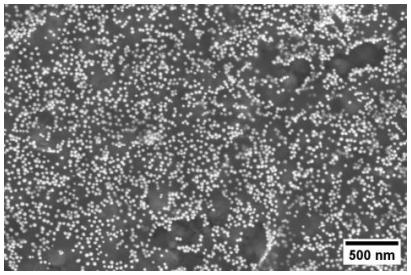

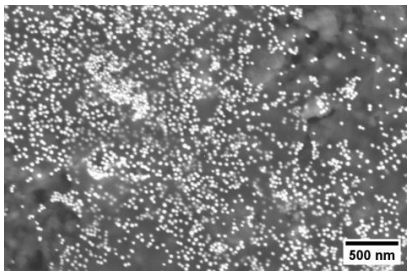

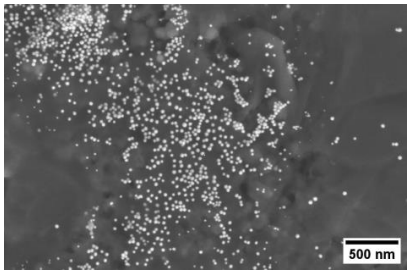

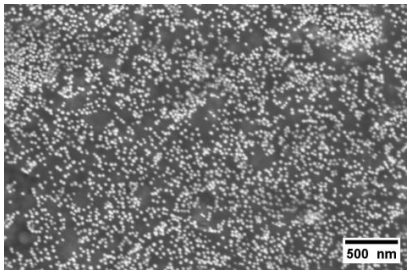

Appendix C

SEM images of the experiment regarding the influence of the parameters of the modified drop casting method

10 SEM Images of electrode 1

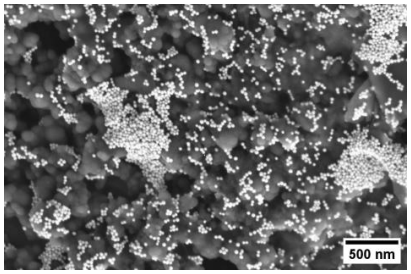

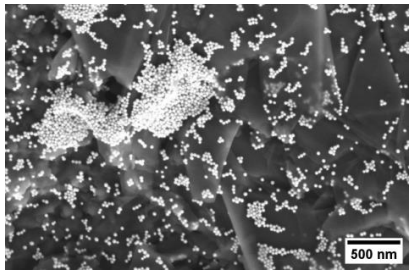

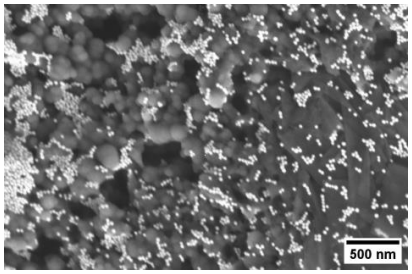

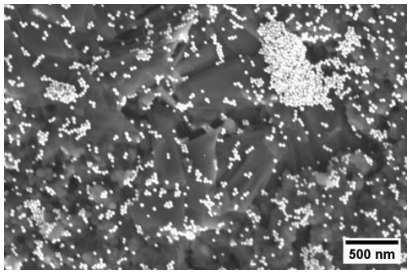

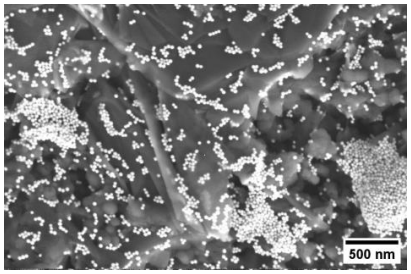

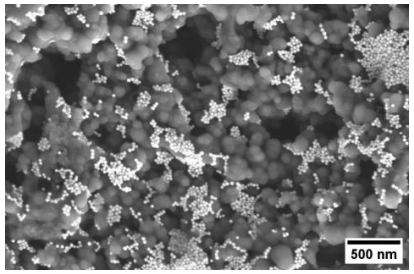

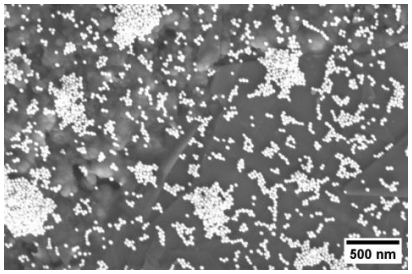

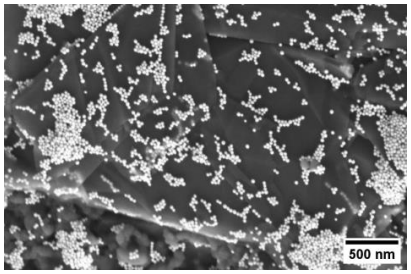

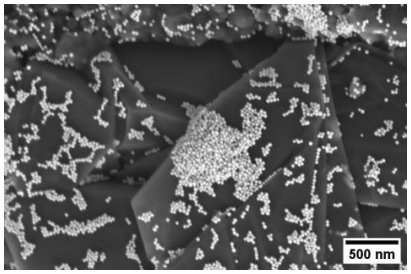

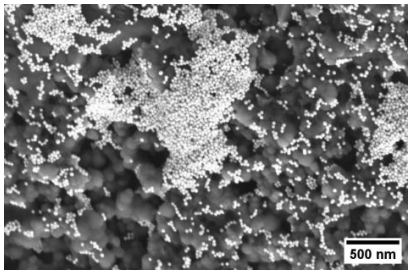

10 SEM Images of electrode 2

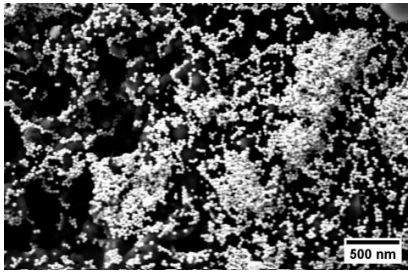

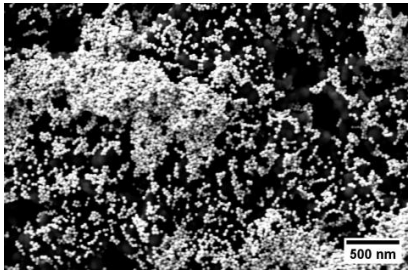

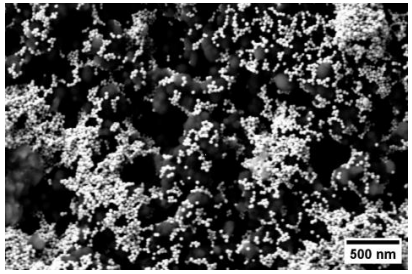

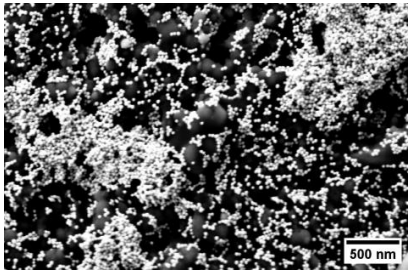

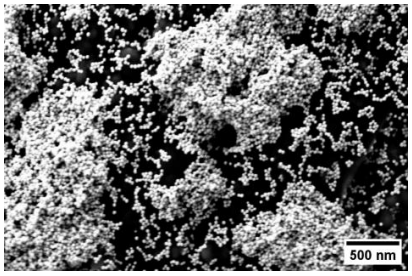

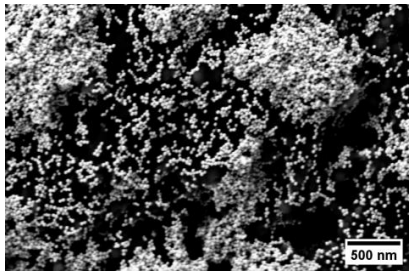

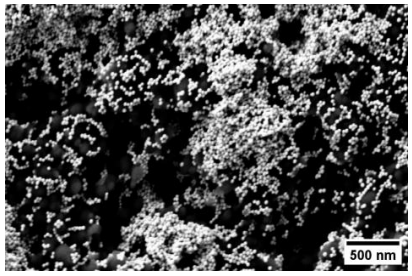

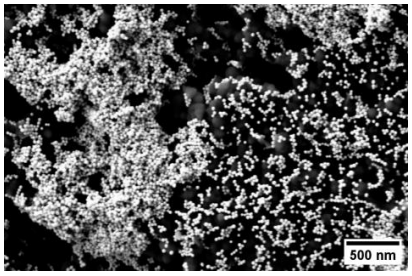

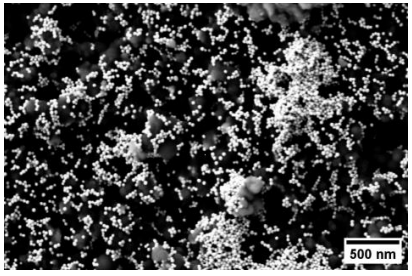

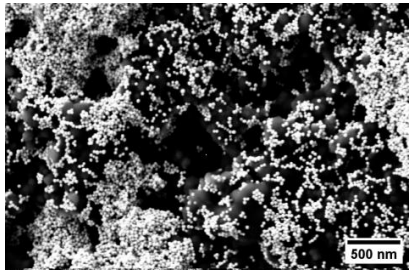

10 SEM Images of electrode 3

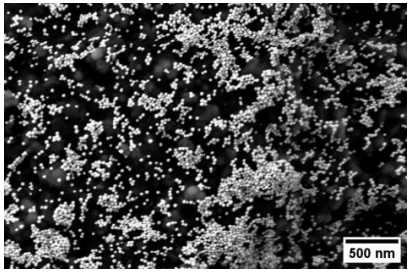

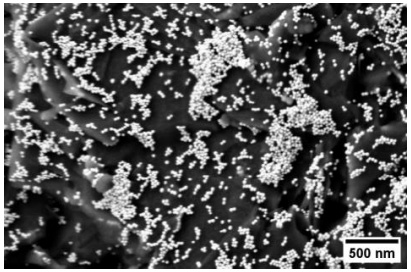

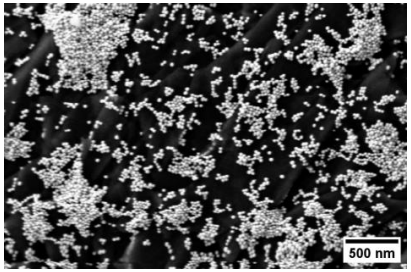

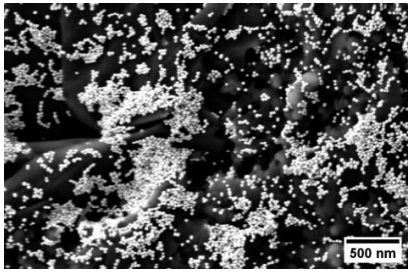

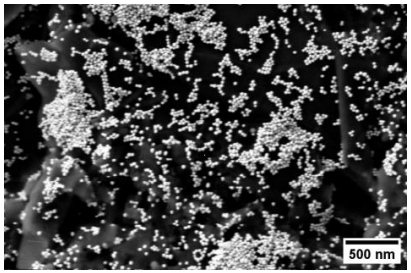

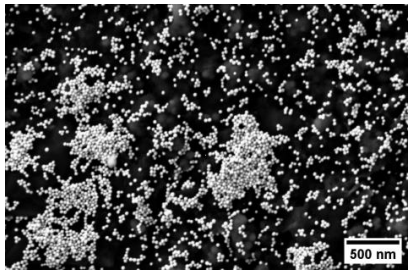

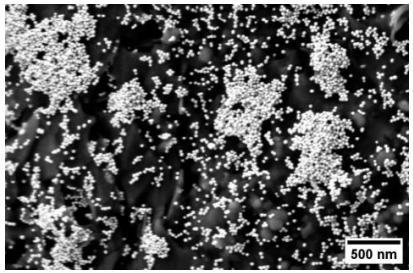

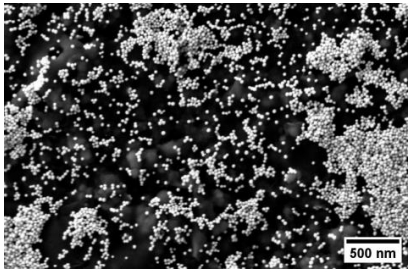

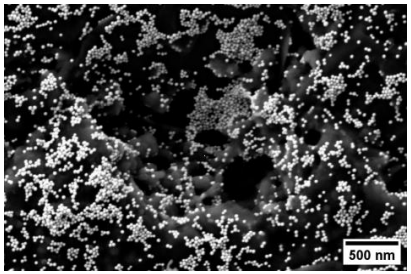

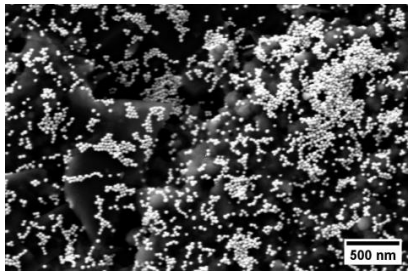

10 SEM Images of electrode 4

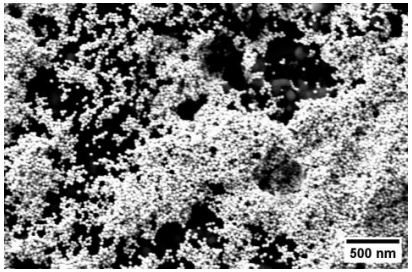

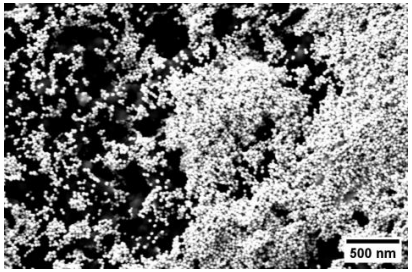

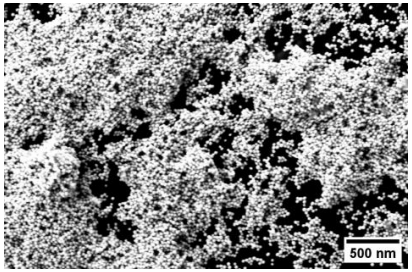

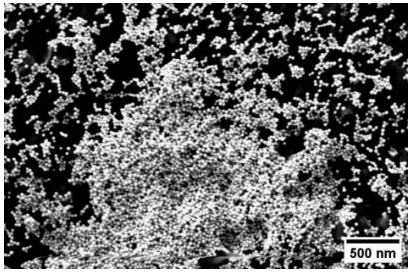

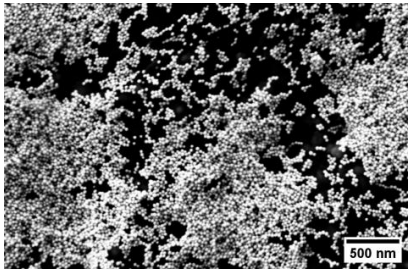

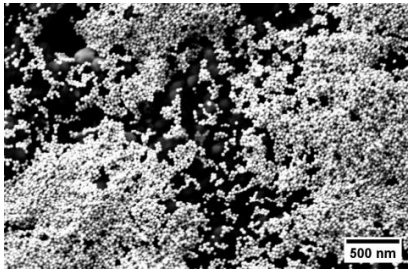

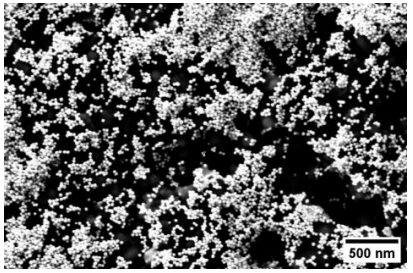

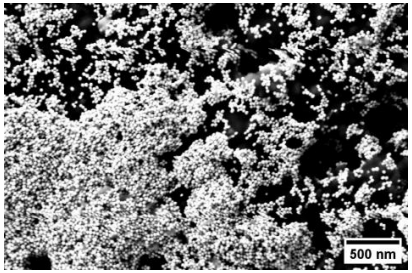

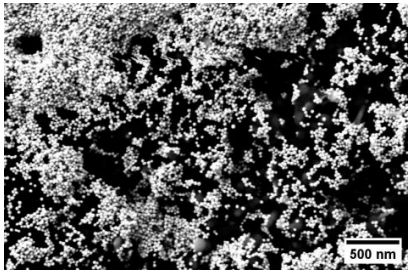

10 SEM Images of electrode 5

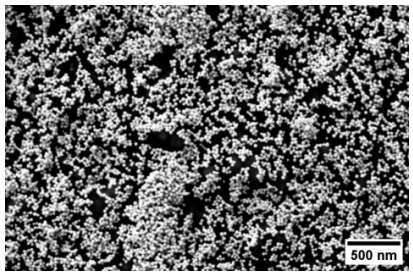

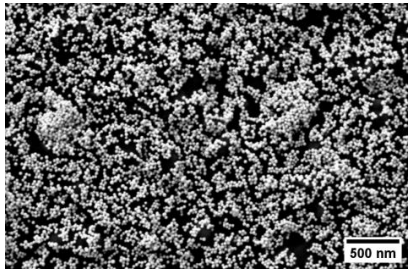

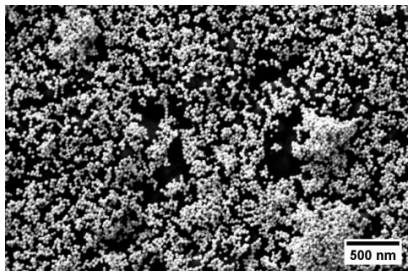

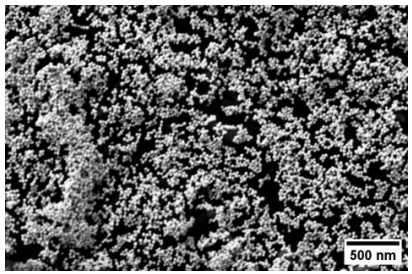

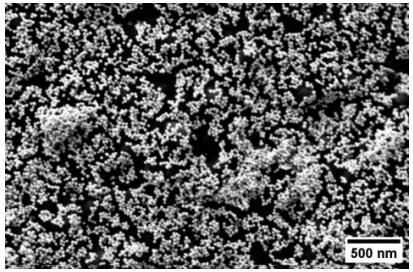

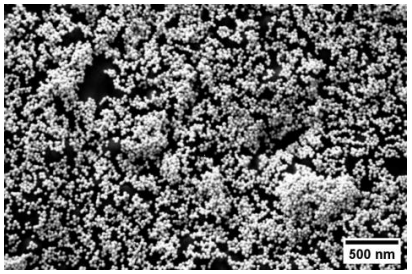

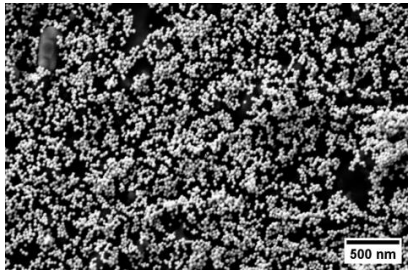

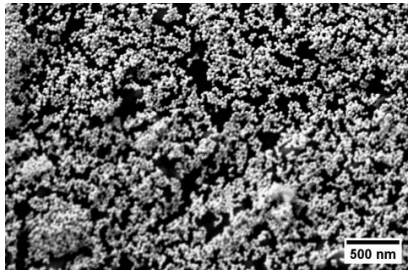

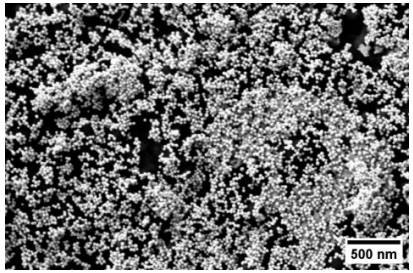

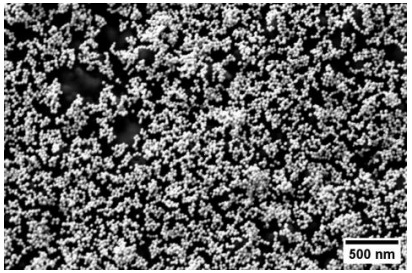

10 SEM Images of electrode 6

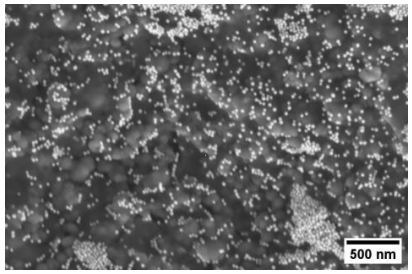

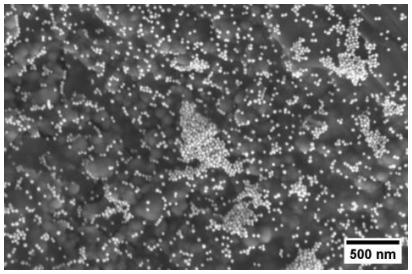

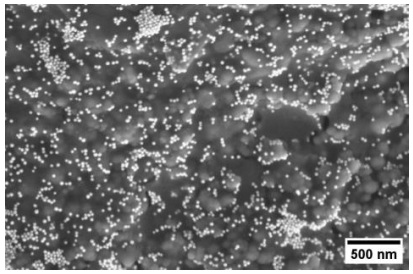

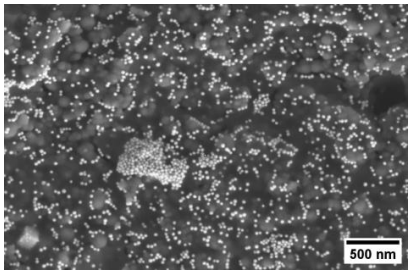

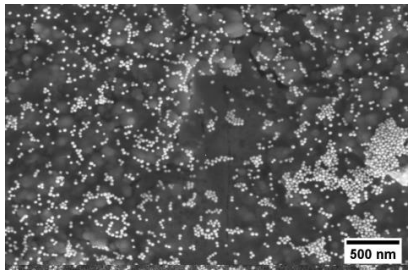

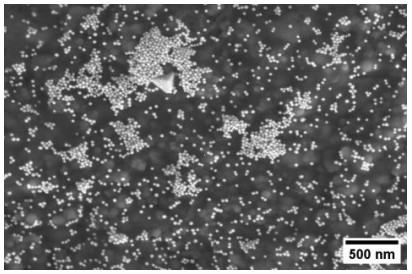

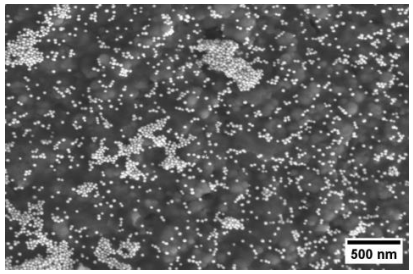

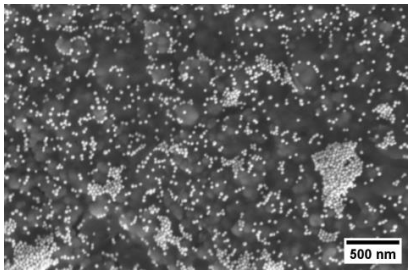

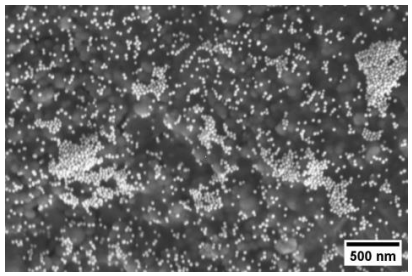

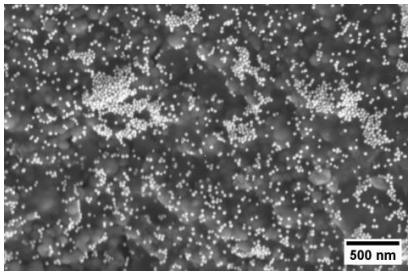

10 SEM Images of electrode 7

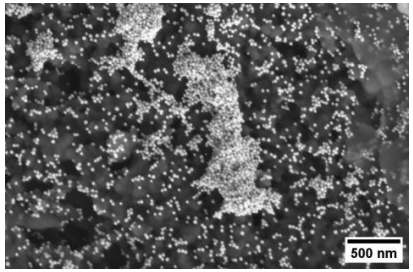

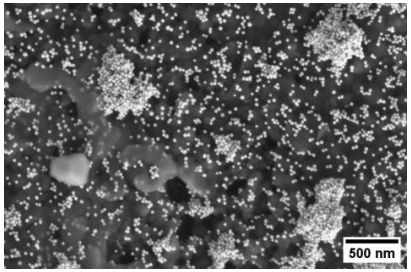

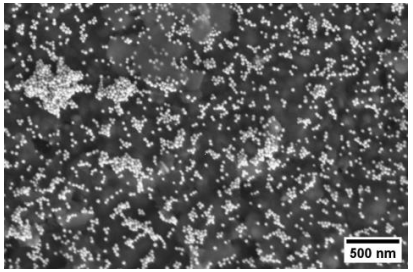

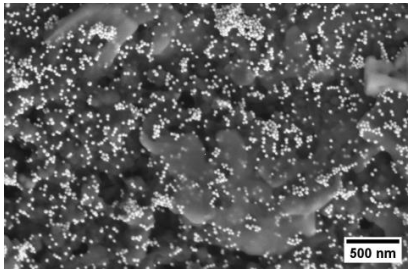

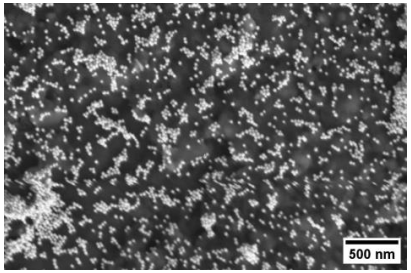

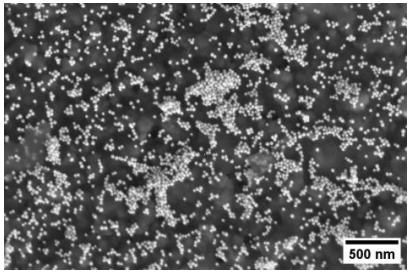

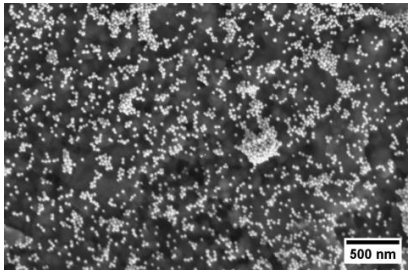

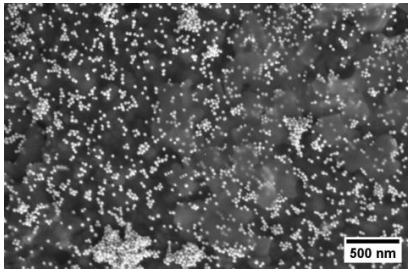

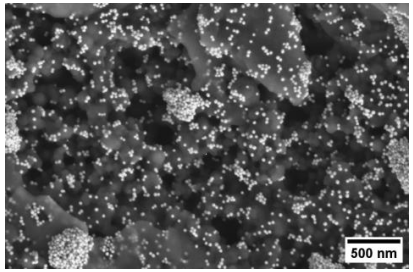

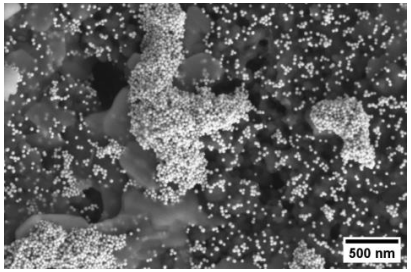

10 SEM Images of electrode 8

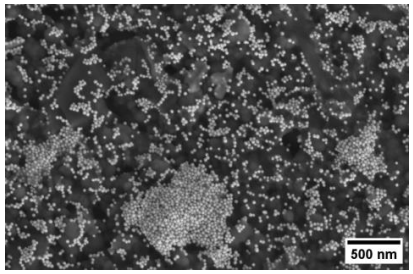

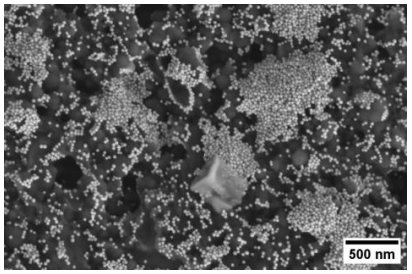

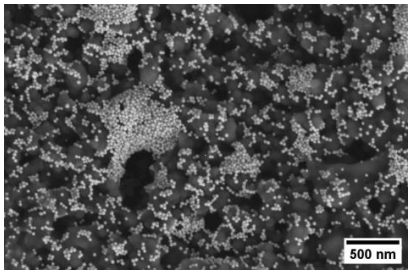

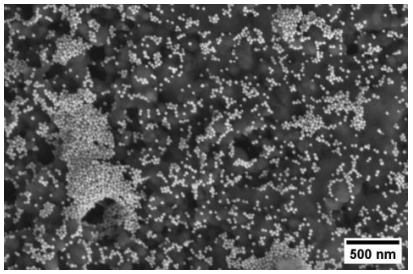

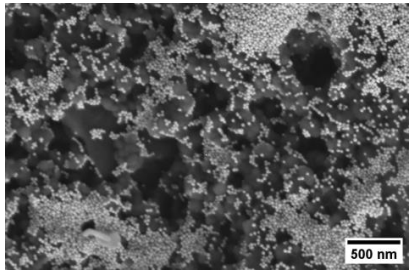

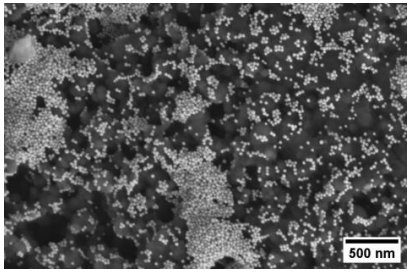

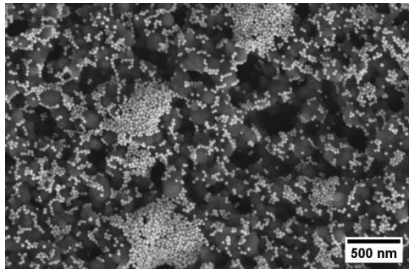

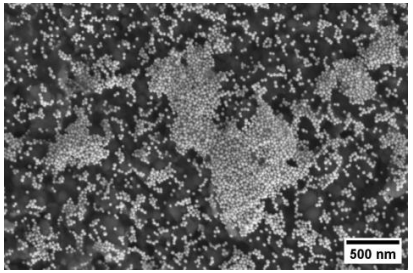

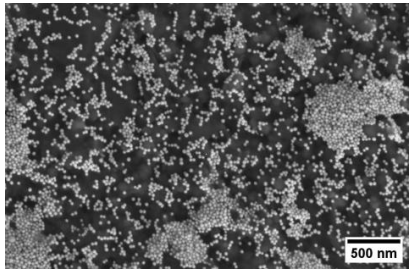

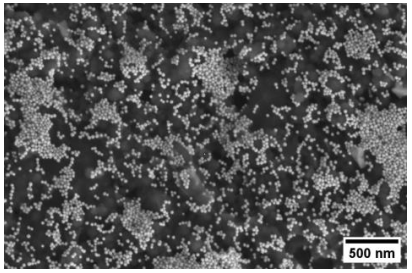

10 SEM Images of electrode 9

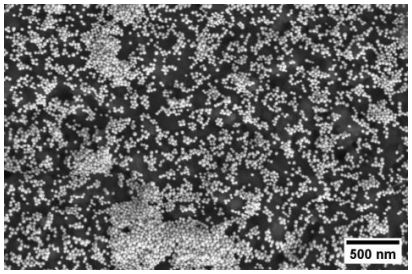

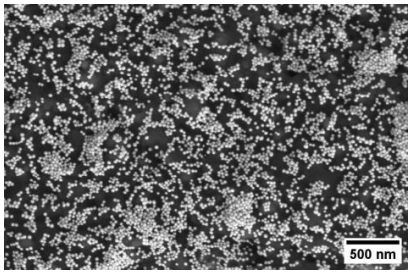

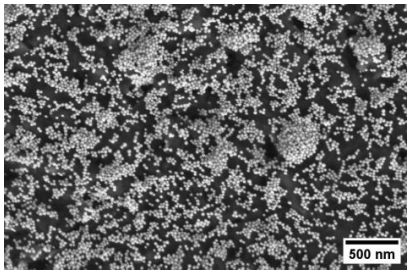

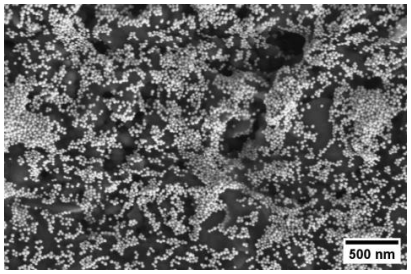

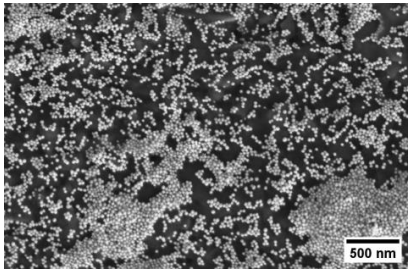

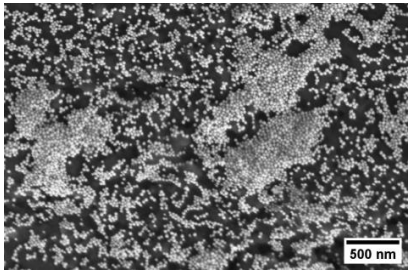

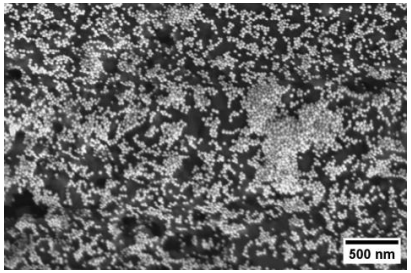

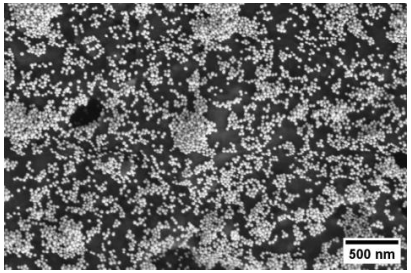

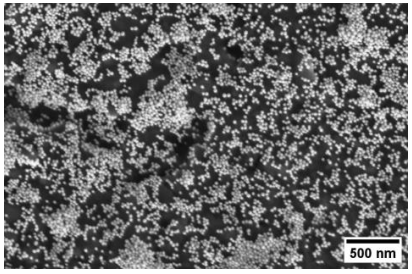

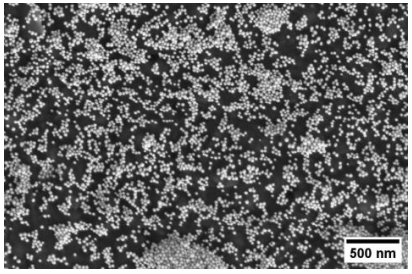

10 SEM Images of electrode 10

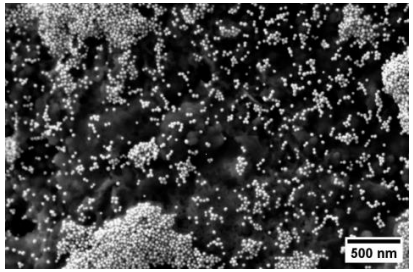

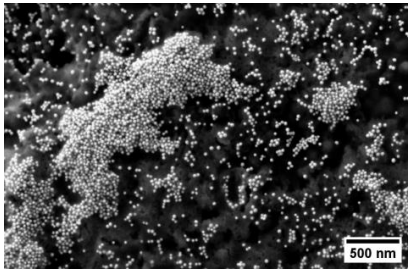

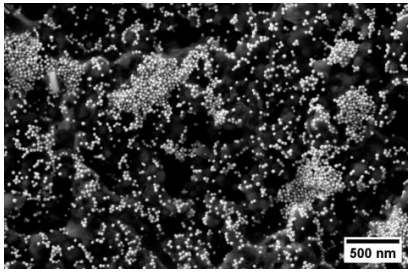

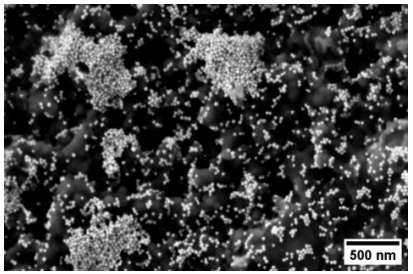

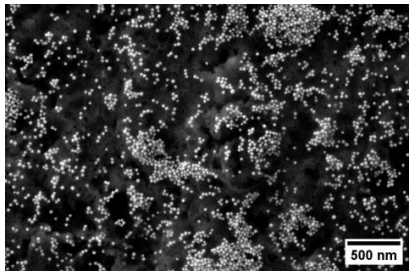

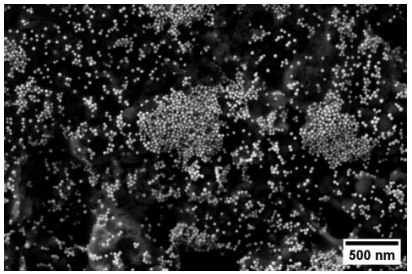

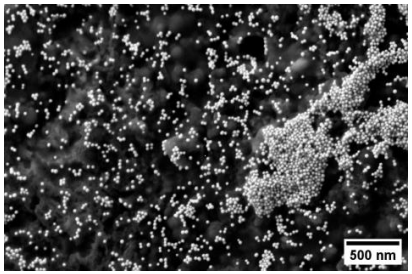

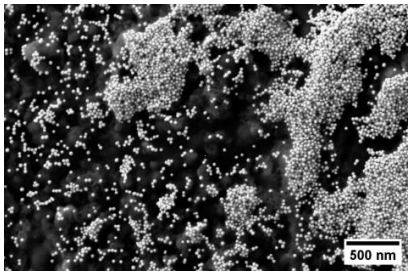

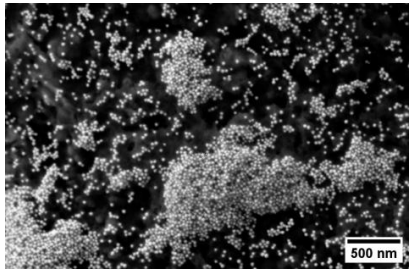

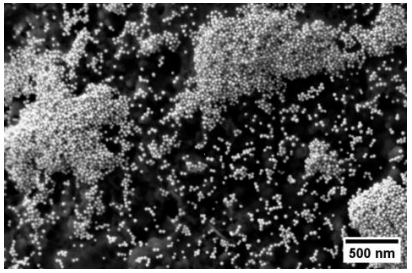

10 SEM Images of electrode 11

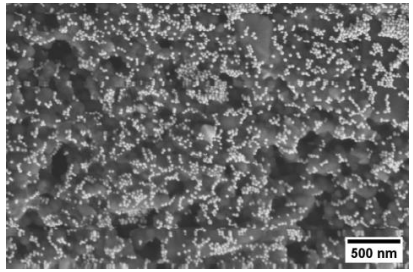

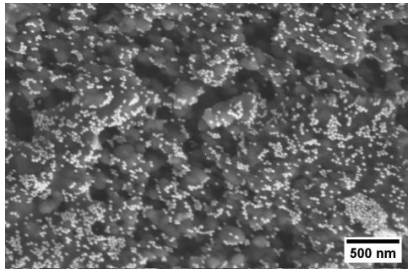

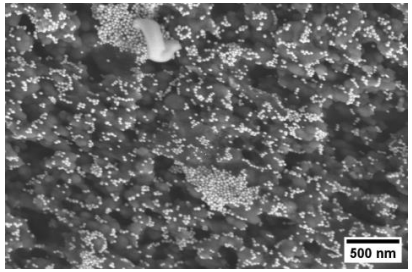

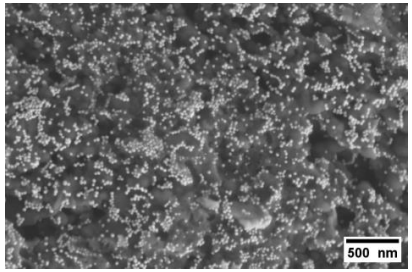

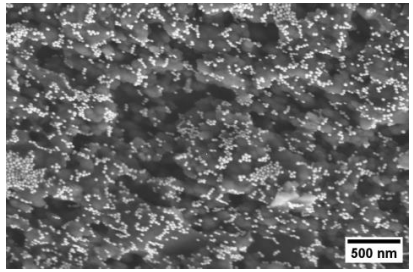

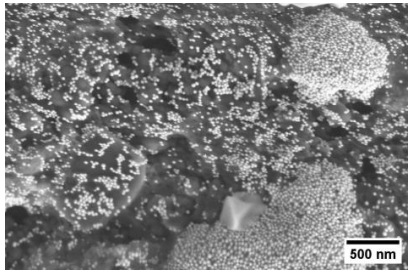

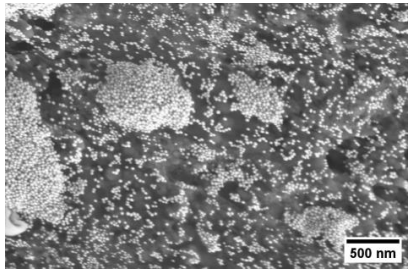

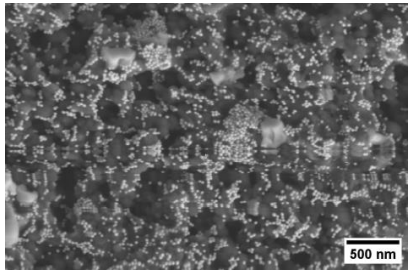

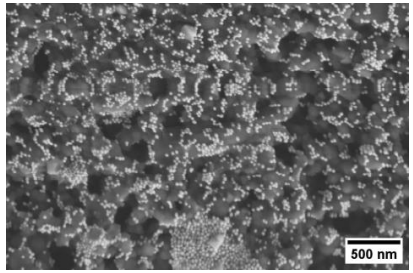

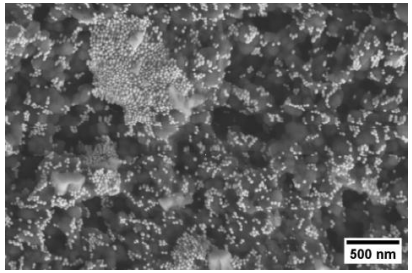

10 SEM Images of electrode
12

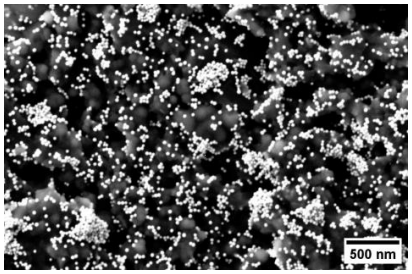

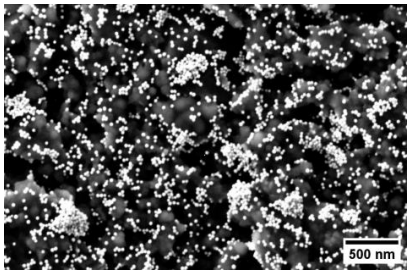

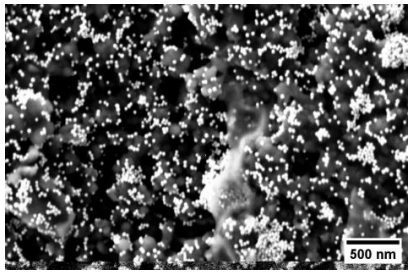

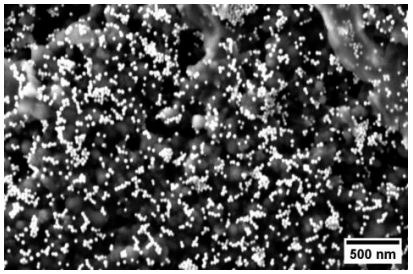

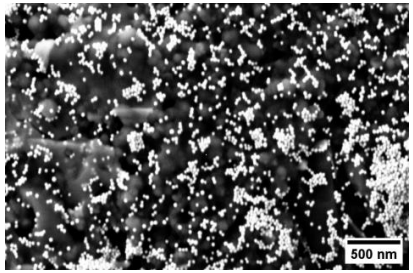

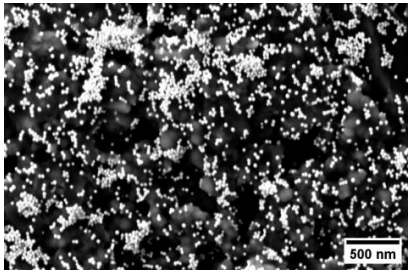

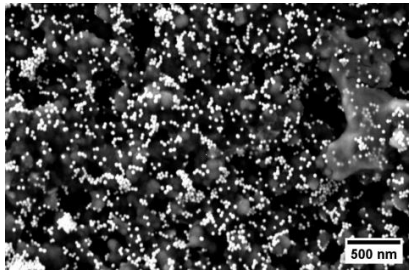

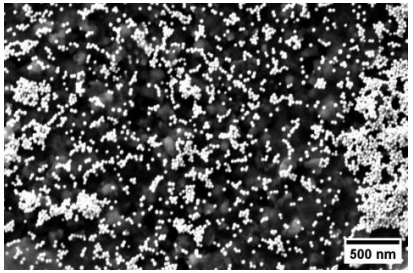

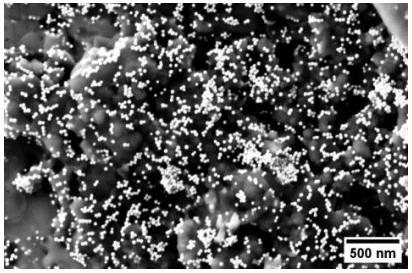

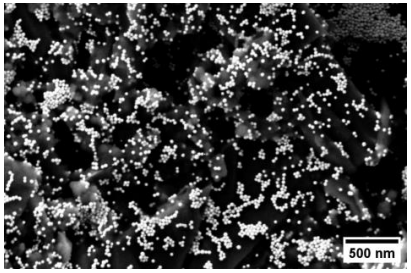

Appendix D

SEM images of the experiment where the concentration was varying for the modified drop casting method

10 SEM Images for the deposition with C=24e11

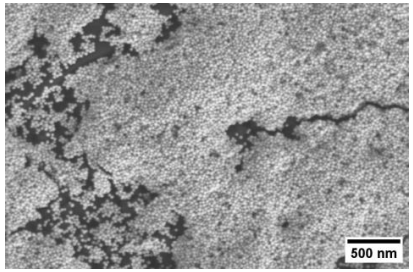

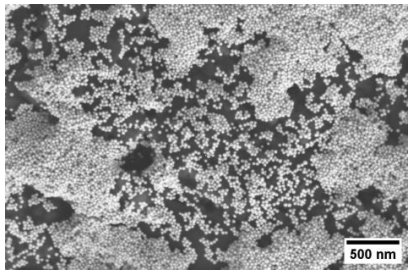

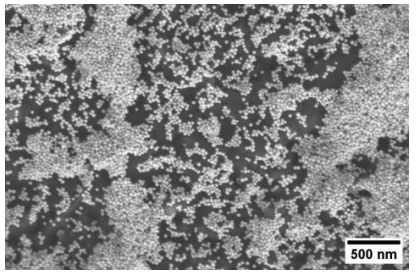

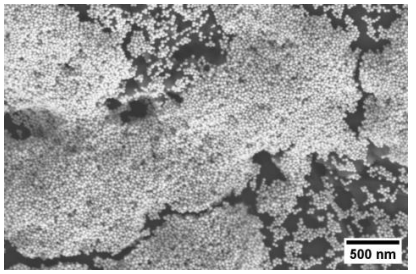

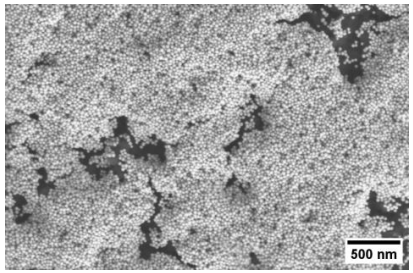

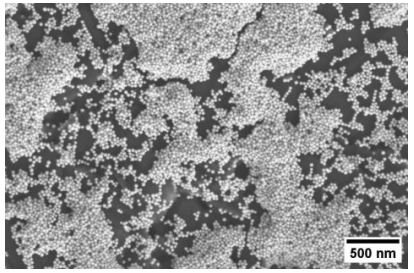

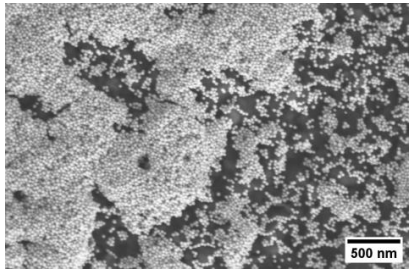

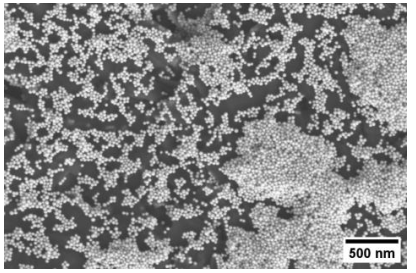

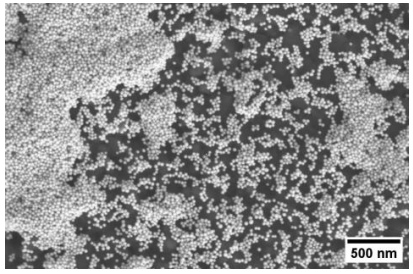

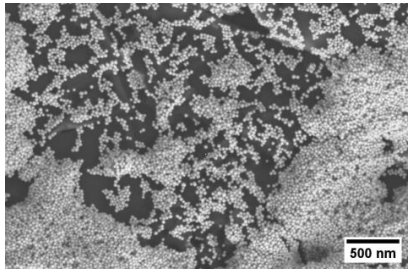

10 SEM Images for the deposition with C=32e11

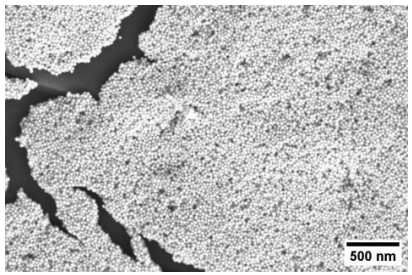

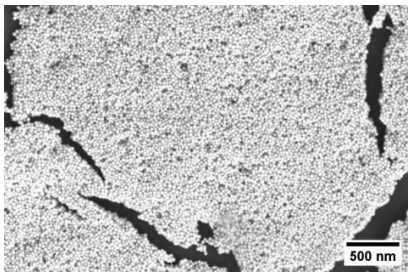

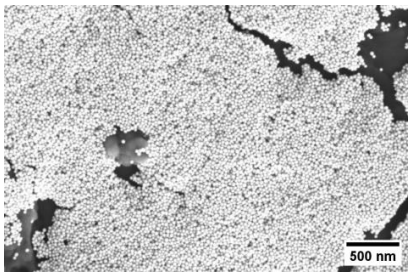

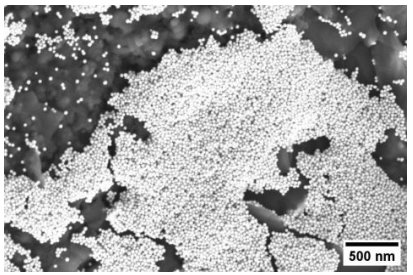

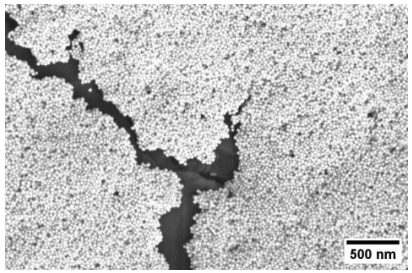

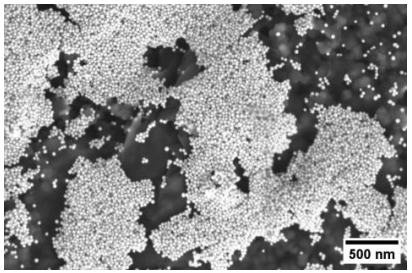

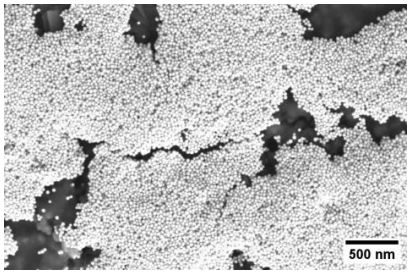

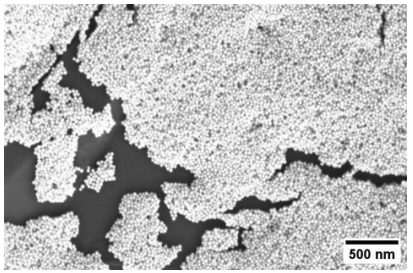

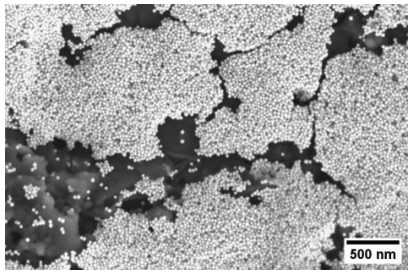

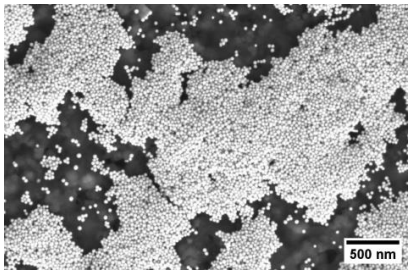

Appendix E

SEM images of the experiment with successive deposition of AuNPs via the modified drop casting method

10 SEM Images after the first deposition

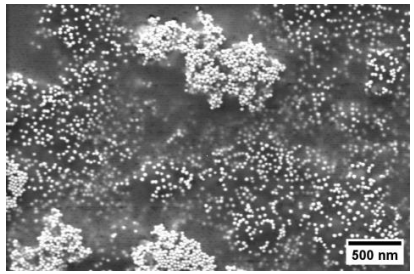

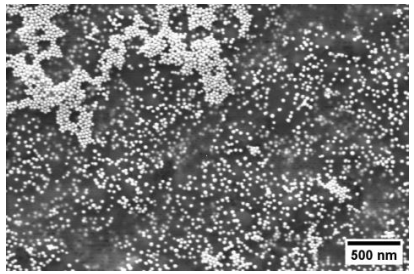

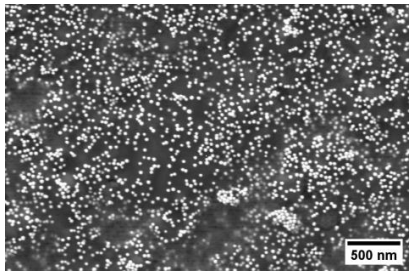

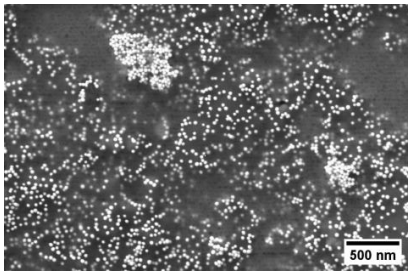

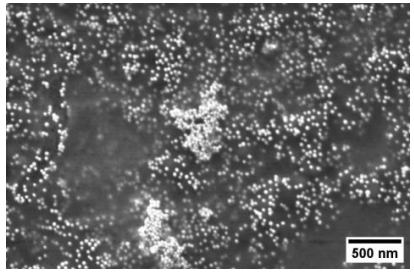

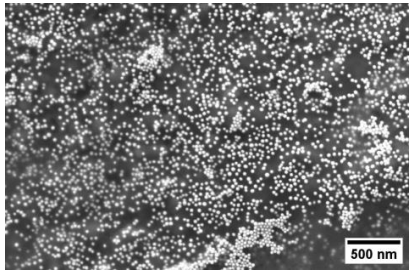

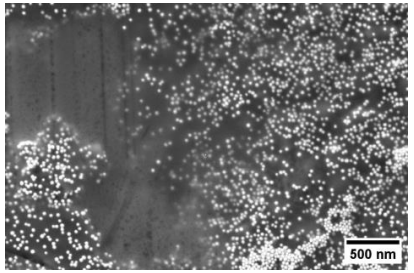

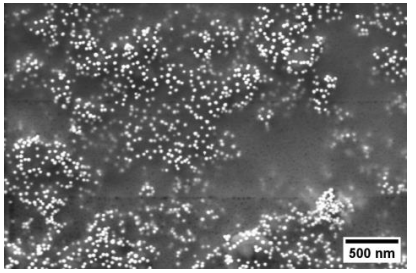

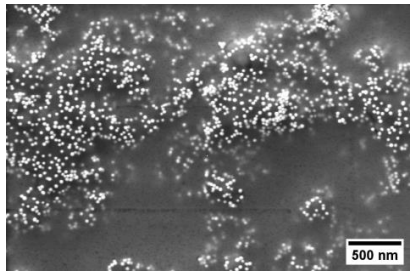

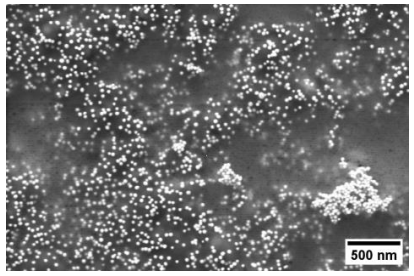

10 SEM Images after the second deposition

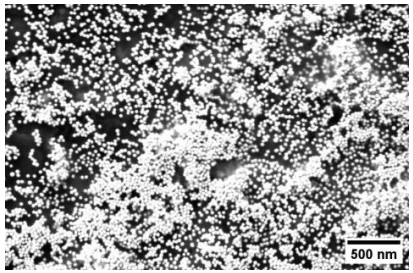

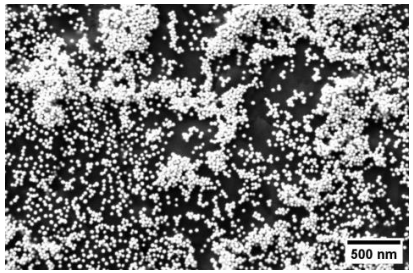

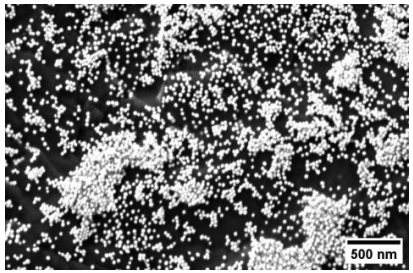

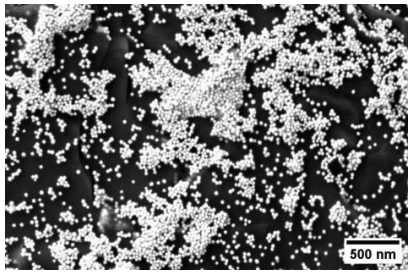

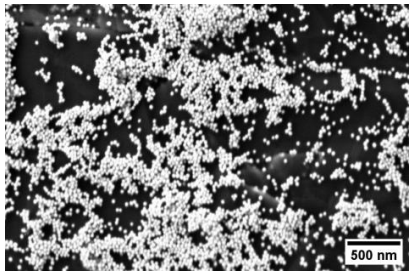

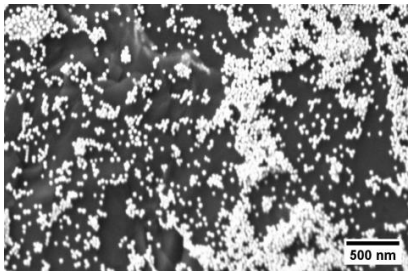

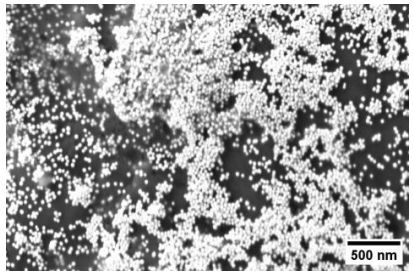

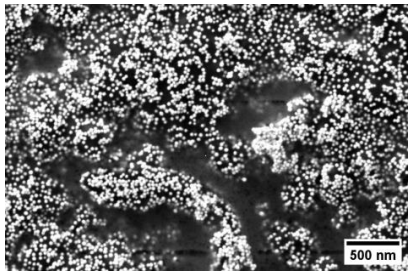

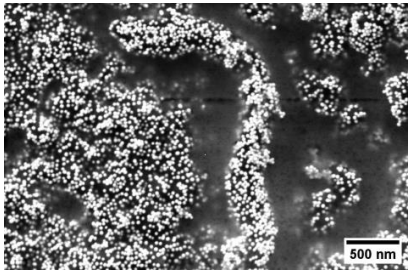

10 SEM Images after the third deposition

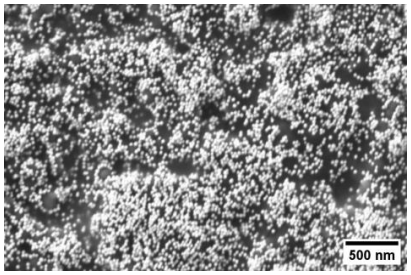

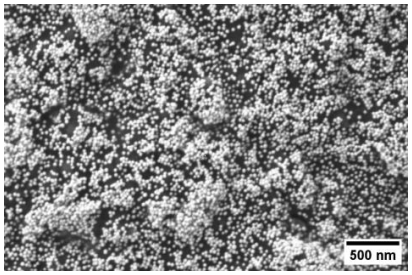

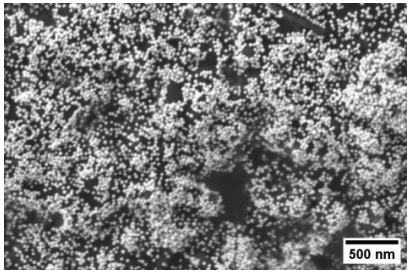

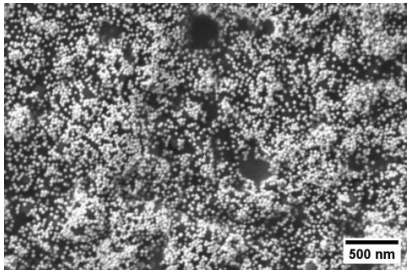

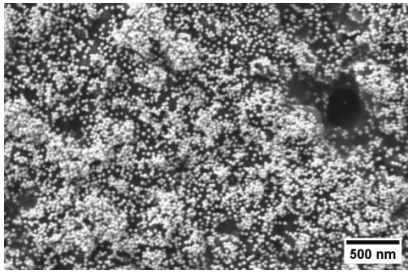

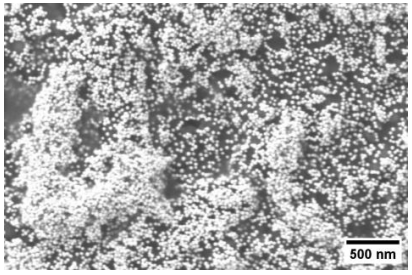

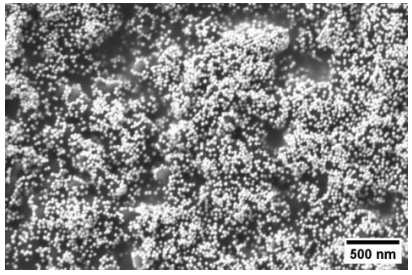

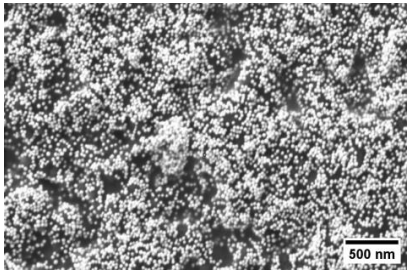

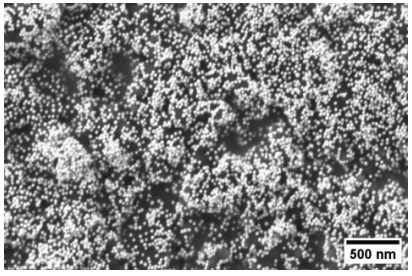

10 SEM Images after the fourth deposition

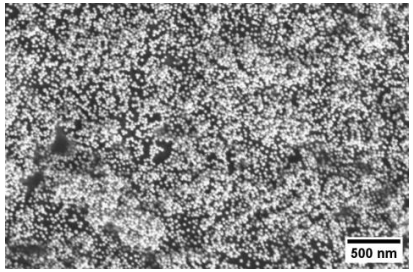

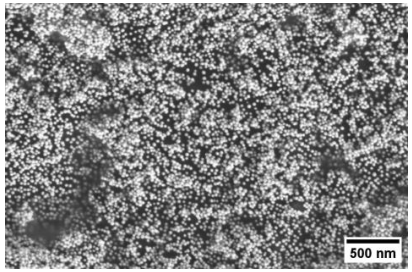

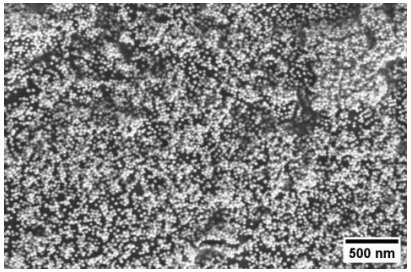

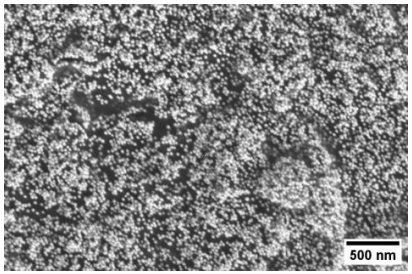

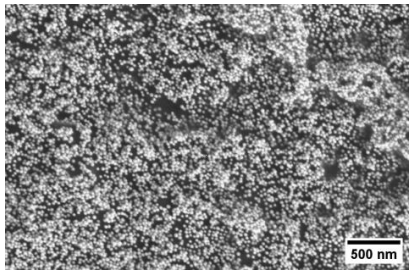

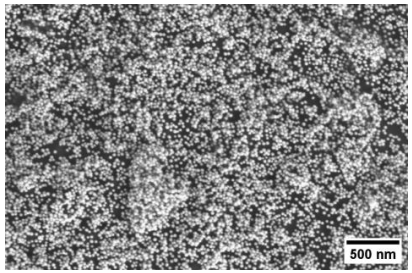

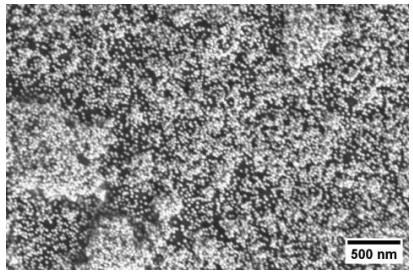

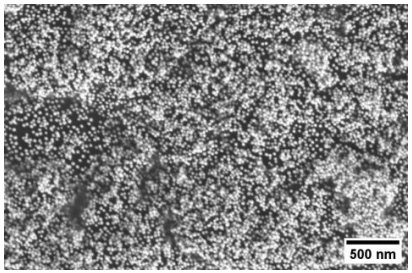

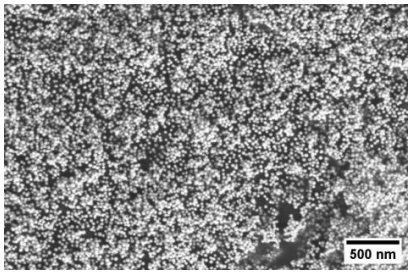

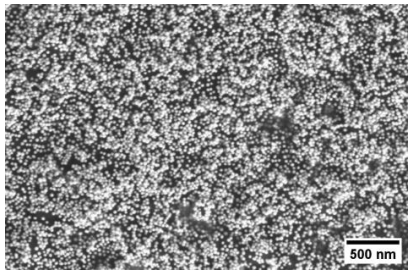

Bibliography

[1] Christopher L. Alexander, Bernard Tribollet, and Mark E. Orazem. "Contribution of Surface Distributions to Constant-Phase-Element (CPE) Behavior: 1. Influence of Roughness". In: *Electrochimica Acta* 173 (Aug. 10, 2015), pp. 416–424. ISSN: 0013-4686. DOI: 10.1016/j.electacta.2015.05.010. URL: https://www.sciencedirect.com/science/article/pii/S0013468615011214 (visited on 05/26/2024).

[2] *automatic nuclei counter plugin for imagej | Center for Bio-Image Informatics | UC Santa Barbara*. URL: https://bioimage.ucsb.edu/docs/automatic-nuclei-counter-plugin-imagej (visited on 05/27/2024).

[3] Elif Burcu Bahadır and Mustafa Kemal Sezgintürk. "A review on impedimetric biosensors". In: *Artificial Cells, Nanomedicine, and Biotechnology* 44.1 (Jan. 2, 2016), pp. 248–262. ISSN: 2169-1401, 2169-141X. DOI: 10.3109/21691401.2014.942456. URL: https://www.tandfonline.com/doi/full/10.3109/21691401.2014.942456 (visited on 04/21/2024).

[4] *Basics of EIS: Electrochemical Research-Impedance Gamry Instruments*. URL: https://www.gamry.com/application-notes/EIS/basics-of-electrochemical-impedance-spectroscopy/ (visited on 05/05/2024).

[5] L Besra and M Liu. "A review on fundamentals and applications of electrophoretic deposition (EPD)". In: *Progress in Materials Science* 52.1 (Jan. 2007), pp. 1–61. ISSN: 00796425. DOI: 10.1016/j.pmatsci.2006.07.001. URL: https://linkinghub.elsevier.com/retrieve/pii/S0079642506000387 (visited on 04/12/2024).

[6] Laxmidhar Besra et al. "Bubble-Free Aqueous Electrophoretic Deposition (EPD) by Pulse-Potential Application". In: *Journal of the American Ceramic Society* 91.10 (Oct. 2008), pp. 3154–3159. ISSN: 0002-7820, 1551-2916. DOI: 10.1111/j.1551-2916.2008.02591.x. URL: https://ceramics.onlinelibrary.wiley.com/doi/10.1111/j.1551-2916.2008.02591.x (visited on 05/20/2024).

[7] Tanu Bhardwaj. "REVIEW ON BIOSENSOR TECHNOLOGIES". In: 6.2 ().

[8] D Buttard, F Oelher, and T David. "Gold colloidal nanoparticle electrodeposition on a silicon surface in a uniform electric field". In: *Nanoscale Res Lett* 6.1 (Dec. 2011), p. 580. ISSN: 1556-276X. DOI: 10.1186/1556-276X-6-580. URL: https://link.springer.com/10.1186/1556-276X-6-580 (visited on 04/12/2024).

[9] Utkarsh Chadha et al. "Recent progress and growth in biosensors technology: A critical review". In: *Journal of Industrial and Engineering Chemistry* 109 (May 2022), pp. 21–51. ISSN: 1226086X. DOI: 10.1016/j.jiec.2022.02.010. URL: https://linkinghub.elsevier.com/retrieve/pii/S1226086X22000600 (visited on 04/21/2024).

[10] Xiaojun Chen et al. "Electrochemical Impedance Immunosensor Based on Three-Dimensionally Ordered Macroporous Gold Film". In: *Anal. Chem.* 80.6 (Mar. 15, 2008), pp. 2133–2140. ISSN: 0003-2700, 1520-6882. DOI: 10.1021/ac7021376. URL: https://pubs.acs.org/doi/10.1021/ac7021376 (visited on 04/12/2024).

[11] Hao-Chun Chiang et al. "Optimization of the Electrodeposition of Gold Nanoparticles for the Application of Highly Sensitive, Label-Free Biosensor". In: *Biosensors* 9.2 (June 2019). Number: 2 Publisher: Multidisciplinary Digital Publishing Institute, p. 50. ISSN: 2079-6374. DOI: 10.3390/bios9020050. URL: https://www.mdpi.com/2079-6374/9/2/50 (visited on 05/13/2024).

[12] Norman Chiu and Theodore K. Christopoulos. *Advances in Immunoassay Technology*. Google-Books-ID: cNKZDwAAQBAJ. BoD – Books on Demand, Mar. 23, 2012. 194 pp. ISBN: 978-953-51-0440-7.

[13] Woosung Choi et al. "Modeling and Applications of Electrochemical Impedance Spectroscopy (EIS) for Lithium-ion Batteries". In: *J. Electrochem. Sci. Technol* 11.1 (Jan. 20, 2020). Publisher: The Korean Electrochemical Society, pp. 1–13. ISSN: 2093-8551, 2288-9221. DOI: 10.33961/jecst.2019.00528. URL: http://www.jecst.org/journal/view.php?doi=10.33961/jecst.2019.00528 (visited on 05/26/2024).

[14] *Deep vein thrombosis (DVT): Blood-clotting disorder with dangerous complications-Deep vein thrombosis (DVT) - Symptoms & causes*. Mayo Clinic. URL: https://www.mayoclinic.org/diseases-conditions/deep-vein-thrombosis/symptoms-causes/syc-20352557 (visited on 05/29/2024).

[15] *Definition of standard_redox_potential - Chemistry Dictionary*. URL: https://www.chemicool.com/definition/standard_redox_potential.html (visited on 05/26/2024).

[16] James H. Dickerson and Aldo R. Boccaccini, eds. *Electrophoretic Deposition of Nanomaterials*. Nanostructure Science and Technology. New York, NY: Springer New York, 2012. ISBN: 978-1-4419-9690-9 978-1-4419-9730-2. DOI: 10.1007/978-1-4419-9730-2. URL: https://link.springer.com/10.1007/978-1-4419-9730-2 (visited on 05/22/2024).

[17] Noémie Elgrishi et al. "A Practical Beginner's Guide to Cyclic Voltammetry". In: *J. Chem. Educ.* 95.2 (Feb. 13, 2018), pp. 197–206. ISSN: 0021-9584, 1938-1328. DOI: 10.1021/acs.jchemed.7b00361. URL: https://pubs.acs.org/doi/10.1021/acs.jchemed.7b00361 (visited on 05/12/2024).

[18] Anab Fatima, Ishrat Younas, and Mohammad Waqar Ali. "An Overview on Recent Advances in Biosensor Technology and its Future Application". In: *Arch. Pharm. Pract* 13.1 (2022), pp. 5–10. ISSN: 2320-5210. DOI: 10.51847/LToGI43jil. URL: https://archivepp.com/article/an-overview-on-recent-advances-in-biosensor-technology-and-its-future-application-p2wlyubdhliextw (visited on 05/01/2024).

[19] Fabiana S. Felix and Lúcio Angnes. "Electrochemical immunosensors – A powerful tool for analytical applications". In: *Biosensors and Bioelectronics* 102 (Apr. 2018), pp. 470–478. ISSN: 09565663. DOI: 10.1016/j.bios.2017.11.029. URL: https://linkinghub.elsevier.com/retrieve/pii/S0956566317307583 (visited on 04/12/2024).

[20] Anca Florea et al. "Label free MUC1 aptasensors based on electrodeposition of gold nanoparticles on screen printed electrodes". In: *Electrochemistry Communications* 33 (Aug. 2013), pp. 127–130. ISSN: 13882481. DOI: 10.1016/j.elecom.2013.05.008. URL: https://linkinghub.elsevier.com/retrieve/pii/S1388248113001914 (visited on 04/12/2024).

[21] Dorothee Grieshaber et al. "Electrochemical Biosensors - Sensor Principles and Architectures". In: *Sensors (Basel)* 8.3 (Mar. 7, 2008), pp. 1400–1458. ISSN: 1424-8220. URL: https://www.ncbi.nlm.nih.gov/pmc/articles/PMC3663003/ (visited on 05/04/2024).

[22] Xuefang Gu et al. "Enhanced electrochemical and SERS signals by self-assembled gold microelectrode arrays: A dual readout platform for multiplex immumoassay of tumor biomarkers". In: *Sensors and Actuators B: Chemical* 334 (May 2021), p. 129674. ISSN: 09254005. DOI: 10.1016/j.snb.2021.129674. URL: https://linkinghub.elsevier.com/retrieve/pii/S0925400521002422 (visited on 04/12/2024).

[23] Alex D. Herbert, Antony M. Carr, and Eva Hoffmann. "FindFoci: A Focus Detection Algorithm with Automated Parameter Training That Closely Matches Human Assignments, Reduces Human Inconsistencies and Increases

Speed of Analysis". In: *PLoS ONE* 9.12 (Dec. 5, 2014). Ed. by Michael Lichten, e114749. ISSN: 1932-6203. DOI: 10.1371/journal.pone.0114749. URL: https://dx.plos.org/10.1371/journal.pone.0114749 (visited on 05/31/2024).

[24] Bertold Hock. "Antibodies for immunosensors a review". In: *Analytica Chimica Acta* 347.1 (July 1997), pp. 177–186. ISSN: 00032670. DOI: 10.1016/S0003-2670(97)00167-0. URL: https://linkinghub.elsevier.com/retrieve/pii/S0003267097001670 (visited on 05/04/2024).

[25] Hongwei Jiang et al. "Dynamic hydrogen bubble template electrodeposition of Ru on amorphous Co support for electrochemical hydrogen evolution". In: *International Journal of Hydrogen Energy* 48.57 (July 5, 2023), pp. 21599–21609. ISSN: 0360-3199. DOI: 10.1016/j.ijhydene.2023.03.077. URL: https://www.sciencedirect.com/science/article/pii/S0360319923011060 (visited on 05/12/2024).

[26] Archana Kaliyaraj Selva Kumar et al. "A mini-review: How reliable is the drop casting technique?" In: *Electrochemistry Communications* 121 (Dec. 2020), p. 106867. ISSN: 13882481. DOI: 10.1016/j.elecom.2020.106867. URL: https://linkinghub.elsevier.com/retrieve/pii/S1388248120302186 (visited on 05/22/2024).

[27] Bright Katey et al. "A Review of Biosensors and Their Applications". In: ().

[28] Zsolt Kerner and Tamás Pajkossy. "Impedance of rough capacitive electrodes: the role of surface disorder". In: *Journal of Electroanalytical Chemistry* 448.1 (May 1998), pp. 139–142. ISSN: 15726657. DOI: 10.1016/S0022-0728(98)00025-4. URL: https://linkinghub.elsevier.com/retrieve/pii/S0022072898000254 (visited on 05/26/2024).

[29] JeeYoung Kim and Min Park. "Recent Progress in Electrochemical Immunosensors". In: *Biosensors* 11.10 (Sept. 29, 2021), p. 360. ISSN: 2079-6374. DOI: 10.3390/bios11100360. URL: https://www.mdpi.com/2079-6374/11/10/360 (visited on 05/04/2024).

[30] Alexandros Ch. Lazanas and Mamas I. Prodromidis. "Electrochemical Impedance SpectroscopyA Tutorial". In: *ACS Meas. Sci. Au* 3.3 (June 21, 2023). Publisher: American Chemical Society, pp. 162–193. DOI: 10.1021/acsmeasuresciau.2c00070. URL: https://doi.org/10.1021/acsmeasuresciau.2c00070 (visited on 05/11/2024).

[31] J. Leva-Bueno, Sally A. Peyman, and P. A. Millner. "A review on impedimetric immunosensors for pathogen and biomarker detection". In: *Med Microbiol Immunol* 209.3 (June 2020), pp. 343–362. ISSN: 0300-8584, 1432-1831. DOI:

10.1007/s00430-020-00668-0. URL: http://link.springer.com/10.1007/s00430-020-00668-0 (visited on 05/04/2024).

[32] Ying Li et al. "Hydrogen bubble dynamic template synthesis of porous gold for nonenzymatic electrochemical detection of glucose". In: *Electrochemistry Communications* 9.5 (May 2007), pp. 981–988. ISSN: 13882481. DOI: 10.1016/j.elecom.2006.11.035. URL: https://linkinghub.elsevier.com/retrieve/pii/S1388248106005595 (visited on 05/12/2024).

[33] Ying Li et al. "Superhydrophobicity of 3D Porous Copper Films Prepared Using the Hydrogen Bubble Dynamic Template". In: *Chem. Mater.* 19.23 (Nov. 1, 2007), pp. 5758–5764. ISSN: 0897-4756, 1520-5002. DOI: 10.1021/cm071738j. URL: https://pubs.acs.org/doi/10.1021/cm071738j (visited on 05/27/2024).

[34] Donghai Lin et al. "An impedimetric biosensor for E. coli O157:H7 based on the use of self-assembled gold nanoparticles and protein G". In: *Microchim Acta* 186.3 (Mar. 2019), p. 169. ISSN: 0026-3672, 1436-5073. DOI: 10.1007/s00604-019-3282-3. URL: http://link.springer.com/10.1007/s00604-019-3282-3 (visited on 04/12/2024).

[35] Zhou Linting et al. "An immunosensor for ultrasensitive detection of aflatoxin B1 with an enhanced electrochemical performance based on graphene/conducting polymer/gold nanoparticles/the ionic liquid composite film on modified gold electrode with electrodeposition". In: *Sensors and Actuators B: Chemical* 174 (Nov. 2012), pp. 359–365. ISSN: 09254005. DOI: 10.1016/j.snb.2012.06.051. URL: https://linkinghub.elsevier.com/retrieve/pii/S0925400512006260 (visited on 04/12/2024).

[36] Benjamin L. Liu and Marina Adamich Saltman. "Immunosensor Technology: Historical Perspective and Future Outlook". In: *Lab Med* 27.2 (Feb. 1, 1996), pp. 109–115. ISSN: 0007-5027, 1943-7730. DOI: 10.1093/labmed/27.2.109. URL: https://academic.oup.com/labmed/article-lookup/doi/10.1093/labmed/27.2.109 (visited on 05/04/2024).

[37] Peter B. Luppa, Lori J. Sokoll, and Daniel W. Chan. "Immunosensors—principles and applications to clinical chemistry". In: *Clinica Chimica Acta* 314.1 (Dec. 2001), pp. 1–26. ISSN: 00098981. DOI: 10.1016/S0009-8981(01)00629-5. URL: https://linkinghub.elsevier.com/retrieve/pii/S0009898101006295 (visited on 05/04/2024).

[38] Hend S. Magar, Rabeay Y. A. Hassan, and Ashok Mulchandani. "Electrochemical Impedance Spectroscopy (EIS): Principles, Construction, and Biosensing Applications". In: *Sensors* 21.19 (Oct. 1, 2021), p. 6578. ISSN: 1424-8220. DOI: 10.3390/s21196578. URL: https://www.mdpi.com/1424-8220/21/19/6578 (visited on 05/11/2024).

[39] Parikha Mehrotra. “Biosensors and their applications – A review”. In: *Journal of Oral Biology and Craniofacial Research* 6.2 (May 1, 2016), pp. 153–159. ISSN: 2212-4268. DOI: 10.1016/j.jobcr.2015.12.002. URL: https://www.sciencedirect.com/science/article/pii/S2212426815001323 (visited on 04/12/2024).

[40] Karam Nashwan Al-Milaji and Hong Zhao. “New Perspective of Mitigating the Coffee-Ring Effect: Interfacial Assembly”. In: *J. Phys. Chem. C* 123.19 (May 16, 2019). Publisher: American Chemical Society, pp. 12029–12041. ISSN: 1932-7447. DOI: 10.1021/acs.jpcc.9b00797. URL: https://doi.org/10.1021/acs.jpcc.9b00797 (visited on 05/13/2024).

[41] S.P. Mohanty and E. Kougianos. “Biosensors: a tutorial review”. In: *IEEE Potentials* 25.2 (Mar. 2006), pp. 35–40. ISSN: 0278-6648. DOI: 10.1109/MP.2006.1649009. URL: http://ieeexplore.ieee.org/document/1649009/ (visited on 04/21/2024).

[42] Fariba Mollarasouli, Sevinc Kurbanoglu, and Sibel A. Ozkan. “The Role of Electrochemical Immunosensors in Clinical Analysis”. In: *Biosensors* 9.3 (Sept. 2019). Number: 3 Publisher: Multidisciplinary Digital Publishing Institute, p. 86. ISSN: 2079-6374. DOI: 10.3390/bios9030086. URL: https://www.mdpi.com/2079-6374/9/3/86 (visited on 05/25/2024).

[43] Salwa M I Morsy. “Role of Surfactants in Nanotechnology and Their Applications”. In: (2014).

[44] Varnakavi. Naresh and Nohyun Lee. “A Review on Biosensors and Recent Development of Nanostructured Materials-Enabled Biosensors”. In: *Sensors* 21.4 (Feb. 5, 2021), p. 1109. ISSN: 1424-8220. DOI: 10.3390/s21041109. URL: https://www.mdpi.com/1424-8220/21/4/1109 (visited on 04/21/2024).

[45] Hoang Hiep Nguyen et al. “Immobilized Enzymes in Biosensor Applications”. In: *Materials (Basel)* 12.1 (Jan. 2, 2019), p. 121. ISSN: 1996-1944. DOI: 10.3390/ma12010121. URL: https://www.ncbi.nlm.nih.gov/pmc/articles/PMC6337536/ (visited on 05/10/2024).

[46] *NOVA*. URL: https://www.metrohm.com/en/service/software-center/nova.html (visited on 05/28/2024).

[47] Tamás Pajkossy. “Impedance spectroscopy at interfaces of metals and aqueous solutions — Surface roughness, CPE and related issues”. In: *Solid State Ionics*. International Workshop on Impedance Spectroscopy for Characterisation of Materials and Structures 176.25 (Aug. 15, 2005), pp. 1997–2003. ISSN: 0167-2738. DOI: 10.1016/j.ssi.2004.06.023. URL: https://www.sciencedirect.com/science/article/pii/S0167273805002031 (visited on 05/26/2024).

[48] Christopher P. Price, Matthew Fay, and Rogier M. Hopstaken. "Point-of-Care Testing for D-Dimer in the Diagnosis of Venous Thromboembolism in Primary Care: A Narrative Review". In: *Cardiol Ther* 10.1 (June 2021), pp. 27–40. ISSN: 2193-8261. DOI: 10.1007/s40119-020-00206-2.

[49] Mamas I. Prodromidis. "Impedimetric immunosensors—A review". In: *Electrochimica Acta* 55.14 (May 2010), pp. 4227–4233. ISSN: 00134686. DOI: 10.1016/j.electacta.2009.01.081. URL: https://linkinghub.elsevier.com/retrieve/pii/S0013468609002138 (visited on 05/05/2024).

[50] U. Rammelt and G. Reinhard. "On the applicability of a constant phase element (CPE) to the estimation of roughness of solid metal electrodes". In: *Electrochimica Acta* 35.6 (June 1990), pp. 1045–1049. ISSN: 00134686. DOI: 10.1016/0013-4686(90)90040-7. URL: https://linkinghub.elsevier.com/retrieve/pii/0013468690900407 (visited on 05/26/2024).

[51] S.P. Rao, S.R. Singh, and S.R. Bandakavi. "Formal Redox Potentials of Ferricyanide Ferrocyanide Couple in Certain Non-Aqueouswater Mixtures". In: *Proc. Natl. Acad. Sci. India A* 44 (Jan. 1, 1978), pp. 333–335.

[52] N. Sandhyarani. "Chapter 3 - Surface modification methods for electrochemical biosensors". In: *Electrochemical Biosensors*. Ed. by Ali A. Ensafi. Elsevier, Jan. 1, 2019, pp. 45–75. ISBN: 978-0-12-816491-4. DOI: 10.1016/B978-0-12-816491-4.00003-6. URL: https://www.sciencedirect.com/science/article/pii/B9780128164914000036 (visited on 05/27/2024).

[53] Jarred B. Shein et al. "Formation of Efficient Electron Transfer Pathways by Adsorbing Gold Nanoparticles to Self-Assembled Monolayer Modified Electrodes". In: *Langmuir* 25.18 (Sept. 15, 2009), pp. 11121–11128. ISSN: 0743-7463, 1520-5827. DOI: 10.1021/la901421m. URL: https://pubs.acs.org/doi/10.1021/la901421m (visited on 04/12/2024).

[54] Giulia Siciliano et al. "Beyond traditional biosensors: Recent advances in gold nanoparticles modified electrodes for biosensing applications". In: *Talanta* 268 (Feb. 2024), p. 125280. ISSN: 00399140. DOI: 10.1016/j.talanta.2023.125280. URL: https://linkinghub.elsevier.com/retrieve/pii/S0039914023010317 (visited on 04/12/2024).

[55] Mandy LY Sin et al. "Advances and challenges in biosensor-based diagnosis of infectious diseases". In: *Expert Rev Mol Diagn* 14.2 (Mar. 2014), pp. 225–244. ISSN: 1473-7159. DOI: 10.1586/14737159.2014.888313. URL: https://www.ncbi.nlm.nih.gov/pmc/articles/PMC4104499/ (visited on 05/05/2024).

[56] *Standard Potentials*. Chemistry LibreTexts. Nov. 26, 2013. URL: https://chem.libretexts.org/Bookshelves/Analytical_Chemistry/Supplemental_Modules_(Analytical_Chemistry)/Electrochemistry/Redox_Potentials/Standard_Potentials (visited on 05/26/2024).

[57] *Statistical Software*. URL: https://www.jmp.com/en_be/home.html (visited on 05/28/2024).

[58] Rossella Svigelj et al. "An Effective Label-Free Electrochemical Aptasensor Based on Gold Nanoparticles for Gluten Detection". In: *Nanomaterials* 12.6 (Mar. 17, 2022), p. 987. ISSN: 2079-4991. DOI: 10.3390/nano12060987. URL: https://www.mdpi.com/2079-4991/12/6/987 (visited on 04/22/2024).

[59] Anita Swami et al. "Langmuir–Blodgett films of laurylamine-modified hydrophobic gold nanoparticles organized at the air–water interface". In: *Journal of Colloid and Interface Science* 260.2 (Apr. 2003), pp. 367–373. ISSN: 00219797. DOI: 10.1016/S0021-9797(03)00047-X. URL: https://linkinghub.elsevier.com/retrieve/pii/S002197970300047X (visited on 05/27/2024).

[60] Amir Syahir et al. "Label and Label-Free Detection Techniques for Protein Microarrays". In: *Microarrays* 4.2 (Apr. 24, 2015), pp. 228–244. ISSN: 2076-3905. DOI: 10.3390/microarrays4020228. URL: http://www.mdpi.com/2076-3905/4/2/228 (visited on 05/24/2024).

[61] Nikola Tasić, Thiago R. L. C. Paixão, and Luís Moreira Gonçalves. "Biosensing of D-dimer, making the transition from the central hospital laboratory to bedside determination". In: *Talanta* 207 (Jan. 15, 2020), p. 120270. ISSN: 0039-9140. DOI: 10.1016/j.talanta.2019.120270. URL: https://www.sciencedirect.com/science/article/pii/S0039914019309038 (visited on 05/30/2024).

[62] Noach Treitel, Einat Kohn, and Ruthy Sfez. "From Glass to Gold: Visualization of Electrostatic Self-Assembly of Gold Nanoparticles". In: *J. Chem. Educ.* 100.2 (Feb. 14, 2023), pp. 835–843. ISSN: 0021-9584, 1938-1328. DOI: 10.1021/acs.jchemed.2c00796. URL: https://pubs.acs.org/doi/10.1021/acs.jchemed.2c00796 (visited on 04/12/2024).

[63] *Two,Three,Four Electrode System Gamry 4-Probe Potentiostats Gamry Instruments*. URL: https://www.gamry.com/application-notes/instrumentation/two-three-four-electrode-experiments/ (visited on 05/26/2024).

[64] *Venous Thromboembolism - What Is Venous Thromboembolism? | NHLBI, NIH*. URL: https://www.nhlbi.nih.gov/health/venous-thromboembolism (visited on 05/28/2024).

[65] S. Vigneshvar et al. “Recent Advances in Biosensor Technology for Potential Applications – An Overview”. In: *Front. Bioeng. Biotechnol.* 4 (Feb. 16, 2016). ISSN: 2296-4185. DOI: 10.3389/fbioe.2016.00011. URL: http://journal.frontiersin.org/Article/10.3389/fbioe.2016.00011/abstract (visited on 05/01/2024).

[66] Yixian Wang et al. “Impedimetric immunosensor based on gold nanoparticles modified graphene paper for label-free detection of *Escherichia coli* O157:H7”. In: *Biosensors and Bioelectronics* 49 (Nov. 15, 2013), pp. 492–498. ISSN: 0956-5663. DOI: 10.1016/j.bios.2013.05.061. URL: https://www.sciencedirect.com/science/article/pii/S0956566313003953 (visited on 05/05/2024).

[67] Hideo Watanabe et al. “Electrophoretic and Electrolytic Deposition of Gold Nanoparticles on a Graphite Carbon Plate”. In: *KEM* 412 (June 2009), pp. 71–75. ISSN: 1662-9795. DOI: 10.4028/www.scientific.net/KEM.412.71. URL: https://www.scientific.net/KEM.412.71 (visited on 05/22/2024).

[68] M.-P. Winter, G. H. Schernthaner, and I. M. Lang. “Chronic complications of venous thromboembolism”. In: *J Thromb Haemost* 15.8 (Aug. 2017), pp. 1531–1540. ISSN: 1538-7836. DOI: 10.1111/jth.13741.

[69] Youchun Xu et al. “A review of impedance measurements of whole cells”. In: *Biosensors and Bioelectronics* 77 (Mar. 2016), pp. 824–836. ISSN: 09565663. DOI: 10.1016/j.bios.2015.10.027. URL: https://linkinghub.elsevier.com/retrieve/pii/S0956566315304917 (visited on 05/05/2024).

[70] Shui-Ping Yang. “Microscale Synthesis and Characterization of Gold Nanoparticles for the Laboratory Instruction”. In: ().

[71] Xu Yiwei et al. “Oligonucleotide Functionalized Microporous Gold Electrode for the Selective and Sensitive Determination of Mercury by Differential Pulse Adsorptive Stripping Voltammetry (DPAdSV)”. In: *Analytical Letters* 52.18 (Dec. 12, 2019), pp. 2938–2950. ISSN: 0003-2719, 1532-236X. DOI: 10.1080/00032719.2019.1631839. URL: https://www.tandfonline.com/doi/full/10.1080/00032719.2019.1631839 (visited on 04/12/2024).

[72] Xingcheng Zhou et al. “Recent Advances in Signal Amplification to Improve Electrochemical Biosensing for Infectious Diseases”. In: *Front Chem* 10 (June 13, 2022), p. 911678. ISSN: 2296-2646. DOI: 10.3389/fchem.2022.911678. URL: https://www.ncbi.nlm.nih.gov/pmc/articles/PMC9234564/ (visited on 05/27/2024).

[73] Sheng-Qing Zhu et al. “Gold nanoparticle thin films fabricated by electrophoretic deposition method for highly sensitive SERS application”. In: *Nanoscale Res Lett* 7.1 (Dec. 2012), p. 613. ISSN: 1556-276X. DOI: 10.1186/1556-276X-7-613. URL: https://link.springer.com/10.1186/1556-276X-7-613 (visited on 04/12/2024).

Use of generative AI for the writing of this thesis: Chagpt and Grammarly were used to correct spelling and grammar mistakes and improve the text formulation

UNIVERSITÉ CATHOLIQUE DE LOUVAIN
École polytechnique de Louvain
Rue Archimède, 1 bte L6.11.01, 1348 Louvain-la-Neuve, Belgique | **www.uclouvain.be/epl**